

Whole slide imaging systems for digital pathology

Shakeri, Mojtaba

DOI

[10.4233/uuid:4890151d-0052-4107-93f1-3ab2c5283cf8](https://doi.org/10.4233/uuid:4890151d-0052-4107-93f1-3ab2c5283cf8)

Publication date

2017

Document Version

Final published version

Citation (APA)

Shakeri, M. (2017). *Whole slide imaging systems for digital pathology*. [Dissertation (TU Delft), Delft University of Technology]. <https://doi.org/10.4233/uuid:4890151d-0052-4107-93f1-3ab2c5283cf8>

Important note

To cite this publication, please use the final published version (if applicable).
Please check the document version above.

Copyright

Other than for strictly personal use, it is not permitted to download, forward or distribute the text or part of it, without the consent of the author(s) and/or copyright holder(s), unless the work is under an open content license such as Creative Commons.

Takedown policy

Please contact us and provide details if you believe this document breaches copyrights.
We will remove access to the work immediately and investigate your claim.

Whole Slide Imaging Systems for Digital Pathology

S. Mojtaba Shakeri



WHOLE SLIDE IMAGING SYSTEMS FOR DIGITAL PATHOLOGY

WHOLE SLIDE IMAGING SYSTEMS FOR DIGITAL PATHOLOGY

Proefschrift

ter verkrijging van de graad van doctor
aan de Technische Universiteit Delft,
op gezag van de Rector Magnificus prof. ir. K.C.A.M. Luyben,
voorzitter van het College voor Promoties,
in het openbaar te verdedigen op donderdag 26 januari 2017 om 15:00 uur

door

S. Mojtaba SHAKERI

Master of Science in Electrical Engineering (Control),
Iran University of Science and Technology, Tehran, Iran
geboren te Mashhad, Iran.

Dit proefschrift is goedgekeurd door de

promotor: Prof. dr. ir. L.J. Van Vliet

copromotor: dr. S. Stallinga

Samenstelling promotiecommissie:

Rector Magnificus,	voorzitter
Prof. dr. ir. L.J. Van Vliet,	Technische Universiteit Delft
Dr. S. Stallinga,	Technische Universiteit Delft

Onafhankelijke leden:

Prof. dr. ir. M. Verhaegen	Technische Universiteit Delft
Prof. dr. P. Török	Imperial College London
Prof. dr. J. Morreau	Leiden University Medical Center
Prof. dr. W.M.J. Coene	Technische Universiteit Delft & ASML

Overige leden:

Dr. B. Hulskens,	Philips Digital Pathology Solutions
------------------	-------------------------------------



This work was carried out in the Department of Imaging Physics at the faculty of Applied Sciences of Delft University of Technology. The research effort was in cooperation with Philips Digital Pathology Solutions and was funded by the bioimaging technology consortium Cyttron II.

Printed by: IPSKAMP printing, Enschede, The Netherlands.

Front: (Right) A typical pathology tissue slide. (Left) Images of a $4\mu\text{m}$ thick prostate tissue slide stained with H&E at different focus levels.

Copyright © 2016 by S.M. Shakeri

ISBN 978-94-6186-781-0

An electronic version of this dissertation is available at

<http://repository.tudelft.nl/>.

All generalizations are dangerous, even this one.

Alexandre Dumas

CONTENTS

1	Introduction	1
1.1	Digital Pathology	2
1.2	Whole Slide Imaging (WSI) systems	5
1.3	Technical challenges	6
1.3.1	Optical quality assessment	7
1.3.2	Full-field aberration maps and Alignment Test	9
1.3.3	Illumination	10
1.3.4	From 2D to 3D imaging	11
1.4	Thesis challenges & outline	12
	References	14
2	Optical quality assessment of WSI systems for digital pathology	19
2.1	Introduction	20
2.2	Methods	22
2.2.1	Scanning and image acquisition	22
2.2.2	OTF measurement	22
2.2.3	Aberration extraction	24
2.2.4	Shack-Hartmann measurements	26
2.3	Results	27
2.3.1	Effect of the tube lens design	27
2.3.2	Statistical errors	31
2.3.3	Effect of an aging objective lens	31
2.3.4	Validation with Shack-Hartmann wavefront sensor	33
2.3.5	Chromatic aberration	35
2.4	Discussion	35
	References	36
3	Shack-Hartmann sensor based optical quality testing of WSI systems	41
3.1	Introduction	42
3.2	Methods	42
3.2.1	Shack-Hartmann test setup	43
3.2.2	Full-field aberration map analysis	43
3.3	Results	45
3.3.1	OTF-based vs. Shack-Hartmann aberration measurement	45
3.3.2	Full-field aberration map analysis	49
3.4	Conclusion	52
	References	53

4	The impact of partial coherence on the apparent optical transfer function derived from the response to amplitude edges	55
4.1	Introduction	56
4.2	Theory and simulation	57
4.2.1	Apparent transfer functions and performance function	57
4.2.2	Edge ringing	60
4.2.3	Depth Of Focus	63
4.2.4	Aberration estimation	67
4.3	Experiment	69
4.3.1	Scanner with compact flat-field Köhler illumination unit	69
4.3.2	Experimental results	72
4.4	Discussion	78
	References	80
5	Novel 3D multispectral WSI platform for digital pathology	83
5.1	Introduction	84
5.2	Methods	87
5.2.1	3D scanner architecture	87
5.2.2	System Characterization	92
5.2.3	Image analysis	95
5.3	Results	99
5.3.1	Sensor characterization	99
5.3.2	Optical characterization	99
5.3.3	H&E stained tissue slides.	106
5.3.4	Multispectral image analysis	106
5.3.5	Defocus-based phase retrieval	107
5.4	Discussion	113
	References	114
6	Conclusions & Recommendations	119
6.1	Conclusions.	119
6.2	Recommendations	121
6.2.1	Optical quality test.	121
6.2.2	NAT and distortion.	121
6.2.3	3D WSI platform	122
	Summary	125
	Samenvatting	127
	Curriculum Vitæ	129
	List of Publications	131
	Acknowledgements	133

1

INTRODUCTION

There is nothing permanent except change.

Heraclitus

CHANGING a routine, which has been practiced for years, is difficult and it needs motivation and incentives to be brought about. This represents the current situation for pathologists who make intricate diagnoses of diseases by microscopic examination of the morphology of tissues. Currently they perform the majority of primary diagnoses through visual inspection via the eyepiece of a microscope. The upcoming alternative to this conventional workflow is a digital workflow in which the diagnosis is based on digital high-resolution images taken by automated microscopes, which are called Whole Slide Imaging (WSI) systems in this field. In this chapter I will explain the differences between the conventional and digital workflow and specifying the potential benefits of "going digital". WSI systems, which are the focus of this thesis, are crucial to enable the transition to digital pathology. After introducing WSI systems I present four important technical challenges; optical quality, alignment tests, illumination, and 3D imaging which play an essential role in optimizing the output of WSI systems. Lastly, the outline of this thesis is presented.

1.1. DIGITAL PATHOLOGY

The word pathology originates from two Greek roots *pathos* and *-logia* which literally means "*study of suffering*". This explains the function of pathology as an important branch of medical science. Pathologists specialize in finding the root causes of diseases by examining different organs, tissues and body fluids. Among the wide range of diseases, cancer is currently the most important to be diagnosed. Starting point in a pathology examination is the preparation of tissue sections cut from the suspected organ, either post-surgically or via a needle biopsy. In a subsequent step cells are stained, specific proteins important in tumor growth are labeled (immunostaining), or specific chromosomes are marked (in-situ hybridization techniques). The most common staining technique is Hematoxylin and Eosin staining, mostly abbreviated as H&E staining. Hematoxylin gives a deep-blue purple color to nucleic acids (highlighting the nuclei of the cells). Eosin is pink and stains proteins (highlighting the cytoplasm and the extracellular matrix) [1]. Upon inspection of the tissue morphology, it is decided whether the tissue under examination belongs to a tumor, along with type and severity scale (cancer grade). Figure 4.11 shows an illustration of prostate cancer progressing from stage I to IV. It depicts how cancer cells (yellow area) grow from within the prostate to other nearby tissues and organs at different stages of the disease [2].

In Figure 4.12, different cases of prostate tissue sections are shown [3]. In part (a) a normal prostate tissue section stained with H&E shows uniform round and oval nuclei and also clear cytoplasm. Three regions can be distinguished: the transparent lumen, haematoxylin-rich epithelial cells, and eosin-rich stroma. A distortion of the topology of these different regions is one of the hallmarks of tumor progression. However in part (b), three areas (shown with dashed yellow contour) are suspected for cancer since they have enlarged nuclei, visible nucleoli, and also the layer of the so-called basal cells seems to be absent. To confirm this absence, an immunostaining protocol can be used to highlight basal cells with a brown color. The outcome is shown in part (c), which validates the interpretation of the tissue morphology in (b). Parts (e) to (g) show the result of a prostate needle biopsy as the cancer stage increases. This corresponds qualitatively with the tumor growth shown in Fig.4.11.

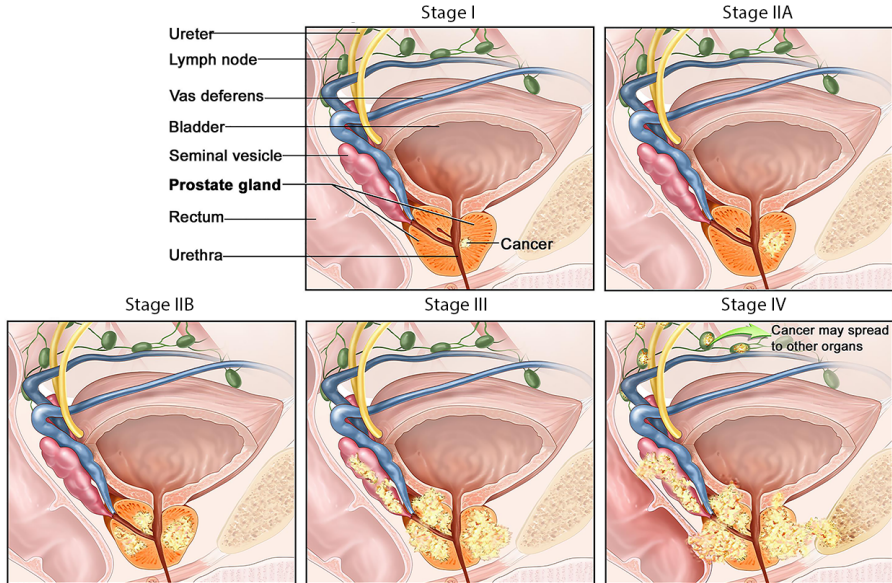


Figure 1.1: Different stages of prostate cancer. In stage I and II, cancer stays inside the prostate. It spreads to the outer layer of the prostate in stage III. In the most advanced stage IV, it may spread to other organs and even to the bone (Adapted from [2]).

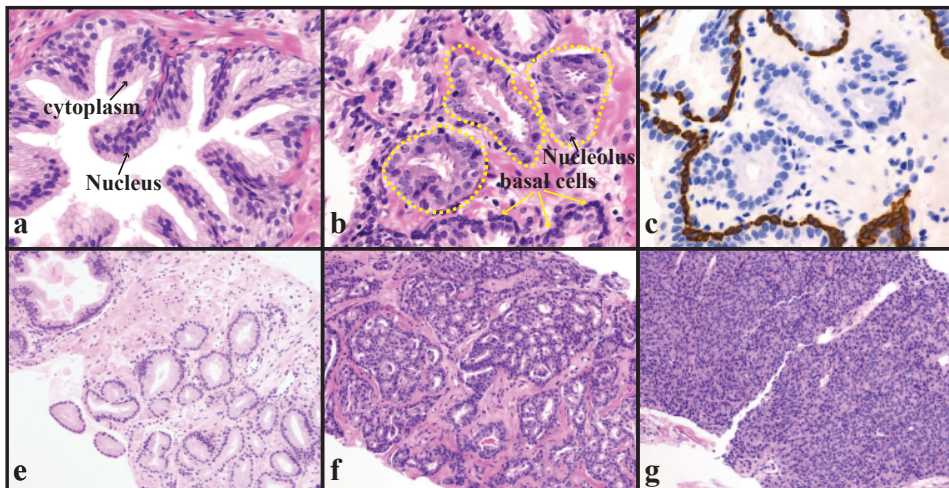


Figure 1.2: Prostate tissue sections for cancer diagnosis [3]. (a) High magnification image of a normal prostate tissue section. (b) H&E stained tissue with three areas (dashed yellow contour) suspected for cancer due to the absence of basal cells and irregularity of nuclear shape. (c) The absence of basal cells is confirmed by staining the same section as part b with a high molecular weight cytokeratin (HMWCK) antibody, which gives a brown color to basal cells. (e) to (g) Low magnification images of H&E stained cancerous prostate tissues with increasing stage.

The entire process of extracting tissue, preparation, viewing, diagnosing, reporting and finally archiving results comprises the pathology workflow. In a conventional workflow pathologists make a diagnosis by looking at a tissue slide through a conventional microscope. This workflow also involves manual quality assurance, case assembly and sorting and case fetching [4]. In the digital workflow several stacks of tissue slides are automatically scanned, digitized and archived for a pathologist to make a diagnosis. The pathologist can be located anywhere, even away from the local pathology lab. These features bring many advantages to pathology, specifically for educational [5–7] and research purposes [8, 9]. In education, it can reduce the cost by eliminating the need for acquiring and maintaining a large number of microscopes and by reducing the risk of damaged or unsatisfactory slides. Additionally, the quality of education may increase by having access to a broader range of cases [10]. Digital pathology can also facilitate cooperation among pathologists by regional collaborations, communications, expert consultation [11–14], and by providing access to pathology services in remote locations [15, 16]. Moreover, digital pathology can aid in making diagnoses more objective by quantitative image analysis methods. This is called Computer Aided Diagnostics (CAD) [17, 18] or sometimes Clinical Decision Support (CDS) [19]. These methods need to be tailored to specific diseases/tumor types, e.g. for prostate cancer [20]. One may even need to develop case specific measurements of relevant image features, the so-called biomarkers, for different types of prostate cancer.

The majority of primary diagnosis is still made by following the conventional workflow, despite the benefits of digital pathology and its popularity in research and education [10, 15, 21]. Reasons for this slow transition are the cost of the necessary infrastructure [22], standards and regulatory approval [23], unfamiliarity with digital workflow [24], and a perception of possible inferior performance [15]. These barriers can be overcome by further developing this technology and performing more validation studies [25, 26] to ensure a satisfactory performance for pathologists.

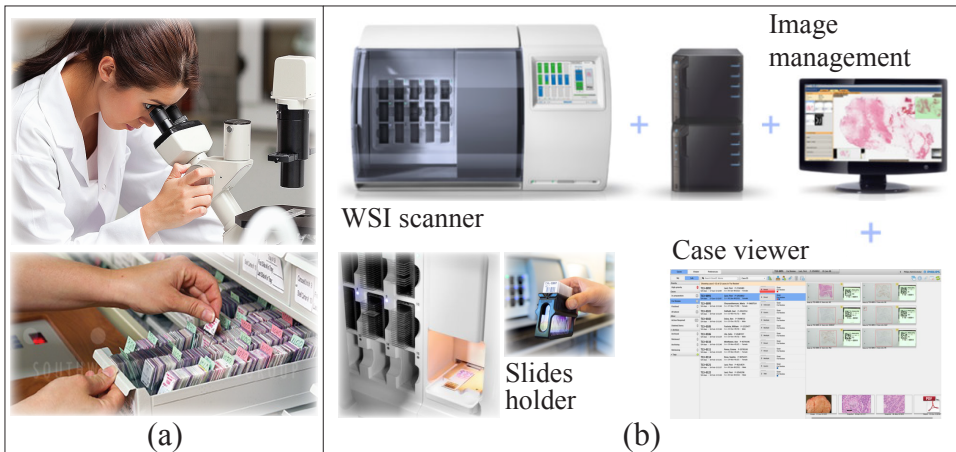


Figure 1.3: (a) Conventional pathology using a normal microscope to examine tissue slides. (b) Digital pathology elements including a WSI scanner, image management system and case viewer. (Image sources: www.pathologyca.com, www.southwestsolutions.com, and www.philips.co.uk)

1.2. WHOLE SLIDE IMAGING (WSI) SYSTEMS

The key enabler for digital pathology is the WSI system. This is an automated microscope system packed with a variety of software and hardware tools for digitizing, processing, and storing images of entire tissue slides in the shortest possible amount of time and with the highest possible image quality. Hardware tools make up the slide scanner engine of the WSI system and comprise of one or more cameras, a set of lenses and mirrors for illumination and imaging, and a high precision automated stage for moving and focusing of the tissue slide. The specification of these parts defines the microscopy type and performance in terms of speed and image quality. Fig. 4.14 shows the schematics of two common types of microscope in pathology: brightfield and fluorescence. Brightfield microscopy is most widely used in pathology due to its low cost, simplicity and the availability of various visible stains including the default H&E stain, but also Immunohistochemistry (IHC) stains and Chromogenic In Situ Hybridization (CISH) stains. Fluorescence microscopy is more complicated to implement, more expensive, and its performance in terms of speed is not up to par with the current available brightfield scanners [27].

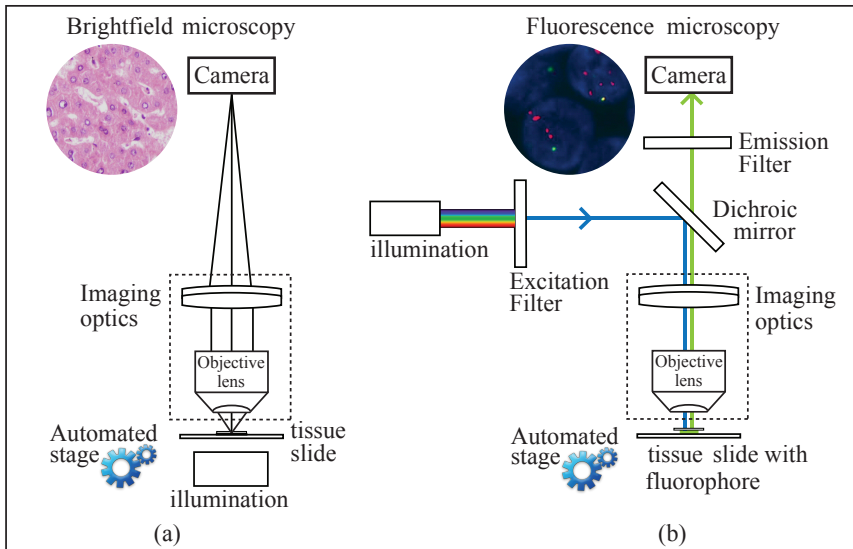


Figure 1.4: Schematic overview of the microscopy principles of WSI systems in digital pathology **(a)** Brightfield microscopy: The tissue is imaged in transmission mode, i.e. illuminated from below and imaged from above. Samples absorb light and their image forms on a bright background. **(b)** Fluorescence microscopy: A high contrast and sensitivity is obtained by epi-illumination. Light of a specific wavelength illuminates tissue from above and is absorbed by fluorophores that label target proteins or genes inside the tissue. The excited fluorophores re-emit light with a longer wavelength which is separated from the incident light on the way back to the camera. The resulting images have a dark background with bright fluorescent labels on the foreground.

Another important aspect of designing WSI system is the scanning method. The two main methods are tile-based and line-based scanning (see Fig. 4.16) [28]. In the tile-based method, the area to be scanned is divided into a matrix of square blocks, which

are imaged one by one in a start-stop mode. They are subsequently aligned and stitched together by a post processing step. To improve the alignment accuracy blocks have to overlap by about 2%-5%. In the line-based method, the stage moves continuously in one direction and at each step the image of one line will be captured. This procedure continues until the entire slide is scanned lane by lane. A key advantage of the line-based method is that it reduces the difficulty of post-processing in alignment and stitching. It also increases the scanning speed due to its simplicity and the possibility of employing fast line-scan cameras.

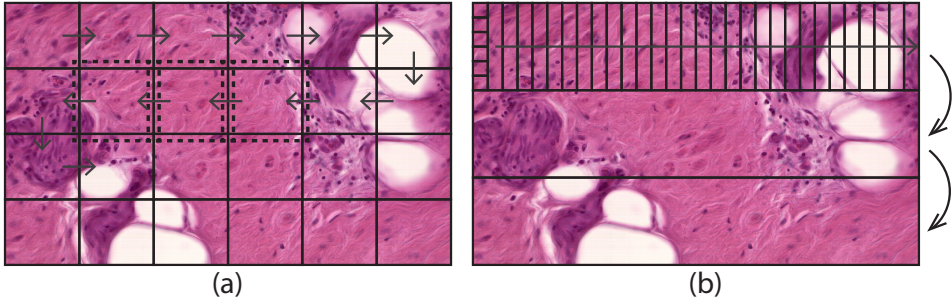


Figure 1.5: WSI system scanning methods: (a) Tile-based scanning. (b) Line-based scanning.

The file size of a digitized image mostly depends on the specifications of the WSI system especially its resolution. With a typical sampling pitch of $0.25 \mu m/pixel$, the file size of the final RGB image amounts to roughly 10 GB uncompressed data for a standard tissue area of about $15 \times 15 mm^2$. This requires a sophisticated image management system to perform lossless compression and then store the image in a coded way for retrieving the image as fast as possible. To this end, the image files are wavelet encoded into an image pyramid with the ability to switch between different scales or effective magnifications. At each zoom level images are split into small tiles to speed up and facilitate the image viewing experience for pathologists [27].

1.3. TECHNICAL CHALLENGES

WSI systems should be capable of automatically acquiring digitized images of at least comparable image quality as a conventional microscope. This yields the following set of technical challenges, which are important for both end-user and manufacturer. The main challenge is to know how good is the optical image quality of a digitized tissue slide. This is important for end-user to trust the sanity of WSI system, and also for manufacturer to deliver a system with maximized optical quality. Another challenge is how to adjust WSI system parameters, specifically its illumination, to further increase the image quality. Final challenge is a practical and effective transition from 2D to 3D imaging, which brings additional benefits to the field of digital pathology.

1.3.1. OPTICAL QUALITY ASSESSMENT

Pathologists need assurances that the WSI system produces images that faithfully represent the tissue slides. This image quality depends to a large extent on how well the imaging optics is designed and integrated with the rest of the system. In order to assess the optical quality, it is important to know what the ultimate limitations of the optical quality are regardless of how well the system is designed or assembled. The wave nature of light limits the resolution of a perfect optical imaging system. According to Ernst Abbe this so-called diffraction limit is given by $d = \lambda / (2 \times NA)$ where λ is the wavelength of light and NA is the numerical aperture of the objective lens that collects the light. Nyquist's sampling theorem then implies that the pixel size back projected to object space must be less than $\lambda / 4NA$. NA is defined as $n \sin(\theta)$ where n represents the medium refractive index and θ is the semi-angle of the objective lens angular aperture (see Fig. 1.6). Improving the resolution is therefore possible by decreasing the wavelength or increasing the NA. For example, with green light ($\lambda \approx 500nm$) and $NA = 0.75$ a resolution of approximately $0.33 \mu m$ is achievable. This is sufficient to study tissue at the cellular level ($1 \mu m - 10 \mu m$), which is specifically needed for pathology applications. Now the question is what can further

limit the system and make it perform worse than diffraction-limited. The answer is the aberrations or defects of the optical system, which can arise from sub-optimal design, errors in manufacturing, or misalignment of the optical components in the assembled optical imaging system. As Fig. 1.7(a) shows, in the ideal case spherical waves originating

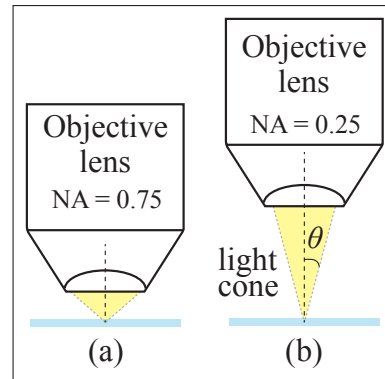


Figure 1.6: Numerical Aperture (NA) of a microscope objective lens in air ($n = 1$). (a) $NA = 0.75$ gives $\theta = 49^\circ$ (b) $NA = 0.25$ gives $\theta = 15^\circ$.

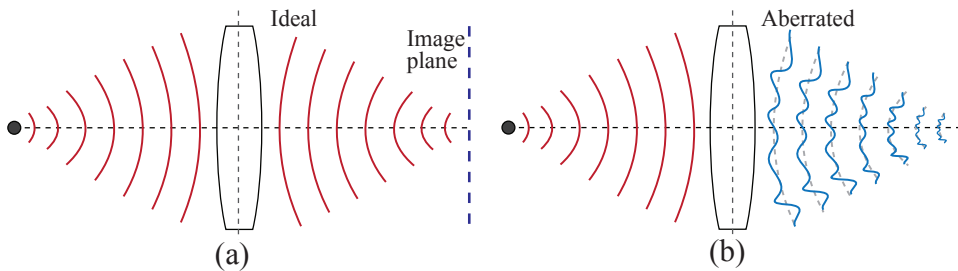


Figure 1.7: (a) Ideal optical system. (b) Aberrated optical system

from the object pass through the optical system and converge as spherical waves to the image plane. In the presence of aberrations, the converging waves deviate from the ideal spherical shape. The deviation of the actual wavefront from the ideal spherical shape is called the aberration function and is measured in units of the wavelength (λ). The Maréchal criterium sets an upper bound on the root mean square value of the aberration function equal to $72 m\lambda$ ($1m\lambda = \lambda / 1000$), which defines the maximum aberration bud-

get below which diffraction-limited performance is maintained. Each aberration type consumes a portion of the budget, but it turns out that the lowest order aberrations have more impact on the overall optical quality. These lowest order aberrations are called the primary aberrations and in Fig. 1.8 it is shown how coma, spherical aberration, and astigmatism degrade the image quality.

In part (a) the diffraction-limited image of a point source is shown. In terms of geometrical optics, all rays converge to a single point at the image plane. This results in a bright spot with a size on the order of λ/NA and diffraction rings around it. For spherical aberration (part b), the focus position varies in the axial direction for rays converging under different angles of incidence which creates a blurry image. In the presence of coma (part c), an off-axis point source is imaged by a comet shaped spot. Astigmatism results from rays in two perpendicular planes not having the same focal point (part d). Therefore they focus at a different axial position instead of at a single axial position.

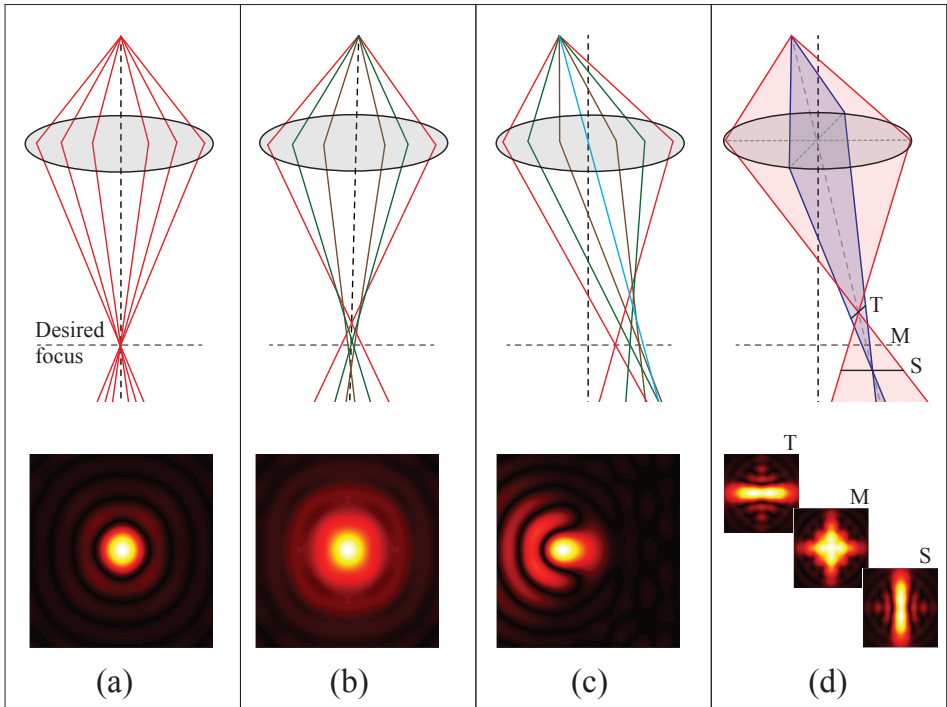


Figure 1.8: The effect of low order primary aberrations in imaging a point source. (a) Diffraction-limited system. (b) Spherical aberration. (c) Presence of coma in off-axis object. (d) Astigmatism and images at three different planes in image space.

Quantifying these aberrations through a non-invasive optical quality test is an important design challenge for WSI system. Such a non-invasive quality assessment of the (optical) image quality can be used to assure the image quality of a scanned tissue slides. A non-invasive approach needs to be practical, fast, and executable without end-user interaction. Only then can it fulfill the need for regular testing of the optical quality of the WSI systems. These aberrations have a specific signature in the so-called Optical

Transfer Function (OTF) which expresses the performance of the optical imaging system as a function of spatial frequency. A thorough analysis of the measured OTF at different focus levels will provide quantitative information about the aberrations of WSI system without the need to use external aberration measurement sensor.

1.3.2. FULL-FIELD ABERRATION MAPS AND ALIGNMENT TEST

The aberrations of an optical imaging system stem from two sources: they are either intrinsic to the optical design or they arise from manufacturing errors of the individual components or misalignment. The part that is intrinsic to the optical design can only be improved by redesigning and changing the components. However, misalignment can be tested and corrected to reduce the total aberration level and thereby optimize the optical image quality. Knowing the root causes of the aberrations reduces the manufacturing costs of WSI systems. The magnitude of individual aberrations (astigmatism, coma) varies as a function of the position in the field of view (FOV) of the optical imaging system. Full-field aberration maps can be measured and analyzed for the effect of different misalignments and in this way can be used as an alignment test. This way of testing was invented by Shack [29] and afterwards developed into what is known as Nodal Aberration Theory (NAT) [30]. The focus of NAT has been on large optical telescopes [30–36], but it applies equally well to any optical imaging system with small field angles such as microscopes. In NAT, a specific role is played by the nodes of the full-field aberration

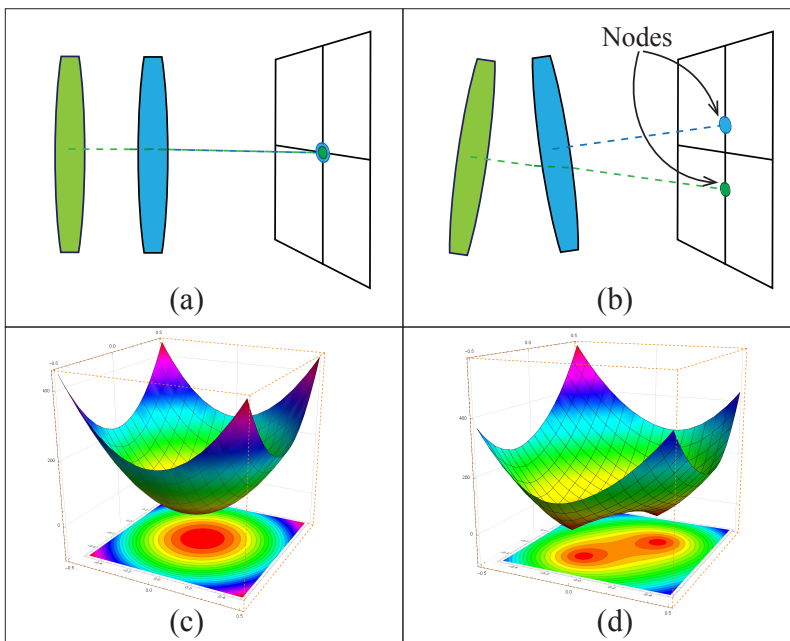


Figure 1.9: Principle of Nodal Aberration Theory. (a) Aligned optical system with two elements. (b) Misaligned optical system in which nodes are away from each other (Adapted from [37]). (c) Field dependency of low order astigmatism for aligned optical system (pure quadratic). (d) Field dependency of low order astigmatism for misaligned optical system with two nodes. This map is a combination of quadratic, linear and constant field dependency.

maps, which are the positions in the field of view with zero aberration. Each optical component of the total optical imaging system has its own aberration map. The overall full-field aberration map of the entire optical system is the sum of all the individual aberration maps of its components. When the system is well-aligned all the nodes are in the center of the FOV (see Fig. 1.9a), therefore the summation will not change the position of the node or create new nodes. However, if components are tilted or decentered with respect to each other, the position of the nodes change (see Fig. 1.9b) so does the full-field aberration map for the entire system. NAT investigates these changes for each type of aberration. For example, the field dependency of the lowest order astigmatism is quadratic and if the optical system is aligned then the resulting map remains quadratic (see Fig. 1.9c). For a misaligned system, there will be an additional node in the astigmatism map (see Fig. 1.9d). For the lowest order coma the field dependency is linear, which implies that misalignment only shifts the single node away from the center of the FOV but does not introduce additional nodes. NAT provides a systematic framework for evaluating misalignment effects in optical imaging systems. This makes NAT an attractive approach to test and correct the alignment of an optical system in practice. Although NAT has been used extensively in aligning multi-mirror telescopes, it has great potential for optical systems like WSI systems, which have only a few optical components (mainly an objective lens and a tube lens). Full-field maps of primary aberrations can reveal and possibly quantify the presence of misalignment errors in the manufacturing stage of WSI systems. The combination of a non-invasive aberration measurement tool and NAT analysis has the potential to facilitate manufacturing and monitoring of WSI systems.

1.3.3. ILLUMINATION

In brightfield microscopy there are two types of illumination: critical and Köhler [38]. In critical illumination the source is imaged by the condenser onto the object plane (Fig. 1.10a). In Köhler illumination, the source is imaged at the aperture stop, which is imaged by the condenser onto the object plane. This way the condenser provides parallel illumination of the object plane. Every point of a spatially extended light source contributes to the illumination of every point in the object plane (Fig. 1.10b). This provides a more uniform illumination and the possibility to control the maximum illumination angle θ by changing the diameter of the aperture stop. This control of the illumination NA of the microscope enables a continuous transition between incoherent imaging and coherent imaging.

For a high illumination NA the imaging is incoherent, for a low NA the imaging is coherent. Somewhere in between, at an intermediate NA, the imaging is partially coherent. It is well known that the spatial frequency cutoff, the sharpness of edges, and the amount of edge overshoot in the image can be tuned by the degree of partial coherence (one minus the ratio of the condenser and objective NA). Partial coherence also has impact on the defocus tolerance. The effect of partial coherence on the edge response and defocus tolerance can be studied via simulation and measurement of the effective OTF derived from the edge response. Such a study can be used to optimize the image quality of WSI systems in terms of sharpness.

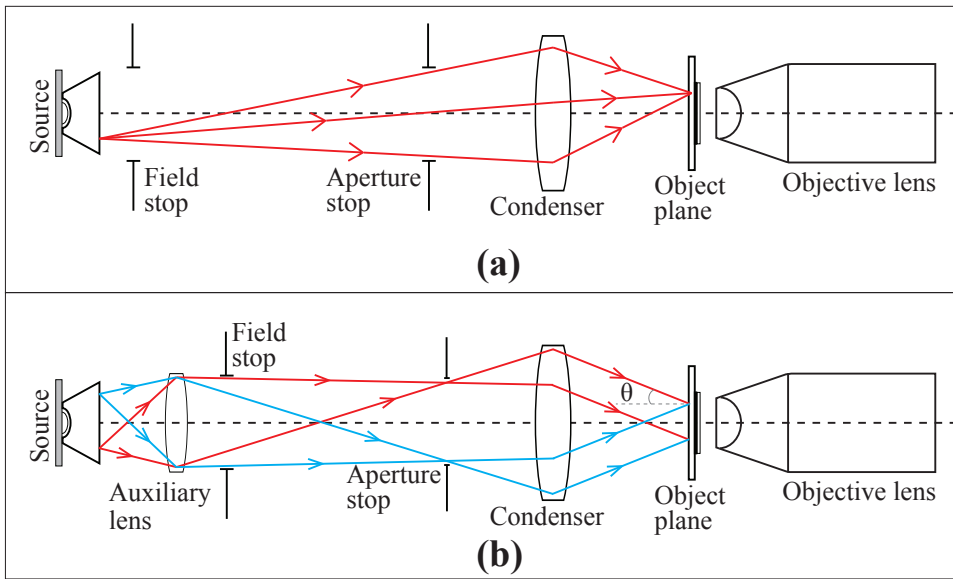


Figure 1.10: Illumination type (adapted from [38]). (a) Critical illumination. (b) Köhler illumination.

1.3.4. FROM 2D TO 3D IMAGING

Most of the current WSI systems record two-dimensional (2D) images of tissue slides, either at a fixed focus or in an autofocus mode [21, 39]. In the fixed focus mode, the imaging optics is focused at one level in the sample and provides a sharp (in-focus) image of just that one fixed optical plane. Tissue slides, however, are not fully flat. The topography of the tissue layer shows peaks and valleys on the order of $10\ \mu\text{m}$, more than the focal depth of about 1 to $2\ \mu\text{m}$. In the fixed focus mode the image of the tissue layer is therefore usually not sharp throughout the image. The autofocus mode overcomes this problem by adjusting the imaging optics in order to track the topography variations of the tissue layer thereby providing an image of a tissue layer that is sharp throughout the entire image. Finding the best focus can be done by image-based approaches [40] in which multiple images at different focus levels are analyzed to define the best focus positions. Depending on the scanning mechanism (line-based or tile-based) the autofocus algorithm varies [40]. The procedure of focus finding must be executed prior to the scanning step, which increases the total scanning time. In a different approach the autofocus imaging components (extra beamsplitter and extra camera) are separated from the WSI scanning engine. In this way, the scanning and autofocus can be done simultaneously which is beneficial for optimizing the overall throughput (Fig. 1.11).

Such an approach is effective in imaging thin tissue slides with a standard thickness of around $4\ \mu\text{m}$ but not for thicker ones, because the autofocus algorithm may have difficulties in finding the "best" focus in layers with significant structural changes in the axial direction. An image of a single focus layer is not sufficient for applications such as cytology in which whole cells need to be imaged. To cover this area, WSI systems can acquire a full z-stack, which provides the user with a 3D virtual slide [39]. This functionality can

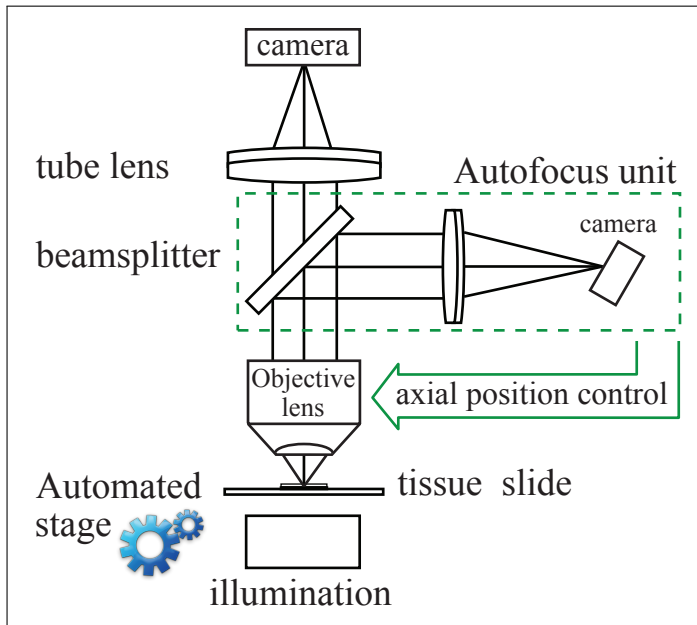


Figure 1.11: A WSI system with separate autofocus unit based on differential measurement [41]. A tilted autofocus camera records multiple sequential images which are used to determine the axial position of the tissue.

bring the benefits of WSI systems to the field of cytology as well [42–44]. There is also a potential benefit in histology for imaging thicker tissue layers (at least two cells thick, i.e. from 10 to 20 μm) or deeper into the tissue layer in helping to elucidate the 3D tissue morphology. Performing multiple scans to acquire a through-focus image stack for a 3D virtual slide increases the scanning time and also the already huge file sizes. In addition, light originating from out-of-focus layers reduces the contrast of the images and lowers the quality of 3D virtual slides. One way to overcome this is to use image post-processing methods such as 3D image deconvolution [45, 46].

Considering these factors (scanning time, image size and image quality) the currently available 3D imaging solutions are not on par with 2D WSI systems. A technical challenge would be to devise a scanner architecture that does concurrent scanning and autofocus signal generation without a separate camera for autofocus. Additionally a simplified way to image tissue slides in 3D could provide further benefits.

1.4. THESIS CHALLENGES & OUTLINE

The main goal of this thesis is to design, build and characterize a modular platform for a WSI system for application in the emerging field of digital pathology. This platform is to conduct good quality brightfield microscopy, the most common modality in this field, and to obtain 2D as well as 3D images of tissue slides. To attain this goal, we faced the following challenges during the course of this project:

- Developing a non-invasive systematic approach to test and quantify the optical quality of WSI systems without the need for an external aberration measurement instrument.

- Contriving a procedure to verify the previously proposed approach using a well established aberration sensor and developing a method to test the alignment of the optical components in WSI systems.
- Optimizing the partial coherence of a LED-based illumination unit for WSI systems.
- Building an experimental WSI platform for studying 2D and 3D multicolor bright-field microscopy of tissues slides with different staining and thickness.

These challenges have been addressed in this thesis as outlined below:

In **chapter 2** we present a method for testing and monitoring the optical quality of WSI systems using the through-focus Optical Transfer Function (OTF) obtained from the edge response of a custom-made resolution target. This enables quantitative analysis of a number of primary aberrations such as spherical aberration, coma, astigmatism and field curvature. We use the method to compare different tube lens designs and to study the effect of objective lens aging. The results are compared with direct measurement of aberrations based on Shack-Hartmann wavefront sensing.

In **chapter 3**, we analyze a full-field aberration maps measured by Shack-Hartmann sensor to find the root cause of the aberrations in WSI systems. Our approach inspired by methods developed for analyzing and quantifying misalignment in optical telescopes through the analysis of the measured aberrations across the field of view. We present the analysis of such full-field aberration maps for revealing different misalignments such as decenter and tilt of optical components for configurations with intentional misalignment.

We have assumed that the WSI system acts as an incoherent optical imaging system in our OTF-based optical quality test. In reality brightfield microscopy systems are partially coherent and our assumption is reasonable only for a condenser NA about equal to or higher than the objective lens NA. In **chapter 4** we present a further investigation into the effect of partial coherence on the optical quality of the system. We designed and constructed a very compact Köhler condenser with variable NA to test the effect of partial coherence on the edge response and defocus tolerance. We have designed and built a three-color sequential LED-based illumination unit. We characterized this unit in terms of light profile across the object plane and spectrum. This design enables us to perform color-sequential RGB imaging using one camera with a line rate of up to 100 KHz.

The majority of WSI systems for digital pathology are 2D slide scanners. A high scanning rate and full (RGB) color imaging is made possible by using separate line-scan camera for each of the three color channels. The drawbacks of such a system are difficulties in the optical path alignment, color layer registration and also system maintenance. In addition, autofocus operation requires 3D information, which can be obtained either from multiple scans at different object heights or by yet another camera used for that purpose. Moreover, inspection of 2D digital slides differs from viewing through the eyepiece of a conventional microscope by the lack of a focus knob, while viewing back-and-forth through focus is often used by pathologists. For these reasons 3D scanning of tissue slides is a definite need for digital pathology. We address this need in **chapter 5** by introducing a novel scanner platform in which a single image sensor replaces all the cameras of the old architecture and enables single-scan 3D imaging. We presented a full system characterization along with the design details of a new LED-based 5-channel color-

sequential illumination unit. We evaluated the performance of our setup by scanning tissue slides with different staining concentration and thicknesses up to 100 μ m. Finally, we also present two new computational imaging techniques made possible with this scanner architecture. The first is a color-segmentation approach using the five recorded colors for segmenting images of multiple stained tissues. The second is quantitative phase imaging of unstained tissues from a through focus 3D image stack.

Finally in **chapter 6** we conclude and then discuss future directions of WSI systems and speculate on potential applications of our novel 3D WSI platform.

REFERENCES

- [1] A. H. Fischer, K. A. Jacobson, J. Rose, and R. Zeller, *Hematoxylin and eosin staining of tissue and cell sections*, Cold Spring Harbor Protocols **2008** (2008).
- [2] *National cancer institute website, U.S.A*, www.cancer.gov (2016).
- [3] *Webpathology, visual survey of surgical pathology*, www.webpathology.com (2016).
- [4] S. Thorstenson, J. Molin, and C. Lundstrom, *Implementation of large-scale routine diagnostics using whole slide imaging in Sweden: Digital pathology experiences 2006-2013*, Journal of Pathology Informatics **5**, 14 (2014).
- [5] P. W. Hamilton, Y. Wang, and S. J. McCullough, *Virtual microscopy and digital pathology in training and education*, Acta Pathologica, Microbiologica, et Immunologica Scandinavica **120**, 305–315 (2012).
- [6] K. Foster et al., *Medical education in the digital age: Digital whole slide imaging as an e-learning tool*, Journal of Pathology Informatics **1**, 14 (2010).
- [7] L. Pantanowitz and A. V. Parwani, *Education*, in *Digital Pathology* (Springer, 2016).
- [8] E. A. Krupinski, A. K. Bhattacharyya, and R. S. Weinstein, *Telepathology and digital pathology research*, in *Digital Pathology* (Springer, 2016).
- [9] P. W. Hamilton, et al., *Digital pathology and image analysis in tissue biomarker research*, Methods **70**, 59–73 (2014).
- [10] T. C. Cornish, R. E. Swapp, and K. J. Kaplan, *Whole-slide imaging: routine pathologic diagnosis*, Advances in Anatomic Pathology **19**, 152–9 (2012).
- [11] B. Têtu, D. C. Wilbur, L. Pantanowitz, and A. V. Parwani, *Teleconsultation*, in *Digital Pathology* (Springer, 2016).
- [12] G. R. Lauro, et al., *Digital pathology consultations—a new era in digital imaging, challenges and practical applications*, Journal of Digital Imaging **26**, 668–677 (2013).
- [13] N. C. Jones, et al., *Interinstitutional whole slide imaging teleconsultation service development: Assessment using internal training and clinical consultation cases*, Archives of Pathology and Laboratory Medicine **139**, 627–635 (2014).

- [14] T. W. Bauer and R. J. Slaw, *Validating whole-slide imaging for consultation diagnoses in surgical pathology*, *Archives of Pathology and Laboratory Medicine* **138**, 1459–1465 (2014).
- [15] F. Ghaznavi, A. Evans, A. Madabhushi, and M. Feldman, *Digital imaging in pathology: whole-slide imaging and beyond*, *Annual Review of Pathology: Mechanisms of Disease* **8**, 331–359 (2013).
- [16] S. Al-Janabi, et al., *Digital pathology: current status and future perspectives*, *Histopathology* **61**, 1–9 (2012).
- [17] M. Kowal, P. Filipczuk, A. Obuchowicz, J. Korbicz, and R. Monczak, *Computer-aided diagnosis of breast cancer based on fine needle biopsy microscopic images*, *Computers in biology and medicine* **43**, 1563–1572 (2013).
- [18] L. Langer, et al., *Computer-aided diagnostics in digital pathology: automated evaluation of early-phase pancreatic cancer in mice*, *International Journal of Computer Assisted Radiology and Surgery* **10**, 1043–1054 (2015).
- [19] C. Castaneda, et al., *Clinical decision support systems for improving diagnostic accuracy and achieving precision medicine*, *Journal of Clinical Bioinformatics* **5**, 1 (2015).
- [20] C. Mosquera-Lopez, S. Agaian, A. Velez-Hoyos, and I. Thompson, *Computer-aided prostate cancer diagnosis from digitized histopathology: A review on texture-based systems*, *Biomedical Engineering, IEEE Reviews in* **8**, 98–113 (2015).
- [21] J. R. Gilbertson, et al., *Primary histologic diagnosis using automated whole slide imaging: a validation study*, *BMC Clinical Pathology* **6** (2006).
- [22] J. Webster and R. Dunstan, *Whole-slide imaging and automated image analysis considerations and opportunities in the practice of pathology*, *Veterinary Pathology Online* **51**, 211–223 (2014).
- [23] A. V. Parwani, L. Hassell, E. Glassy, L. Pantanowitz, et al., *Regulatory barriers surrounding the use of whole slide imaging in the united states of america*, *Journal of Pathology Informatics* **5**, 38 (2014).
- [24] R. Randell, R. Ruddle, and D. Treanor, *Barriers and facilitators to the introduction of digital pathology for diagnostic work*, *Studies in Health Technology and Informatics* **216**, 443–447 (2015).
- [25] L. Pantanowitz, et al., *Validating whole slide imaging for diagnostic purposes in pathology: guideline from the college of American pathologists pathology and laboratory quality center*, *Archives of Pathology and Laboratory Medicine* **137**, 1710–1722 (2013).
- [26] D. R. Snead, et al., *Validation of digital pathology imaging for primary histopathological diagnosis*, *Histopathology* (2015).

- [27] T. C. Cornish, *An introduction to digital whole slide imaging and whole slide image analysis*, Practical Pathology Workshop (2013).
- [28] N. Farahani, A. Parwani, and L. Pantanowitz, *Whole slide imaging in pathology: advantages, limitations, and emerging perspectives*, Pathology and Laboratory Medicine International **7**, 23–33 (2015).
- [29] R. V. Shack and K. Thompson, *Influence of alignment errors of a telescope system on its aberration field*, Proc. SPIE, 24th Annual Technical Symposium **0251**, 146–153 (1980).
- [30] K. Thompson, *Description of the third-order optical aberrations of near-circular pupil optical systems without symmetry*, J. Opt. Soc. Am. A **22**, 1389–1401 (2005).
- [31] T. Schmid, *College of Optics and Photonics*, Ph.D. thesis, University of Central Florida, Orlando, Florida (2010).
- [32] K. P. Thompson, T. Schmid, O. Cakmakci, and J. P. Rolland, *Real-ray-based method for locating individual surface aberration field centers in imaging optical systems without rotational symmetry*, J. Opt. Soc. Am. A **26**, 1503–1517 (2009).
- [33] K. P. Thompson, T. Schmid, and J. P. Rolland, *Recent discoveries from nodal aberration theory*, International Optical Design Conference **7652**, 76522Q (2010).
- [34] J. Wang, B. H. Guo, Q. Sun, and Z. W. Lu, *Third-order aberration fields of pupil decentered optical systems*, Opt. Express **20**, 11652–11658 (2012).
- [35] Z. Gu, C. Yan, and Y. Wang, *Alignment of a three-mirror anastigmatic telescope using nodal aberration theory*, Opt. Express **23**, 25182–25201 (2015).
- [36] R. W. Gray, *Investigation of the field dependence of the aberration functions of rotationally nonsymmetric optical imaging systems*, Ph.D. thesis, Engineering and Applied Sciences (2015).
- [37] J. R. Rogers, *Techniques and tools for obtaining symmetrical performance from tilted-component systems*, Optical Engineering **39**, 1776–1787 (2000).
- [38] M. Born and E. Wolf, *Principles of Optics* (Cambridge University, 1999).
- [39] M. G. Rojo, G. B. Garcia, C. P. Mateos, J. G. Garcia, and M. C. Vicente, *Critical comparison of 31 commercially available digital slide systems in pathology*, International Journal of Surgical Pathology **14**, 285–305 (2006).
- [40] M. C. Montalto, R. R. McKay, R. J. Filkins, et al., *Autofocus methods of whole slide imaging systems and the introduction of a second-generation independent dual sensor scanning method*, Journal of Pathology Informatics **2**, 44 (2011).
- [41] B. Hulsken, *Autofocus based on differential measurements*, US Patent App. 13/805,555 (2011).

- [42] E. A. El-Gabry, A. V. Parwani, and L. Pantanowitz, *Whole-slide imaging: widening the scope of cytopathology*, *Diagnostic Histopathology* **20**, 456–461 (2014).
- [43] W. E. Khalbuss, L. Pantanowitz, and A. V. Parwani, *Digital imaging in cytopathology*, *Pathology Research International* **2011** (2011).
- [44] T. Kalinski, et al., *Virtual 3D microscopy using multiplane whole slide images in diagnostic pathology*, *American Journal of Clinical Pathology* **130**, 259–264 (2008).
- [45] D. S. Biggs, *3D deconvolution microscopy*, *Current Protocols in Cytometry* , 12–19 (2010).
- [46] J. G. McNally, T. Karpova, J. Cooper, and J. A. Conchello, *Three-dimensional imaging by deconvolution microscopy*, *Methods* **19**, 373–385 (1999).

2

OPTICAL QUALITY ASSESSMENT OF WHOLE SLIDE IMAGING SYSTEMS FOR DIGITAL PATHOLOGY

Whole Slide Imaging (WSI) systems are high-throughput automated microscopes for digital pathology applications. We present a method for testing and monitoring the optical quality of WSI-systems using a measurement of the through-focus Optical Transfer Function (OTF) obtained from the edge response of a custom made resolution target, composed of sagittal and tangential edges. This enables quantitative analysis of a number of primary aberrations. The curvature of the best focus as a function of spatial frequency is indicative for spherical aberration, the argument of the OTF quantifies for coma, and the best focus as a function of field position for sagittal and tangential edges allows assessment of astigmatism and field curvature. The statistical error in the determined aberrations is typically below 20 mλ. We use the method to compare different tube lens designs and to study the effect of objective lens aging. The results are in good agreement with direct measurement of aberrations based on Shack-Hartmann wavefront sensing with a typical error ranging from 10 mλ to 40 mλ.

2.1. INTRODUCTION

THE primary activity of a pathologist is to make diagnoses via microscopic examination of tissue and cells from a biopsy. In the emerging clinical practice of digital pathology [2–5] this is based on digital high-resolution images of tissue slides acquired with a high-resolution and high-throughput automated microscope, the Whole Slide Imaging (WSI) system. These systems are designed for imaging a postage stamp sized area on a glass slide with a sampling density down to $0.25 \mu\text{m}/\text{pixel}$ in about 1 min. Digital pathology comprises a number of applications such as connectivity for remote diagnosis in regional hospital cooperation or for expert consultations, connectivity for correlating pathology images with radiology data, workflow management and quality control [6], teaching and certification, and the use of Computer Aided Diagnostics (CAD) and Clinical Decision Support (CDS) [7–10].

A number of different optical architectures have been considered for WSI systems [11], from a step-and-stitch approach using standard widefield acquisitions, to array microscopy [12], and architectures based on continuous scanning with a line sensor (“pushbroom” scanning). The latter approach (see Fig. 2.1) is often implemented using Time Delay Integration (TDI) cameras [13], for increasing the Signal-to-Noise-Ratio (SNR). The SNR-increment originates from a more efficient use of the illumination etendue. The line scanner approach has appeared to be the most favoured architecture because of the mechanical simplicity and the reduced need for stitching (if any at all).

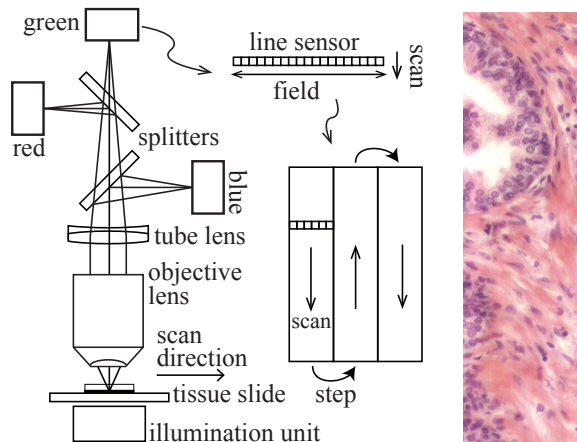


Figure 2.1: Schematic layout of the home-built line sensor based WSI system (left) and an image acquired with the setup (right).

The optical quality of any WSI system is the key to guaranteeing the best possible image quality of the final digital slide images. For that reason there is a need for testing and monitoring optical quality in manufacturing and during the operational lifetime of the instrument. This systematic optical quality assessment must give access to many optical parameters, e.g. primary aberrations including astigmatism, field curvature, spherical aberration, coma, and chromatic aberrations. In addition, it must be cost effective and practical, i.e., run without end-user intervention or modification of the hardware setup

of the scanner.

A non-invasive method that satisfies these requirements is based on the evaluation of the Modulation Transfer Function (MTF) derived from features such as edges or line patterns on a resolution target [14, 15]. A through-focus measurement is advisable to assess the effects of field curvature and tilt of the image plane around the scan direction. These may result in a focus mismatch between the center and the edge of a scanned lane and between two adjacent scan lanes, respectively. Although optical quality assessment can be done based on the MTF data alone, it is desirable to extract the basic optical information, i.e. to estimate the optical aberrations underlying a possible deterioration of the MTF. A general way to extract the aberrations is to fit a model MTF, that is a function of the aberrations, to the MTF data [16, 17]. The drawback of iterative aberration retrieval from MTF data is that convergence to the global optimum is not guaranteed, and that convergence to an optimum can be rather slow. Hence there is a need for a more simple and straightforward way to estimate aberrations from through-focus MTF data.

Here, we propose a method that addresses this need. First of all, we find the best focus as a function of both field position and spatial frequency from the through-focus MTF. In this way we can directly quantify astigmatism and field curvature (from the dependence on field position). We add to this the novel aspect of extracting the spherical aberration from the dependence of best focus on spatial frequency. Second, we introduce a new way to estimate coma, namely by measuring the full Optical Transfer Function (OTF). It turns out that coma can be estimated from the dependence of the argument of the OTF - the Phase Transfer Function (PTF) - evaluated at best focus on the spatial frequency. Few studies have been made into the use of the PTF for analyzing optical image quality [18, 19], none of them address the quantification of coma.

In our paper we give two examples for the use of the proposed OTF-based optical image quality assessment. A first example concerns the evaluation of tube lens design, which is highly relevant to WSI-systems. Non-standard tube lenses are required in order to achieve a required sampling density in object space (the slide). For example, an Olympus 20 \times /0.75 objective lens has a focal length of 180 mm/20 \times = 9 mm. For a required sampling density of 0.25 μ m/pixel and a camera pixel size of 7 μ m a tube lens with a focal length of 252 mm is then needed. This is significantly different from the standard 180 mm tube lens focal length of Olympus. Similar arguments hold for other manufacturers of high-end objective lenses. Now the complication arises of balancing the low order aberrations (field curvature, astigmatism, axial and lateral color) between objective lens and tube lens, i.e. the objective lens may suffer from these aberrations as long as they are compensated by aberrations of the tube lens that are equal in magnitude but of opposite sign. This balancing may be done differently for different manufacturers. Now the question arises how well the custom tube lens with the required magnification matches the given off-the-shelf high-end objective lens. We apply our method to compare two simple tube lens designs, namely the use of a single catalogue achromat, and two back-to-back achromats of twice the required focal length. This example has implications for the use of home-built microscope systems around the world, as such simple tube lenses are often used. The second example relates to monitoring of aging in imaging systems and to detecting defective objective lenses. We show results for an old and possibly maltreated objective lens for quantifying the degree of sub-standard optical quality.

The proposed method of extracting aberrations is implemented for a push-broom scanning system based on a line sensor, but can in principle also be applied to an ordinary widefield non-scanning system based on an area sensor. The difference between the two optical architectures is that the former has translational invariance in the scan direction, whereas the latter does not. We have used this to our advantage by averaging over features (edges) of the resolution target in the scan direction, thereby increasing the SNR. The outline of this paper is as follows. Section 2 describes the methods, in particular the design of the resolution target, the measurement of the OTF from a through-focus image stack, and the extraction of aberration coefficients from the measured OTE. Section 3 presents the results on the two aforementioned examples as well as on a validation experiment with a Shack Hartmann wavefront sensor. The paper is concluded in section 4 with a short discussion and outlook on possible follow-up research.

2.2. METHODS

2.2.1. SCANNING AND IMAGE ACQUISITION

The WSI lab-system [Fig. 2.1] uses Dalsa Piranha HS-40-04k40 TDI line scan sensors (4096 pixels, pixel size $7\mu\text{m}\times 7\mu\text{m}$, maximum frame rate 36kHz), Nikon 20X/NA0.75 Plan apochromat and Olympus 20X/NA0.75 UPlanSApo objective lenses, tube lenses assembled from the Thorlabs catalogue AC508-250-A-ML (250 mm focal length) and AC508-500-A (500 mm focal length) achromat lenses, a PI M-505 low profile translation stage (for positioning of the slide in the field direction), a Newport XM1000 ultra precision linear motor stage (for the scanning motion of the slide), a PI M-111 compact micro-translation stage (for coarse positioning of the objective lens in the axial direction), and a PI P-721.CL0 piezo nano-positioner (for fine positioning of the objective lens in the axial direction). The illumination was based on LEDs and a condenser matched in NA to the objective lens. It provides red, green, blue light with maximum power at 618, 565, and 435 nm respectively. The corresponding spectral full width at half maximum are 93, 67, and 27 nm.

2.2.2. OTF MEASUREMENT

The use of the edge response for measuring the MTF is a standard technique [14, 15, 20, 21]. Here, we use the through-focus edge response of a custom made resolution target [Fig. 2.2(a)] to measure the full OTF. The target pattern is etched in a thin chrome mask on a Soda Lime glass (B270) substrate with thickness of 1 ± 0.015 mm. A D236 glass cover slip of thickness 0.17 ± 0.015 mm is glued on top of it with UV-curing glue and coated with an antireflection coating. The etched lines have a width of 50 ± 0.8 μm giving a spatial frequency of 10 line pairs/mm. Typically, we use stacks of 170 images recorded at 0.1 μm axial step size of the objective lens. Edges oriented along the scan and field directions are used for measuring the sagittal and tangential response. Different Regions Of Interests (ROIs) for measuring the OTF are shown in Fig. 2.2(a). The ROIs indicated in red give the response for the left, middle and right of the objective lens' Field Of View (FOV). The ROIs indicated in blue serve to assess the field curvature and astigmatism. Prior to scanning, the glass slide is aligned to be perpendicular to a mechanical reference, namely the translation axis of the objective lens piezo stage. Keeping reference marks at

the edges of the glass slide at the same focus level for a single position in the FOV of the objective lens when the slide is translated laterally does this.

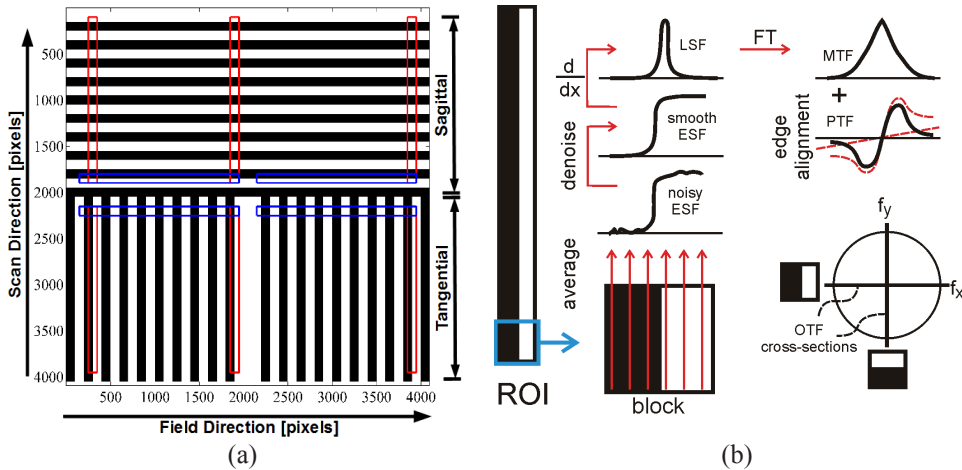


Figure 2.2: Schematic layout of the home-built line sensor based WSI system (left) and an image acquired with the setup (right).

Each ROI consists of several blocks of 100×100 pixels. To each block we apply a number of image processing steps [Fig. 2.2(b)]. The first step is averaging of the 100 line profiles to get a one dimensional Edge Spread Function (ESF) for each block. Possible misalignment of the orientation of the target around the optical axis (normal to the slide) may be neglected on the scale of the 100 lines. The second step is to reduce the noise in the upper and lower plateaus of the ESF without affecting the edge. The guided filter algorithm is used to this end [22]. This filter has four inputs: input line response, guidance image, local window size and regularization parameter. If the guidance image is equal to the filter input ESF then the filter acts as an edge preserving operator. Here the averaged edge response is the guidance image and the mean of the scaled standard deviations of the top and bottom plateaus is chosen for the regularization parameter. So the higher the noise, the more smoothing away from the edge. Possible biases in the ESF and the resulting OTF introduced by the denoising have been checked for by evaluating OTFs with and without application of the guided filter operation. No biases were found, only the expected difference in noise level of the resulting OTF data. The third step is to calculate the line spread function (LSF) from the denoised edge response by numerical differentiation. Here, the discrete difference must be divided by a correction factor $\text{sinc}(\pi a f / 2)$, with f the spatial frequency and the pixel size [23]. The fourth step computes the 1D Fourier Transform (FT) of the LSF to get a cross section through the origin of the OTF. The modulus and the argument of the OTF then yield the MTF and the PTF, respectively. A fifth step is needed to correct for a possible shift of the center of the LSF from the computational window of the FT. Such a shift Δx leads to a linear phase

contribution $2\pi f \Delta x$ to the PTF. This shift is estimated by:

$$\Delta x_{est} = \arg \min_{\Delta x} \left\{ \sum_f W(f) (PTF(f) + \text{rem}(2\pi f \Delta x, 2\pi))^2 \right\} \quad (2.1)$$

where $\text{rem}(a, b)$ indicates the remainder after division a/b . The weight function $W(f)$ is taken to be equal to the MTF.

After computing the MTF and PTF for all individual blocks in a given ROI, the MTF of the ROI is calculated by averaging over all MTFs. Repeating the procedure with a different weight function increases the accuracy of the linear phase removal. Namely, now the weight is the inverse variance of the PTFs of the set of blocks in the ROI. In addition, the weights of the spatial frequencies beyond the onset of aliasing [19] are reduced with a factor of 10. After this refined linear phase removal the PTF of the ROI is found by averaging over all PTFs of the different blocks. The statistical error in the MTF and PTF is found by the standard deviation of the MTF and PTF over the blocks within the ROIs. Note that the current procedure does not provide a measurement of the OTF for all two-dimensional spatial frequencies (f_x, f_y) but only the cross-sections OTF_x and OTF_y along the lines $f_y = 0$, and $f_x = 0$, respectively.

2.2.3. ABERRATION EXTRACTION

The proposed method can be explained from the salient features of the through-focus MTF and PTF affected by the different primary aberrations, as shown in Fig. 2.3. Aberration values reported throughout this paper are standard Zernike coefficients [24], corresponding in magnitude with the Root Mean Square (RMS) value but with the sign maintained of the Zernike fringe coefficients. The route to aberration quantification runs via the extraction of the best focus (optimum MTF) as a function of spatial frequency and position in the FOV of the objective lens. The best focus for a given spatial frequency is found by a Weighted Least Squares (WLS) fit of a parabola to five data points (focus level for which the MTF is maximum and its four neighbors) with weights equal to the inverse of the measurement variances of the data points. The maximum of the fitted parabola yields the best focus position for that spatial frequency. The uncertainty is found from the measured MTF standard deviation by standard error propagation.

Spherical aberration introduces curvature in the best focus as a function of spatial frequency: the best focus is shifted toward the marginal rays' focus for low and high spatial frequencies [Fig. 2.3(b)]. This effect can be quantified by fitting a parabola to the best focus line (using again a WLS fit):

$$z_{opt}(f_x) = \left[p_1 \left(\frac{\lambda}{NA} f_x \right)^2 + p_2 \frac{\lambda}{NA} f_x + p_3 \right] \frac{\lambda}{1 - \sqrt{1 - NA^2}} \quad (2.2)$$

where λ is the wavelength and NA the Numerical Aperture of the objective lens. Scaling of the spatial frequencies with NA/λ and scaling of the best focus position with the depth-of-focus [25] ensures that the coefficients (p_1, p_2, p_3) are largely independent of wavelength and NA . We found that p_1 is linearly dependent on the Zernike spherical aberration coefficient ($p_1/A_{40} = 0.0104/m\lambda$).

The overall best focus is found by weighted averaging (weighted by the inverse square error) of the best focus line over the middle frequency range ($0.90 \geq MTF \geq 0.10$). Plotting the best focus as a function of the position in the FOV of the objective lens, for both the sagittal and tangential ROIs gives direct access to field curvature and astigmatism. The level of astigmatism can be quantified by the axial distance Δz_{ob} between the best

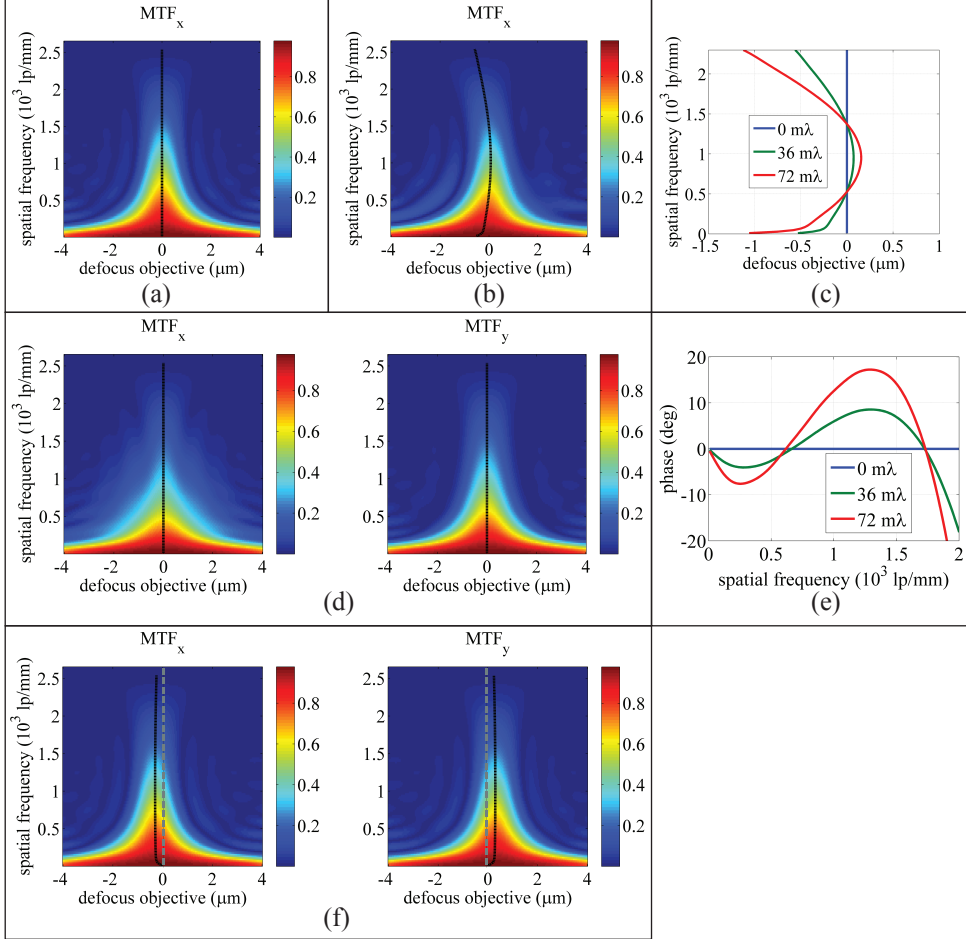


Figure 2.3: Effect of primary aberrations on the through focus OTF ($NA=0.75$, $\lambda=565\text{nm}$). (a) Through-focus MTF in an ideal optical system. (b) Through-focus MTF with spherical aberration of $36m\lambda$. (c) Best focus line with spherical aberration of 0, 36 and $72m\lambda$ (d) Through-focus MTF with coma of $72m\lambda$ in the x direction (e) PTF at the best focus with coma of 0, 36 and $72m\lambda$ (f) Through-focus MTF with astigmatism of $72m\lambda$ at 0 deg.

focus for the sagittal and tangential regions. This distance can be related to a value for the Zernike standard aberration coefficient A_{22} using the method of minimum RMS value of the aberration function [26, 27]. The aberration function including astigmatism and defocus is:

$$W(x, y) = \sqrt{6} A_{22}(x^2 - y^2) + z_{ob}[1 - \sqrt{1 - NA^2(x^2 + y^2)}], \quad (2.3)$$

where z_{ob} is the objective lens axial position, and x and y are the pupil coordinates normalized with the pupil radius. The best sagittal and tangential focus positions are found by minimizing the RMS value of the aberration functions $W(x, 0)$ and $W(0, y)$, i.e. along the lines $y = 0$ and $x = 0$ in the pupil plane. Details of the procedure are outlined in the appendix. The final outcome is a relation $A_{22} = S(NA)\Delta z_{ob}$. In the paraxial regime we have $S(NA) \approx NA^2/4/\sqrt{6}$, for the current objective lenses with $NA = 0.75$ we find $S(NA) = 0.0669$. The field curvature is measured from the overall best focus position for each sub block of the horizontal blue ROIs (see Fig. 2.2(a)). Ideally, this curve will be parabolic and symmetric with respect to the center of the FOV. Since we aligned the slide to be perpendicular to the mechanical symmetry axis of the objective lens, any asymmetry in the field curvature is indicative for tilt or decenter of individual optical components, such as the lenses within the objective lens assembly. The field curvature is quantified by the difference FC_{edge} between the average of the sagittal and tangential best focus values at the edge of the FOV from the best focus in the center of the FOV, after removal of any focus plane tilt.

Coma does not alter the ideal straight best focus line, as opposed to the previously treated cases it is an odd aberration. Although the MTF at the best focus is reduced by coma, the PTF appears to be a better indicator for this aberration. It turns out that the PTF as a function of spatial frequency can be qualitatively described by a third order polynomial [Fig. 2.3(e)], with a distinct maximum and minimum in the range of spatial frequencies below the cutoff. Interestingly, it appears that the difference $\Delta PTF = PTF_{max} - PTF_{min}$ depends linearly on the Zernike coefficient for coma (with coefficient $\Delta PTF/A_{31} = 0.340 \text{ deg}/m\lambda$), but not on wavelength and NA , at least for aberration levels below approximately $120 \text{ m}\lambda$. The error in the measured coma directly follows from the standard deviation in the measured PTF.

2.2.4. SHACK-HARTMANN MEASUREMENTS

The set of aberrations measured from the through-focus OTF are compared to Shack-Hartmann (SH) measurements for verification. We built a wavefront sensing setup using an Optocraft SHR-150-CL SH-sensor (12 bit, detection area $11.8 \times 8.9 \text{ mm}^2$, 78×59 microlens array) to measure the aberrations of the optical system under inspection [Fig. 2.4]. A pinhole ($5 \mu\text{m}$ diameter) mounted in between a glass slide and a coverslip is used as a point source object. In order to provide a (near) parallel wavefront to the SH sensor an additional collimating lens (Melles Griot 01LAO536 - 120mm focal length) is placed at its focal distance from the system's image plane. We measured the aberrations of this collimating lens separately to offset the final results. The aberrations for different positions in the FOV of the objective lens can be probed by laterally translating the pinhole slide.

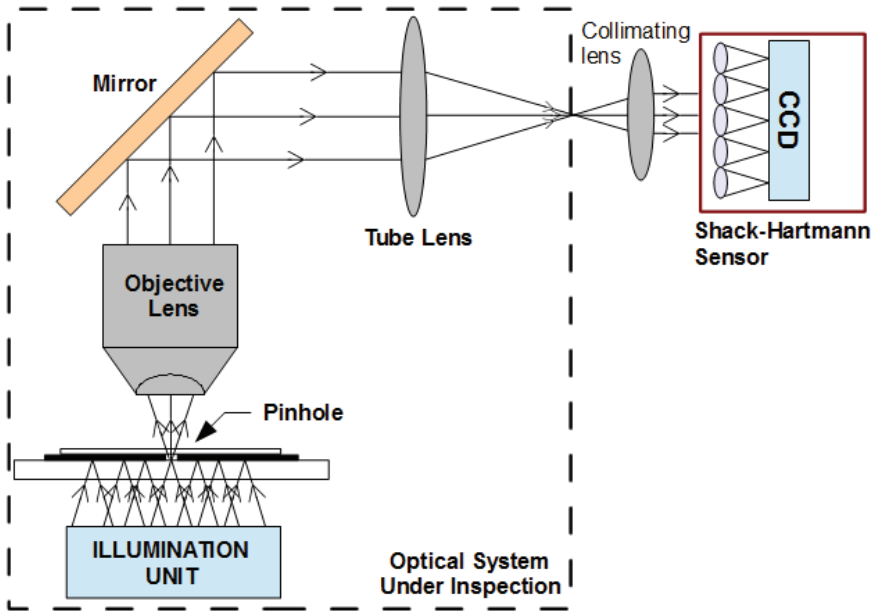


Figure 2.4: Schematic layout of Shack-Hartmann setup for validation of the proposed method.

2.3. RESULTS

2.3.1. EFFECT OF THE TUBE LENS DESIGN

WSI-systems require custom tube lenses in order to achieve a required sampling density, as discussed in the introduction. We considered two simple tube lens designs: a single achromat (Thorlabs AC508-250-A-ML, 250 mm focal length) and double back-to-back achromat design (two Thorlabs AC508-500-A, 500 mm focal length). Simulation of these designs using Zemax ray tracing software (see Fig. 2.5) shows that the astigmatism and field curvature for the double back-to-back achromat design are $-0.57\mu\text{m}$ and $-0.21\mu\text{m}$ at 0.5mm field position, respectively, compared to $+1.6\mu\text{m}$ and $+1.99\mu\text{m}$ for the single achromat design. This is a reduction with a factor 2.8 in astigmatism and 9.5 in field curvature.

In our experiment we used Nikon 20x/0.75 objective lenses (focal length $200\text{mm}/20 = 10\text{mm}$) leading to a sampling density of $0.28\mu\text{m}/\text{pixel}$ for a 250 mm focal length tube lens. The reason for selecting Nikon objective lenses is the reputed absence of balancing of low order aberrations between objective lens and tube lens, implying that the aberrations of the tube lens should match with the aberrations of the composite objective plus tube lens system. The measurements were done with green light with peak wavelength $\lambda = 565\text{nm}$. Our experimental result for the single achromat tube lens (case A) and the double back-to-back achromat tube lens design (case B) are shown in Fig. 2.6 and Fig. 2.7. The measured sampling densities were 0.28 and $0.27\mu\text{m}/\text{pixel}$ for case A and B, respectively, close to the design value.

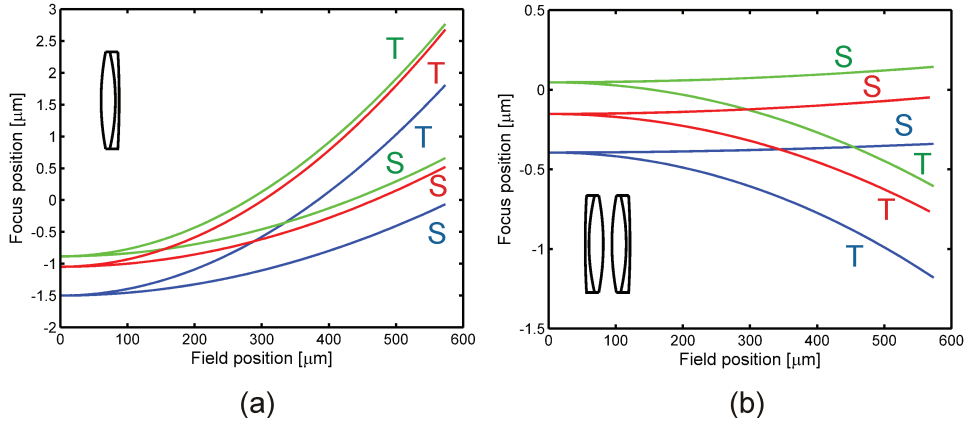


Figure 2.5: Result of Zemax simulation for field curvature and astigmatism. T and S stand for the tangential and sagittal best focus, respectively. Blue, green and red pairs are for 435, 565 and 618nm wavelength. (a) Single achromat. (b) Double back to back achromat design. Notice the different scales in (a) and (b).

The best focus lines in Fig. 2.6(a) and Fig. 2.7(a) show little curvature, which is indicative for low values of spherical aberration (measured values 16 ± 10 and 35 ± 8 $m\lambda$ averaged over the two middle ROIs). The erratic behavior of the best focus line at spatial frequencies close to the cutoff in the tangential right ROI of Fig. 2.6(a) is due to the low and noisy MTF values at those frequencies (signal to noise ratio below ~ 10 dB). The measured PTFs (Fig. 2.6(b) and Fig. 2.7(b)) indicate that the level of coma is also low. The measured values for the left, middle and right ROIs are for case A: 7 ± 10 $m\lambda$, 7 ± 12 $m\lambda$, and 5 ± 10 $m\lambda$ in the sagittal area, 48 ± 8 $m\lambda$, -7 ± 12 $m\lambda$, and -57 ± 8 $m\lambda$ in the tangential area, and for case B: 9 ± 10 $m\lambda$, 13 ± 12 $m\lambda$, and 9 ± 10 $m\lambda$ in the sagittal area, 42 ± 3 $m\lambda$, -8 ± 9 $m\lambda$, and -37 ± 3 $m\lambda$ in the tangential area.

There is, however, a significant amount of astigmatism and field curvature. First, it is noted that the tangential and sagittal best focus curves are significantly asymmetric (Figs. 2.6c and 2.7c), while the slide tilt is near zero (Figs. 2.6d and 2.7d), pointing to a tilt of the objective lens' optical axis w.r.t. its mechanical symmetry axis on the order of 1-2 $mrad$. We measured a field curvature $FC_{edge} = 1.38 \mu m$ for case A, compared to -0.13 μm for case B, also in reasonable agreement with the Zemax design. The astigmatism quantified by the average difference in sagittal and tangential best focus at ± 0.5 mm field position is 0.99 μm for case A, compared to -0.41 μm for case B, in reasonable agreement with the Zemax design. The astigmatic aberration coefficients for the single achromat were found to be 154 $m\lambda$, 3 $m\lambda$, and 79 $m\lambda$ with an uncertainty of 3 $m\lambda$ for the ROIs at the left, middle and right of the FOV, respectively, whereas we measured corresponding values of 36 $m\lambda$, 7 $m\lambda$, and 61 $m\lambda$ with an uncertainty of 2 $m\lambda$ for the double back-to-back achromat design, which amounts to an average reduction in astigmatism for the double back-to-back achromat design with a factor 2.0.

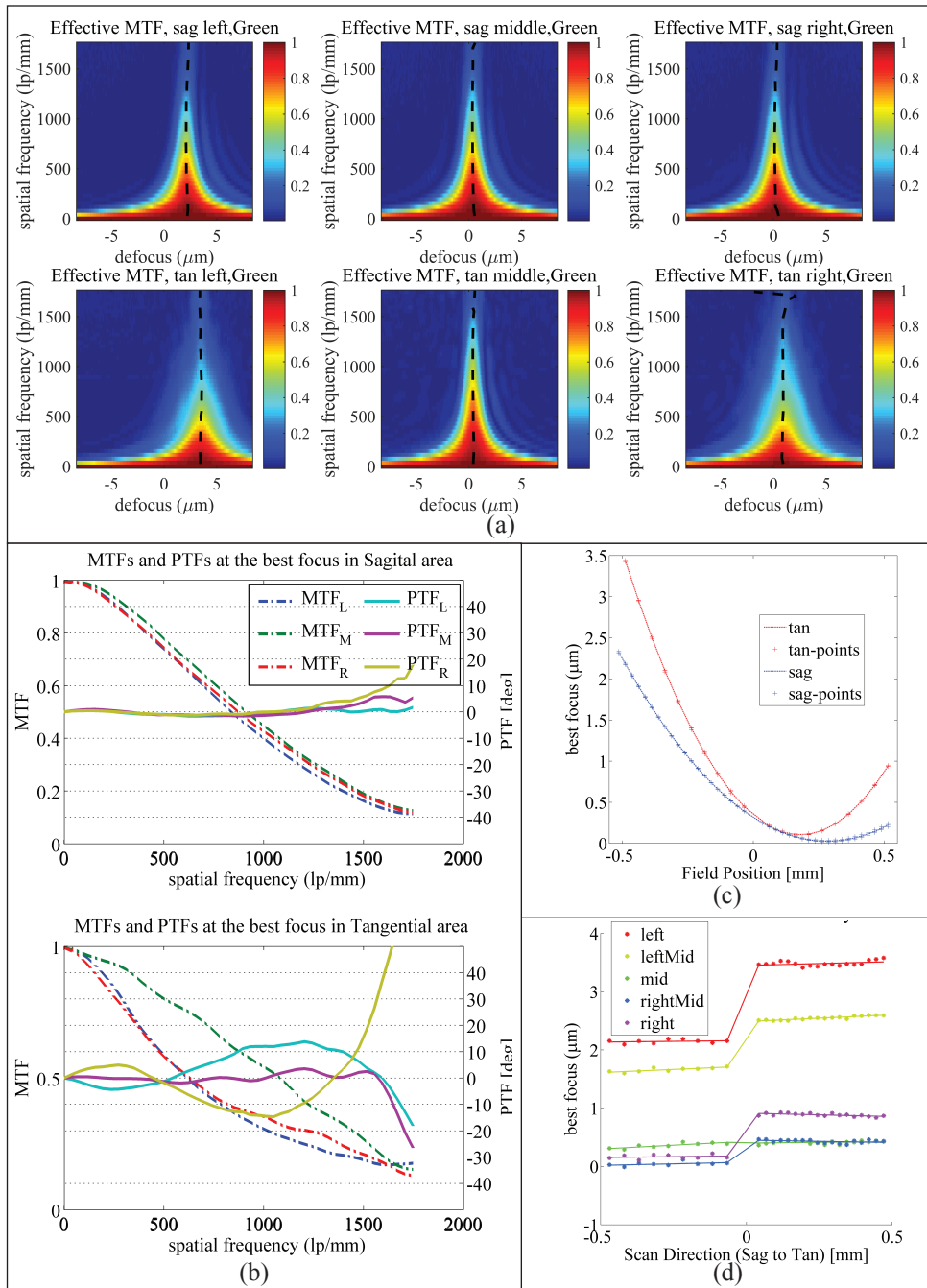


Figure 2.6: Results for a Nikon 20x/0.75 objective lens with single achromat tube lens (case A) (a) Through-focus MTFs for 6 ROIs (red rectangles in custom resolution target) with the best focus line (dashed black line). (b) MTFs (dashed) and PTFs (solid) at the overall best focus. (c) Measured field curvatures. (d) Best focus lines in the scan direction at five positions in the FOV from the sagittal to the tangential area showing the absence of tilt in the scan direction and sagittal to tangential jumps due to astigmatism.

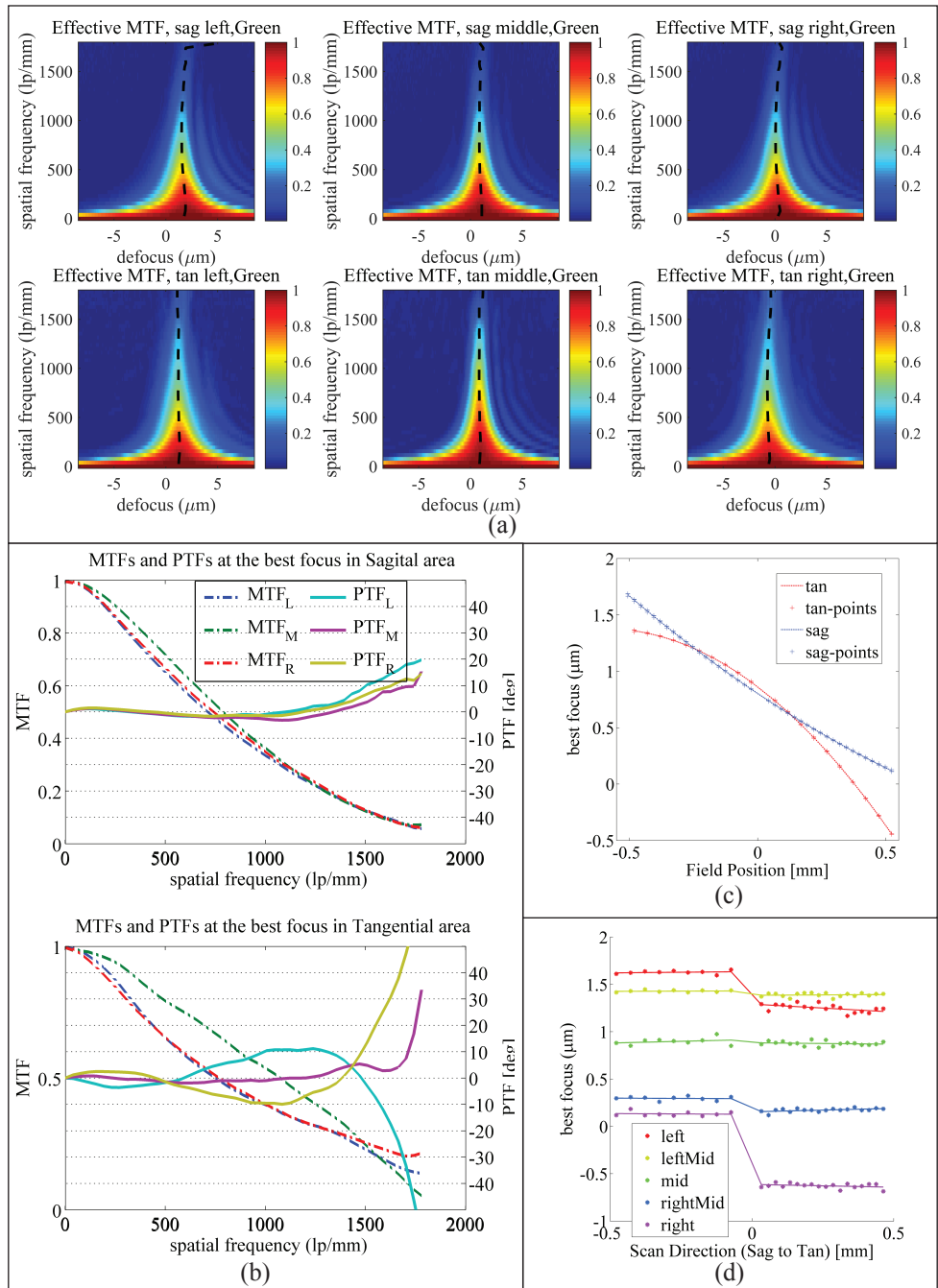


Figure 2.7: Results for a Nikon 20 \times /0.75 objective lens with double back-to-back achromat tube lens (case B) (a) Through-focus MTFs for 6 ROIs (red rectangles in custom resolution target) with the best focus line (dashed black line). (b) MTFs (dashed) and PTFs (solid) at the overall best focus. (c) Measured field curvatures. (d) Best focus lines in the scan direction at five position in the FOV from the sagittal to the tangential area showing the absence of the scan direction and sagittal to tangential jumps due to astigmatism.

2.3.2. STATISTICAL ERRORS

The statistical error of the measured aberrations is found by error propagation from the standard deviation of the MTF and PTF within the ROIs, as described in section 2. Fig. 2.8 shows typical examples of the error in MTF measurement (around 1%) and PTF (ranging from below 1 deg for small spatial frequencies to above 10 deg for high spatial frequencies). The best focus as a function of spatial frequency can subsequently be determined with an error of around 100 nm, the overall best focus with an error of around 10 nm. This translates into statistical errors in the measured aberration coefficients ranging typically from 5 to 20 $m\lambda$.

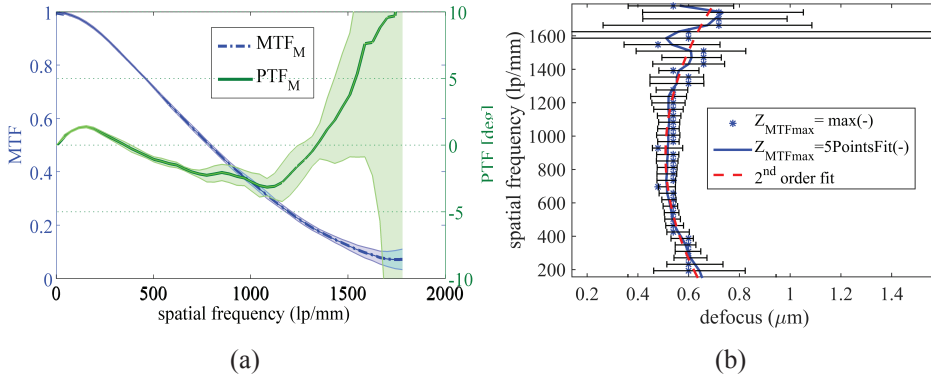


Figure 2.8: Example of statistical errors for case B in the middle sagittal ROI (a) Average MTF and PTF at the best focus, (b) Measured and fitted best focus as a function of spatial frequency. The small decrease of the error at the highest spatial frequency is due to a coincidence, not all the ROIs show this behavior.

2.3.3. EFFECT OF AN AGING OBJECTIVE LENS

Objective lenses, as any piece of hardware, suffer from aging. This manifests itself in misalignment of the individual lenses within the mounted objective lens, giving rise to increased levels of aberrations. In order to test the aging effect, we measured the aberrations of an 8-year old Olympus 20 \times /NA0.75 objective lens with undocumented use in these 8 years, in combination with a single achromat tube lens (case C, Fig. 2.9).

We observed higher levels of all aberrations. The spherical aberration increased to $102 \pm 10 m\lambda$. We measured coma values of $62 \pm 14 m\lambda$, $46 \pm 15 m\lambda$, $30 \pm 14 m\lambda$ in the sagittal area from left to right, and corresponding values of $-130 \pm 14 m\lambda$, $-80 \pm 11 m\lambda$, $-30 \pm 7 m\lambda$ in the tangential area. The measured levels of astigmatism were $295 \pm 8 m\lambda$, $-17 \pm 8 m\lambda$, and $296 \pm 8 m\lambda$ for the ROIs at the left, middle and right of the FOV. This is significantly higher than the result for case A, but this could also be due to design choices of the manufacturer for balancing the lowest order aberrations between the objective and the custom tube lens in their microscope systems. The field curvature and astigmatism are $0.48 \mu\text{m}$ and $2.5 \mu\text{m}$, respectively. Also in this case we have observed a significant asymmetry in the tangential and sagittal best focus lines, arising from tilt of the optical axes w.r.t. the mechanical reference.

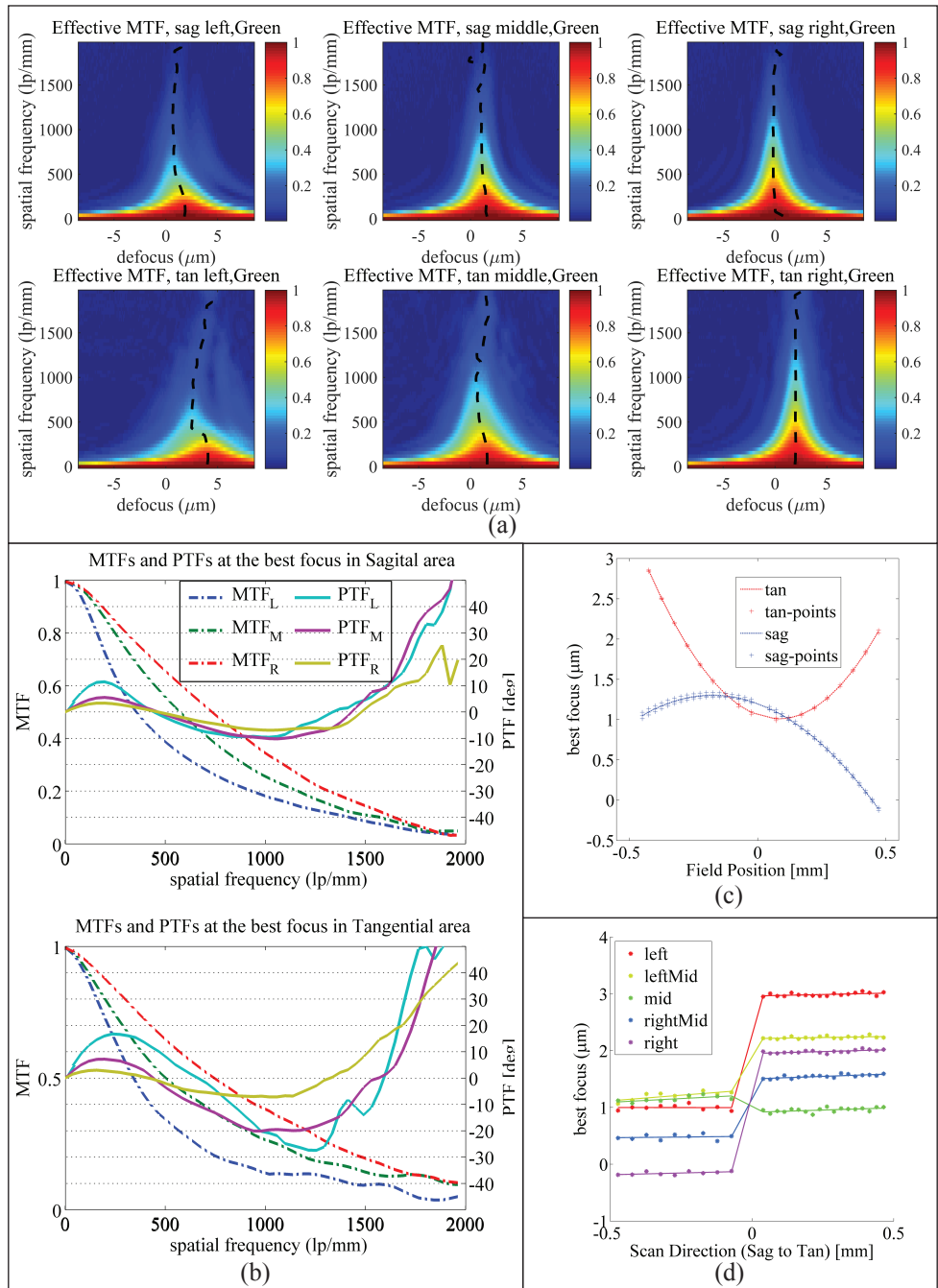


Figure 2.9: Results for an aged Olympus 20 \times /0.75 objective lens with single achromat tube lens (case C) (a) Through-focus MTFs for 6 ROIs (red rectangles in custom resolution target) with the best focus line (dashed black line). (b) MTFs (dashed) and PTFs (solid) at the overall best focus. (c) Measured field curvatures. (d) Best focus lines in the scan direction at five position in the FOV from the sagittal to the tangential area showing the absence of the scan direction and sagittal to tangential jumps due to astigmatism.

2.3.4. VALIDATION WITH SHACK-HARTMANN WAVEFRONT SENSOR

A summary of the aberrations measured from the through-focus OTF is shown in Fig. 2.10(a). The results of the validation measurement with the SH-setup are shown in Fig. 2.10(b). The two independent sets of measurements agree with typical errors ranging from $10\text{ m}\lambda$ to $40\text{ m}\lambda$, which is reasonable in view of the alignment uncertainty in the different mechanical and optical components and the statistical error in measuring the aberrations from the through-focus OTF. The agreement is less good for spherical aberration, which we attribute to the sensitivity to the definition of the pupil radius in the SH measurement, which gives rise to a bit overestimated aberration coefficient compared to the through-focus OTF based measurement. The pupil radius in the SH measurement can be set with an accuracy of about 0.5 mm . We extracted the spherical aberration for different pupil radius settings and found variations of about $30\text{ m}\lambda$ for 0.5 mm difference of the pupil radius. Our proposal to quantify the spherical aberration from the curvature of the best focus line is therefore not validated with high accuracy.

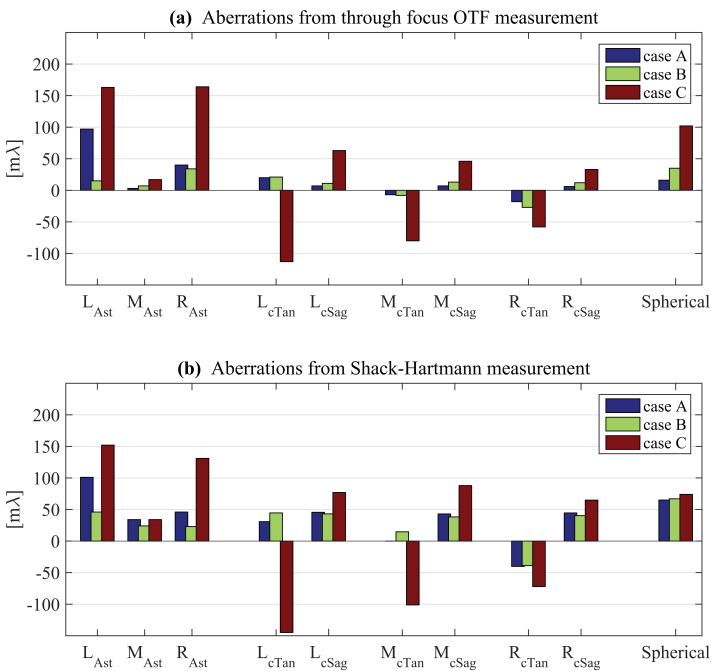


Figure 2.10: Comparison of the aberration values for astigmatism, coma and spherical aberration using standard Zernike coefficients representation [24] for case A (Nikon $20\times/0.75$ objective lens with single achromat tube lens), case B (Nikon $20\times/0.75$ objective lens with double back-to-back achromat tube lens), and case C (aged Olympus $20\times/0.75$ objective lens with single achromat tube lens). L, M and R stands for left, middle and right of the FOV, and Ast, cTan and cSag denote astigmatism, tangential coma and sagittal coma respectively. (a) Results obtained with the proposed method. (b) Results obtained with the Shack-Hartmann measurement. It should be noted that the left and right of the FOV are here at $\pm 0.38\text{ mm}$ in the FOV due to the mechanical constraints in the Shack-Hartmann setup. To make a fair comparison to the aberration values of (b) the values reported in (a) are also at $\pm 0.38\text{ mm}$ in the FOV and can therefore not be compared directly to the values in section 3.1 to 3.3 which were acquired at $\pm 0.5\text{ mm}$ field position.

In all three cases we observed an apparent tilt in the best focus curves, although there was no slide tilt w.r.t. the mechanical reference axis of the objective lens. This points to possible misalignments in the system, which may be linked to intricate patterns in the magnitude and orientation of astigmatism and coma across the FOV of the objective lens [28–30]. In order to test this link we have measured the aberrations across the FOV (see Fig. 2.11), which indeed shows complicated dependencies of magnitude and orientation of both astigmatism and coma on the field position. One typical example is shown in Fig. 2.11(c), where the astigmatic aberration field complies with so-called “binodal astigmatism”, i.e. the astigmatism is zero for two, diametrically opposite, points in the FOV. As a consequence, the tangential and sagittal best focus curves will not touch at the center of the FOV, but rather cross at two nonzero field positions, in agreement with what is seen in Fig. 2.9(c). It also implies there is a small ($34m\lambda$) on-axis astigmatism, which we attribute to relative misalignment of objective lens and tube lens.

Another interesting observation is related to the direction of coma in the FOV. According to Fig. 2.11(a) and Fig. 2.11(b), the direction of the coma component in the scan direction (sagittal coma) does not change. In contrast, the coma component in the field direction (tangential coma) is flipped from left to right. This behavior can be clearly observed in Fig. 2.6(b) and Fig. 2.7(b) in which all the sagittal PTF curves have the same shape, but the left tangential PTF curve has the opposite shape of the right tangential PTF curve

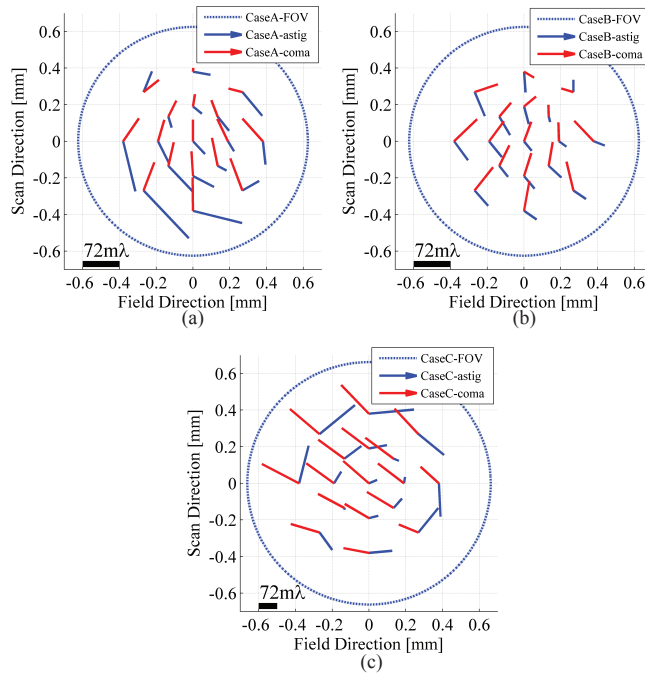


Figure 2.11: Representation of coma and astigmatism measured by the Shack-Hartmann sensor over the FOV for three cases: (a) single achromat tube lens, (b) double achromat tube lens design, and (c) aged objective lens with single achromat tube lens. Note the different scale bar in (c) compared to (a) and (b).

2.3.5. CHROMATIC ABERRATION

Through-focus OTFs and aberrations have also been measured for red and blue light. Fig. 2.12 shows the measured sagittal and tangential best focus lines for the three color channels for the single achromat tube lens (case A) and the double back-to-back tube lens design (case B). They are in good agreement with the Zemax simulation result (Fig. 2.5). For case B, however, there is a change in sign in tangential curvature for the blue channel compared to the Zemax results. We also observed a significant increase in coma in the blue channel compared to the green and red channel.

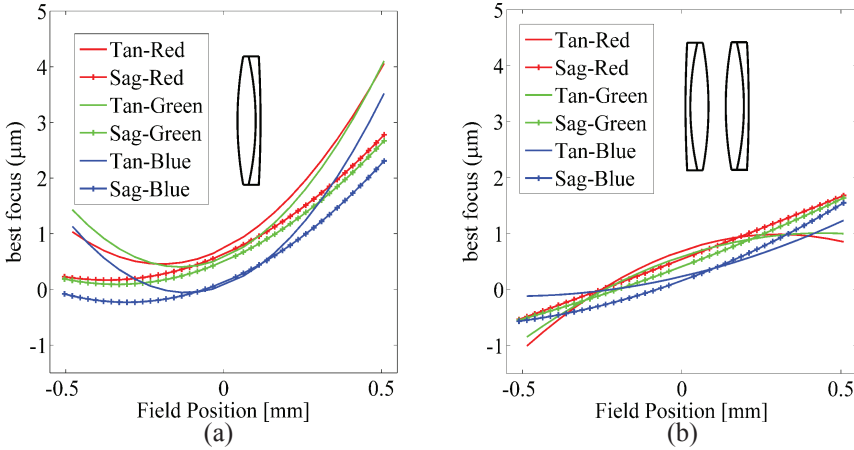


Figure 2.12: Sagittal and tangential best focus lines for the three color channels (red: 618 nm, green: 565 nm, blue: 435 nm) for the (a) single achromat tube lens (case A). (b) double back-to-back achromat tube lens design (case B).

2.4. DISCUSSION

In summary, we have presented a systematic method to assess the optical quality of a WSI system using measurement and analysis of the through-focus OTF for different positions in the FOV. The analysis of MTF and PTF enables the determination of spherical aberration, coma, astigmatism, and field curvature. The method has been benchmarked to SH-wavefront sensing results, and has been shown to be in good agreement with those. Our analysis tool will facilitate the reliable testing and monitoring of the optical quality of WSI systems, using only the custom resolution target and image analysis software, without the need for additional optical or mechanical hardware.

The non-invasiveness of the technique provides the key advantage compared to more conventional aberration measurement methods such as SH-wavefront sensing. The advantage compared to iterative aberration retrieval from through-focus MTF data is the simplicity and directness of the approach. In order to make a fairer comparison we have constructed an algorithm for doing iterative aberration retrieval based on a linear least squares fit of the measured OTF's by the incoherent scalar diffraction OTF, where the lowest order aberrations defocus, astigmatism, coma and spherical aberration are the fit

parameters. The algorithm was implemented with MATLAB's `fminsearch` routine. We found that the iterative aberration retrieval algorithm has indeed problems with convergence, especially for aberration levels that exceed the diffraction limit. A drawback of the proposed method is that no distinction is made between lower and higher order aberrations of a certain type. For example, when the system is affected by sizeable amounts of higher order coma (A_{51}) in addition to lowest order coma (A_{31}) the method will give an effective value for the coma coefficient, not necessarily equal to the underlying Zernike values.

We would like to stress that the proposed method assesses the overall image quality of our home-built WSI system, including our tube lens configurations. The results obtained for systems with different objective lenses may therefore not be interpreted as characterizations or comparisons of these objective lenses alone.

The extension of the proposed optical quality assessment to widefield non-scanning imaging systems requires changes with respect to our implementation. First of all, averaging over the edge response in a certain direction is prohibited, as the translational invariance of the line scanning system is lost. Second, a different design of resolution target may be better suited to the optical architecture of the widefield system. We envision that an array of square blocks would provide the same set of mutually orthogonal edges (the top and bottom edges vs. the left and right edges of the square) for the different regions in the FOV of the objective lens.

We foresee two lines of research as follow-up of the currently reported research. In this work we have implicitly assumed that we deal with an incoherent imaging system, whereas in reality bright field microscopy systems are partially coherent. Approximating partially coherent imaging systems as being fully incoherent is reasonable for a condenser NA about equal to or higher than the objective lens NA, so that in fact the current treatment is sound. However, investigating the effects of partial coherence by tuning the condenser NA seems a fruitful direction for follow-up experiments. A second line of investigation is related to the analysis of full-field aberration maps as shown in Fig. 2.11 using the methods of [28–32]. This may help to quantify possible misalignments, and thereby may lead to a new way of finding the root causes of different aberrations that may be present or to novel methods of calibrating the alignment of different optical and mechanical components in the system.

REFERENCES

- [1] S. M. Shakeri, B. Hulsken, L. J. van Vliet, and S. Stallinga, *Optical quality assessment of whole slide imaging systems for digital pathology*, *Opt. Express* **23**, 1319–1336 (2015).
- [2] R. S. Weinstein, et al., *Telepathology overview: from concept to implementation*, *Human Pathology* **32**, 1283–99 (2001).
- [3] J. Gu and R. W. Ogilvie, *Virtual microscopy and virtual slides in teaching, diagnosis, and research* (Taylor & Francis, 2005).
- [4] J. R. Gilbertson, et al., *Primary histologic diagnosis using automated whole slide imaging: a validation study*, *BMC Clinical Pathology* **6** (2006).

- [5] S. Al-Janabi, et al., *Digital pathology: current status and future perspectives*, *Histopathology* **61**, 1–9 (2012).
- [6] J. Ho, et al., *Use of whole slide imaging in surgical pathology quality assurance: design and pilot validation studies*, *Human Pathology* **37**, 322–31 (2006).
- [7] A. H. Beck, et al., *Systematic analysis of breast cancer morphology uncovers stromal features associated with survival*, *Science Trans. Med.* **3** (2011).
- [8] S. Doyle, M. Feldman, J. Tomaszewski, and A. Madabhushi, *A boosted bayesian multiresolution classifier for prostate cancer detection from digitized needle biopsies*, *IEEE Transactions on Bio-medical Engineering* **59**, 1205–18 (2012).
- [9] M. N. Gurcan, et al., *Histopathological image analysis: a review*, *IEEE Review Biomedical Engineering* **2**, 147–71 (2009).
- [10] J. P. Vink, M. B. Van Leeuwen, C. H. Van Deurzen, and G. De Haan, *Efficient nucleus detector in histopathology images*, *Jornal of Microscopy* **249**, 124–35 (2013).
- [11] M. G. Rojo, G. B. Garcia, C. P. Mateos, J. G. Garcia, and M. C. Vicente, *Critical comparison of 31 commercially available digital slide systems in pathology*, *International Journal of Surgical Pathology* **14**, 285–305 (2006).
- [12] R. S. Weinstein, et al., *An array microscope for ultrarapid virtual slide processing and telepathology. design, fabrication, and validation study*, *Human Pathology* **35**, 1303–14 (2004).
- [13] H. Netten, L. J. Van Vliet, F. R. Boddeke, P. De Jong, and I. T. Young, *A fast scanner for fluorescence microscopy using a 2D CCD and time delayed integration*, *BioImaging* **2** (1994).
- [14] G. D. Boerman, *Modulation transfer function in optical and electro-optical systems* (SPIE, 2001).
- [15] T. Williams, *The optical transfer function of imaging systems* (CRC, 1998).
- [16] J. R. Fienup, *Phase-retrieval algorithms for a complicated optical system*, *Appl. Opt.* **32**, 1737–1746 (1993).
- [17] J. R. Fienup, *Phase retrieval algorithms: a comparison*, *Appl. Opt.* **21**, 2758–2769 (1982).
- [18] V. R. Bhakta, M. Somayaji, and M. P. Christensen, *Image-based measurement of phase transfer function*, *Imaging and Applied Optics Congress* (2010).
- [19] V. R. Bhakta, M. Somayaji, and M. P. Christensen, *Effects of sampling on the phase transfer function of incoherent imaging systems*, *Opt. Express* **19**, 24609–24626 (2011).
- [20] J. C. Mullikin, et al., *Methods for CCD camera characterization*, *Proc. SPIE* **2173**, 73–84 (1994).

- [21] *Photography–Electronic Still Picture Cameras–Resolution Measurements*, ISO Standard 12233 (2000).
- [22] K. He, J. Sun, and X. Tang, *Guided image filtering*, *IEEE Transaction on Pattern Analysis and Machine Intelligence*, IEEE Transactions on Pattern Analysis and Machine Intelligence **35**, 1397–1409 (2013).
- [23] I. A. Cunningham and A. Fenster, *A method for modulation transfer function determination from edge profiles with correction for finite-element differentiation*, *Medical Physics* **14**, 533–7 (1987).
- [24] M. Born and E. Wolf, *Principles of Optics* (Cambridge University, 1999).
- [25] C. J. R. Sheppard, *Depth of field in optical microscopy*, *Journal of Microscopy* **149**, 73–75 (1988).
- [26] S. Stallinga, *Compact description of substrate related aberrations in high numerical-aperture optical disc read-out*, *Appl. Opt.* **44**, 849–858 (2005).
- [27] S. Stallinga, *Finite conjugate spherical aberration compensation in high numerical-aperture optical disc read-out: erratum*, *Appl. Opt.* **45**, 2279–2279 (2006).
- [28] R. V. Shack and K. Thompson, *Influence of alignment errors of a telescope system on its aberration field*, *Proc. SPIE*, 24th Annual Technical Symposium **0251**, 146–153 (1980).
- [29] R. Tessieres, *Optical Sciences*, Master's thesis, University of Arizona, Tucson (2003).
- [30] K. Thompson, *Description of the third-order optical aberrations of near-circular pupil optical systems without symmetry*, *J. Opt. Soc. Am. A* **22**, 1389–1401 (2005).
- [31] P. L. Schechter and R. S. Levinson, *Generic misalignment aberration patterns in wide-field telescopes*, *Publications of the Astronomical Society of the Pacific* **123**, 812–832 (2011).
- [32] K. P. Thompson, T. Schmid, O. Cakmakci, and J. P. Rolland, *Real-ray-based method for locating individual surface aberration field centers in imaging optical systems without rotational symmetry*, *J. Opt. Soc. Am. A* **26**, 1503–1517 (2009).

APPENDIX

The aberration function including astigmatism and defocus along the pupil line is:

$$\begin{aligned}
 W(x, 0) &= \sqrt{6} A_{22} f_1(x) + z_{ob} f_2(x), \\
 f_1(x) &= x^2 \\
 f_2(x) &= 1 - \sqrt{1 - NA^2 x^2}
 \end{aligned} \tag{2.4}$$

The RMS value of the aberration function along the pupil line is:

$$W_{RMS}^2 = \langle W^2 \rangle - \langle W \rangle^2 \tag{2.5}$$

where the angular brackets indicate averaging over all values of x . This results in:

$$W_{RMS}^2 = 6 \left(\langle f_1^2 \rangle - \langle f_1 \rangle^2 \right) A_{22}^2 + 2 \sqrt{6} \left(\langle f_1 f_2 \rangle - \langle f_1 \rangle \langle f_2 \rangle \right) A_{22} z_{ob} + \left(\langle f_2^2 \rangle - \langle f_2 \rangle^2 \right) z_{ob}^2 \quad (2.6)$$

which is minimized for

$$z_{ob} = - \frac{\langle f_1 f_2 \rangle - \langle f_1 \rangle \langle f_2 \rangle}{\langle f_2^2 \rangle - \langle f_2 \rangle^2} \sqrt{6} A_{22} \quad (2.7)$$

The same procedure can be used for determining the position of the orthogonal focal line, leading to the sought-for proportionality factor:

$$S(NA) = \frac{\langle f_2^2 \rangle - \langle f_2 \rangle^2}{2 \sqrt{6} \left(\langle f_1 f_2 \rangle - \langle f_1 \rangle \langle f_2 \rangle \right)} \quad (2.8)$$

The different averages have been analytically evaluated using Mathematica to:

$$\begin{aligned} \langle f_1 \rangle &= \frac{1}{3} \\ \langle f_2 \rangle &= 1 - \frac{NA \sqrt{1 - NA^2} + \text{ArcSin}[NA]}{2NA} \\ \langle f_1^2 \rangle &= \frac{1}{5} \\ \langle f_1 f_2 \rangle &= \frac{1}{3} - \frac{NA \sqrt{1 - NA^2} (-1 + 2NA^2) + \text{ArcSin}[NA]}{8NA^3} \\ \langle f_2^2 \rangle &= 2 - \frac{NA^2}{3} - \sqrt{1 - NA^2} - \frac{\text{ArcSin}[NA]}{NA} \end{aligned} \quad (2.9)$$

3

SHACK-HARTMANN SENSOR BASED OPTICAL QUALITY TESTING OF WHOLE SLIDE IMAGING SYSTEMS

Whole Slide Imaging (WSI) systems are used in the emerging field of digital pathology for capturing high-resolution images of tissue slides at high throughput. We present a technique to measure the optical aberrations of WSI systems using a Shack-Hartmann wavefront sensor as a function of field position. The resulting full-field aberration maps for the lowest order astigmatism and coma are analyzed using nodal aberration theory. According to this theory two coefficients describe the astigmatism and coma inherent to the optical design and another six coefficients are needed to describe the cumulative effects of all possible misalignments on astigmatism and coma. The nodal aberration theory appears to fit well to the experimental data. We have measured and analyzed the full-field aberration maps for two different objective lens-tube lens assemblies and found that only the optical design related astigmatism coefficient differed substantially between the two cases, but in agreement with expectations. We have also studied full-field aberration maps for intentional decenter and tilt and found that these affect the misalignment coefficient for constant coma (decenter) and the misalignment coefficient for linear astigmatism (tilt), while keeping all other nodal aberration theory coefficients constant.

3.1. INTRODUCTION

DIGITAL pathology is based on the use of digital images of tissues for diagnosis of disease. These images are typically $\sim 15\text{mm}^2$ in size and are sampled at a sampling density of $\sim 0.25\mu\text{m}/\text{pixel}$ with a Whole Slide Imaging (WSI) system. This “pushbroom” scanner sweeps the slide lane by lane ($\sim 1\text{mm}$ wide) and stitches the lanes into the final high-resolution image (Figure 3.1a). It is important in assembly and maintenance to test and monitor the optical quality of WSI systems. This can be done by analyzing through-focus images of custom test targets for measuring the Optical Transfer Function (OTF) and subsequently extracting the different primary aberration coefficients [2]. This noninvasive testing method provides a systematic approach to quantify the optical quality solely by using a custom-built resolution target and a software tool. However, this OTF-based method needs validation using direct aberration measurements. A well-known method is to extract aberrations from wavefront measurements using a Shack-Hartmann sensor [3]. The aberrations that are so revealed are due to imperfections in the individual components and also due to possible alignment errors in the system. The wavefront measurements with the Shack-Hartmann sensor can be done for different positions in the Field Of View (FOV) of the objective lens. The measurement of this full-field aberration map can be used to reveal the root cause of the aberrations. This could subsequently be used to modify the alignment of the optical system in such a way as to minimize the overall level of aberrations or for testing the quality of individual optical components (objective lens, tube lens). Several studies have been carried out to develop a theory of misalignment effects on the full-field aberration maps, mostly for aligning telescopes for astronomy applications [4–7]. Here, we present details of a technique to adapt the Shack-Hartmann test for measuring the full-field aberration map of a WSI system, and we present an analysis of the full-field aberration maps for revealing different misalignment root causes such as decenter and tilt of optical components. The outline of this paper is as follows. In section 2, we describe the Shack-Hartmann measurement setup and the theory of full-field aberration map analysis for coma and astigmatism. Then we present the comparison of these full-field aberration maps to the OTF-based aberration test for two different objective lens-tube lens assemblies in section 3. We also apply the full-field aberration map analysis to a configuration with intentional decenter and tilt misalignment. Finally, the paper is concluded with a brief summary in section 4.

3.2. METHODS

We built a wavefront sensing setup using an Optocraft SHR-150-CL Shack-Hartmann sensor (12 bit, detection area $11.8\times 8.9\text{mm}^2$, 78×59 microlens array) to measure the aberrations of the optical system under inspection (Figure 3.1b). A pinhole ($5\mu\text{m}$ diameter) mounted in between a glass slide and a coverslip is used as a point source object. In order to provide a (near) parallel wavefront to the SH sensor, an additional collimating lens (Melles Griot 01LAO536 - 120mm focal length) is placed at its focal distance from the system’s image plane. We measured the aberrations of this collimating lens separately to account for this effect in the final results. The aberrations for different positions in the FOV of the objective lens can be probed by laterally translating the pinhole slide.

The alignment procedure is depicted step by step in Figure 3.2. The alignment of the

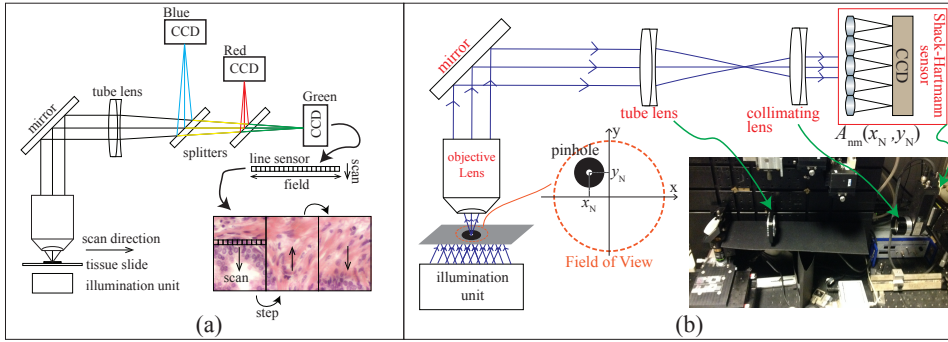


Figure 3.1: Schematic layout of the (a) home-built line sensor based WSI system, (b) Shack-Hartmann test setup. The pinhole can be moved in the field of view and then the corresponding aberration coefficients $A_{nm}(x_N, y_N)$ are measured by the Shack-Hartmann sensor.

objective lens, folding mirror and tube lens are based on the alignment of two mutually perpendicular reference laser lines. These reference laser lines are aligned with respect to a mechanical reference, namely the mounting plate with an array of grooves for mounting the different optical components. Any residual deviations from perpendicularity arise from the mechanical adjustment error of the irises used to align the reference laser lines. The measurement of the aberrations is started by placing the pinhole at the center of the FOV (following step VI in Figure 3.2). The Shack-Hartmann sensor is translated to be perpendicular to the incident wavefront after moving the pinhole to each new position in the FOV, so that the measured coefficients for tilt and defocus become as small as possible. The measurements of the aberrations were restricted to positions up to about 80% of the full FOV diameter in view of mechanical constraints of the objective lens mount and Shack-Hartmann sensor mount.

3.2.1. SHACK-HARTMANN TEST SETUP

3.2.2. FULL-FIELD ABERRATION MAP ANALYSIS

Thompson in [8–10] developed a new way of analyzing aberrations in an optical system by looking into the field dependency of each individual aberration. He showed that for well-aligned rotationally symmetrical optical systems, the full-field aberration map is rotationally symmetric as well. Any misalignment breaks the symmetry of the map. For each aberration type the symmetry is broken in a specific way, giving rise to a limited set of nodes (points in the FOV with zero aberration of the considered type) in the full-field aberration map. The map will have one node at the center of the FOV if the optical system is well aligned. The maximum number of nodes for each type of aberration is equal to the power of the field dependency for that aberration, i.e. if the aberration scales as $\sim \eta^p$, with η a field coordinate, then there will be at most p nodes in the full-field aberration map. For example, for lowest order astigmatism we have $p = 2$, implying that any misalignment can create at maximum two nodes in the full-field aberration map. This nodal aberration theory has been used by Tessieres and Manuel in unpublished manuscripts [6, 11] to relate the full-field Zernike coefficient map to the presence of pos-

sible misalignment in reflective optical systems such as telescopes. We use this theory to study misalignment effects on (lowest order order) coma and astigmatism, as these are critical to the optical quality of WSI systems [2].

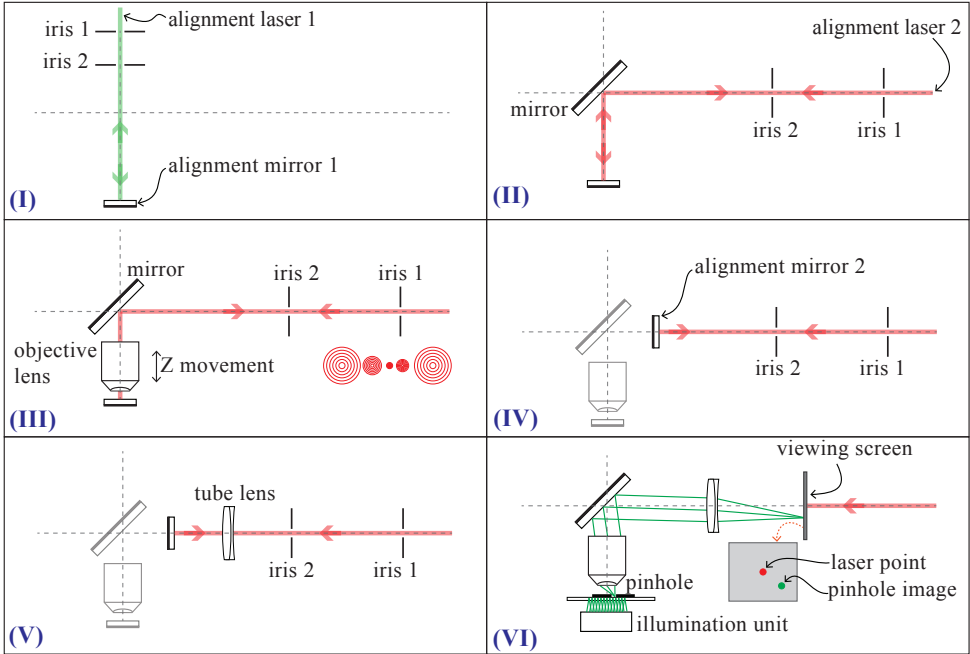


Figure 3.2: Alignment procedure. Step (I) is to align mirror 1 perpendicular to laser 1 reference line. The mirror is placed such that both laser light and its reflection pass through the irises. Step (II) is to place the folding mirror at 45 deg with respect to laser 2 reference line. Step (III) is to align the objective lens. To do so, the objective lens will be moved along the z-axis. If the optical axis of the objective lens is aligned with the reference laser line then the through-focus spots are concentric. The size of the irises needs to be readjusted in order to see the fringes at different distances. Step (IV) is to place another alignment mirror perpendicular to the laser 2 reference line in order to align the tube lens. In step (V), the tube lens is positioned such that the reflected laser light passes through the two irises and there is no double reflection pattern on the left side of the iris. Now, the three optical components are aligned. Step (VI) is to place the pinhole at the optical axis. At this step the alignment mirrors are removed and the illumination unit is placed below the objective lens. A semi-transparent viewing screen (e.g. thin paper) is used to visually monitor the position of the pinhole image and laser reference line. The pinhole slide is translated until its image coincides with the laser point at the viewing screen.

The aberration function of the optical system can be expanded in Zernike polynomials of radial order n and azimuthal order m , where the coefficients are functions of the field coordinates x and y [6, 11]:

$$W = \sum_{n,m} A_{nm}(x, y) Z_{nm}(\rho, \varphi), \quad (3.1)$$

where ρ and φ are the radial and azimuthal coordinates of the (circular and normalized) exit pupil. From now on we will focus on (lowest order) coma and astigmatism only. In an aligned centrosymmetric optical system these have, to the lowest order, a linear and

quadratic dependency on the field coordinates, respectively:

$$\begin{aligned} W_{astigmatism} &= A_{22}(x, y)Z_{22} + A_{2-2}(x, y)Z_{2-2} \\ &= (a_{quadratic}(x^2 - y^2))Z_{22} + (2a_{quadratic}xy)Z_{2-2}, \\ W_{coma} &= A_{31}(x, y)Z_{31} + A_{3-1}(x, y)Z_{3-1} \\ &= (c_{linear}x)Z_{31} + (c_{linear}y)Z_{3-1}, \end{aligned} \quad (3.2)$$

where $a_{quadratic}$ and c_{linear} are constants inherent to the optical design of the system for astigmatism and coma respectively. For example, c_{linear} is a measure for the Offense against the Sine Condition (OSC). If the optical system is misaligned, i.e. if the rotational symmetry around the optical axis is broken, then the field dependency of the Zernike aberration coefficients A_{nm} changes as follows [11]:

$$\begin{aligned} A_{22}(x, y) &= a_{quadratic}(x^2 - y^2) - a_{yLinear}y + a_{xLinear}x + a_{hConstant}, \\ A_{2-2}(x, y) &= 2a_{quadratic}xy + a_{yLinear}x + a_{xLinear}y + a_{dConstant}, \\ A_{31}(x, y) &= c_{linear}x + c_{xConstant}, \\ A_{3-1}(x, y) &= c_{linear}y + c_{yConstant}, \end{aligned} \quad (3.3)$$

where the misalignments introduce constant coma, constant astigmatism and linear astigmatism. The coefficients of all contributions to the full-field aberration map can be found using a least-squares fit. This can be done by solving the following set of equations for a and c by measuring A_{nm} at N points in field of view:

$$\begin{pmatrix} A_{31}^1 \\ A_{3-1}^1 \\ \vdots \\ A_{31}^N \\ A_{3-1}^N \end{pmatrix} = \begin{pmatrix} x_1 & 0 & 1 \\ y_1 & 1 & 0 \\ \vdots & \vdots & \vdots \\ x_N & 0 & 1 \\ y_N & 1 & 0 \end{pmatrix} \begin{pmatrix} c_{linear} \\ c_{yConstant} \\ c_{xConstant} \end{pmatrix} \quad (3.4)$$

$$\begin{pmatrix} A_{22}^1 \\ A_{2-2}^1 \\ \vdots \\ A_{22}^N \\ A_{2-2}^N \end{pmatrix} = \begin{pmatrix} (x_1)^2 - (y_1)^2 & -y_1 & x_1 & 0 & 1 \\ 2x_1y_1 & x_1 & y_1 & 1 & 0 \\ \vdots & \vdots & \vdots & \vdots & \vdots \\ (x_N)^2 - (y_N)^2 & -y_N & x_N & 0 & 1 \\ 2x_Ny_N & x_N & y_N & 1 & 0 \end{pmatrix} \begin{pmatrix} a_{quadratic} \\ a_{yLinear} \\ a_{xLinear} \\ a_{dConstant} \\ a_{hConstant} \end{pmatrix} \quad (3.5)$$

In summary, the full-field aberration maps for astigmatism and coma can thus be characterized by two numbers, characterizing the optical design ($a_{quadratic}$ and c_{linear}), and by six numbers characterizing misalignment effects ($a_{hConstant}$, $a_{dConstant}$, $a_{xLinear}$, $a_{yLinear}$, $c_{xConstant}$, and $c_{yConstant}$).

3.3. RESULTS

3.3.1. OTF-BASED VS. SHACK-HARTMANN ABERRATION MEASUREMENT

In this section, we present results on the through-focus OTF-based aberration measurement, which was recently proposed by us [2] for two objective lens-tube lens assemblies. We use an 8-year old Olympus 20×/0.75 objective lens, which we know has become significantly aberrated in the course of time, and two simple tube lens designs: a

single achromat (Thorlabs AC508-250-A-ML, 250 mm focal length) and double back-to-back achromat design (two Thorlabs AC508-500-A, 500 mm focal length). The method is based on measurement of the through-focus Modulation Transfer Function (MTF) and Phase Transfer Function (PTF) obtained from the edge response of a custom-made resolution target, composed of sagittal and tangential edges. This enables quantitative analysis of a number of primary aberrations. The curvature of the best focus as a function of spatial frequency is indicative for spherical aberration, the argument of the OTF quantifies coma, and the best focus as a function of field position for sagittal and tangential edges allows assessment of astigmatism and field curvature. Aberrations are reported here as standard Zernike values, i.e. equal to the Root Mean Square (RMS) value in magnitude, but with the sign of the Zernike fringe coefficient. Figure 3.3 and 3.4 show the re-

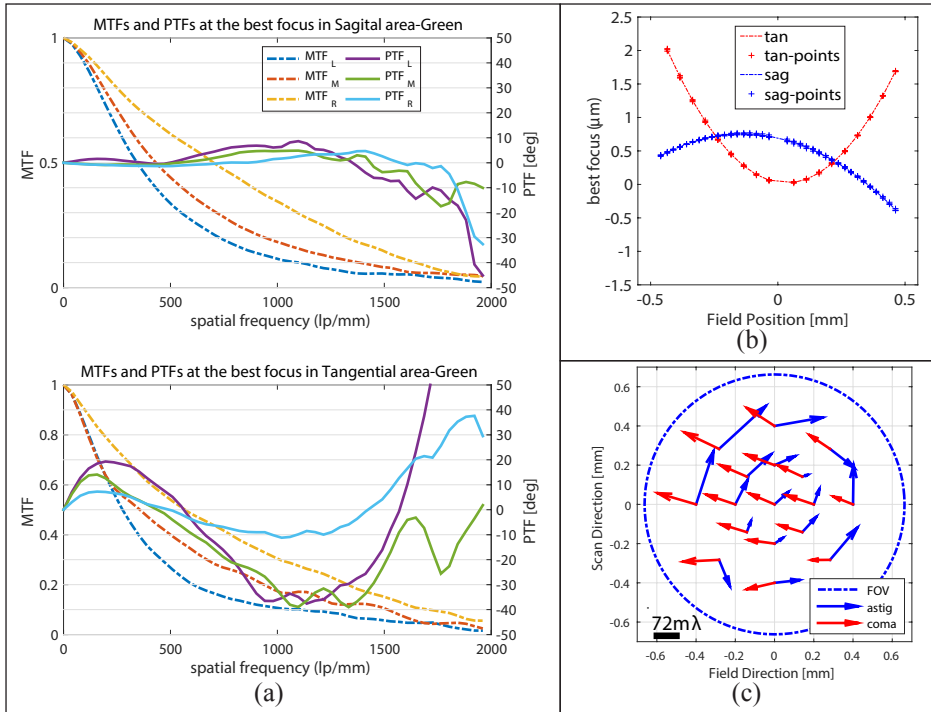


Figure 3.3: Results for the Olympus 20 \times /0.75 objective lens with single achromat tube lens. (a) MTFs (dashed) and PTFs (solid) at the overall best focus along field direction. Subscripts L, M, R denote the left, middle and right side of the FOV and correspond to positions -0.4, 0 and 0.4 mm in the field direction. (b) Measured field curvatures. (c) Full-field aberration map measured by Shack-Hartmann sensor.

sults of the measurements with a wavelength around 565 nm. The measured quadratic astigmatism coefficient with the OTF based method are $\text{aquadratic} = -1.44 \lambda/mm^2$ for the single achromat case and $\text{aquadratic} = -0.55 \lambda/mm^2$ for the double back-to-back achromat case, which is a 2.6 times decrease. The constant astigmatism coefficient is $\text{ahConstant} = 78.5 m\lambda$ for the single achromat case and $\text{ahConstant} = 68.7 m\lambda$ for the double achromat case. The linear astigmatism coefficient was estimated as ayLinear

= $-30.6 \lambda/mm$ for the single achromat case and $ayLinear = -16.4 \lambda/mm$ for the double achromat case. Clearly, the misalignment related astigmatism coefficients do not change appreciably with tube lens design. The linear and constants coma coefficients of the nodal aberration theory are determined from the coma values measured by the OTF-based method at five points along the field direction (see Figure 3.5 and 3.6). We use a weighted least-squares fit with the inverse of the measurement error squared as weight. For the single achromat case we estimated $c_{linear} = 194 \pm 23 \lambda/mm$, $c_{xConstant} = -137 \pm 9 m\lambda$, and $c_{yConstant} = 24 \pm 6 m\lambda$, and for the double achromat case $c_{linear} = 222 \pm 32 \lambda/mm$, $c_{xConstant} = -138 \pm 13 m\lambda$, and $c_{yConstant} = 22 \pm 9 m\lambda$. The comatic aberration

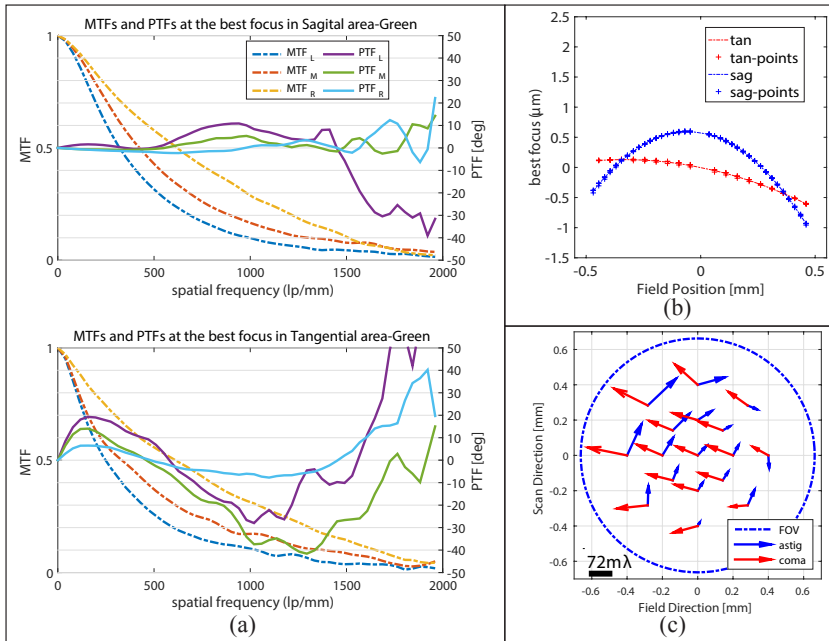


Figure 3.4: Results for the Olympus 20 \times /0.75 objective lens with double back-to-back achromat tube lens. (a) MTFs (dashed) and PTFs (solid) at the overall best focus along field direction. Subscripts L, M, and R denote the left, middle and right side of the FOV and correspond to positions -0.4, 0 and 0.4 mm in the field direction. (b) Measured field curvatures. (c) Full-field aberration map measured by the Shack-Hartmann sensor.

coefficients do not change significantly, as opposed to the astigmatic aberration coefficients. It should be mentioned that the measurement of relatively high coma values (higher than about $120 m\lambda$) from the PTF can be inaccurate and that the estimation of the nodal aberration coefficients from the PTF-based coma values is rather sensitive to the details of the fitting procedure. For example, estimating c_{linear} for the single achromat case with three field points gives $239 \pm 32 m\lambda$, and for five field points with the MTF as weight instead of the inverse squared error gives $181 \pm 7 m\lambda$.

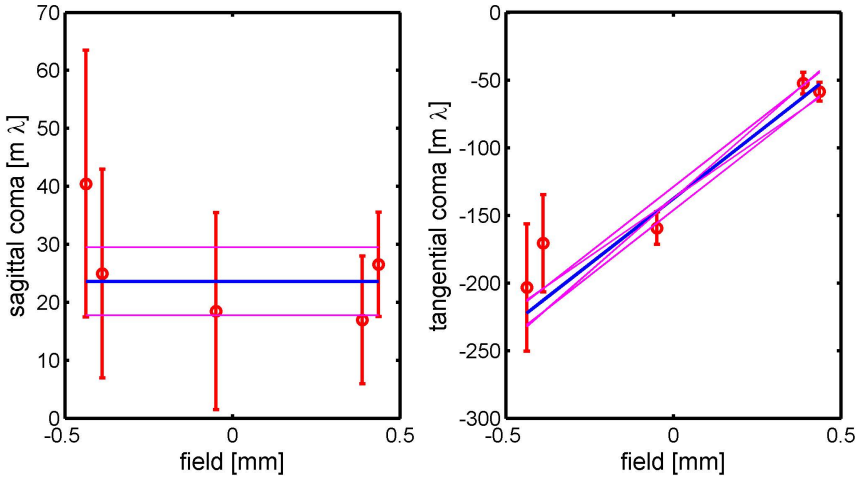


Figure 3.5: Measured sagittal and tangential coma (red) for the single achromat tube lens design using the nodal aberration theory (blue). The magenta lines indicate the error to the fitted curves.

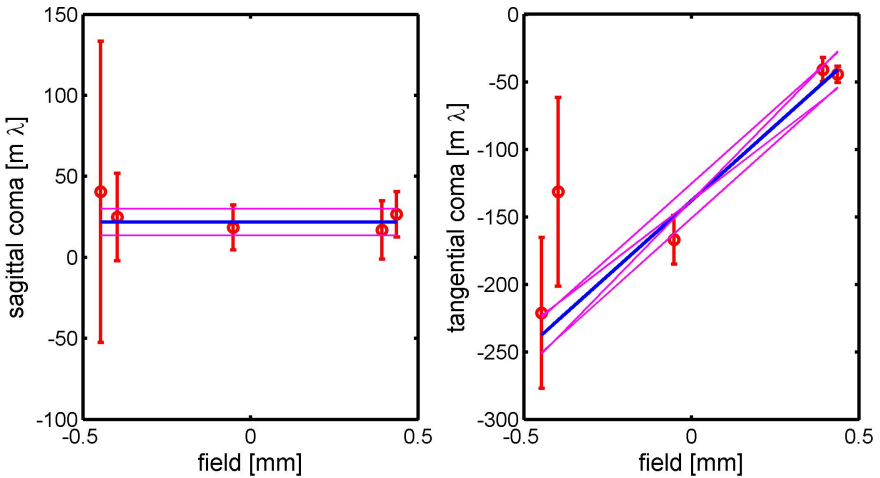


Figure 3.6: Measured sagittal and tangential coma (red) for the double back-to-back achromat tube lens design using the nodal aberration theory (blue). The magenta lines indicate the error to the fitted curves.

3.3.2. FULL-FIELD ABERRATION MAP ANALYSIS

We have analyzed the full-field aberration maps for the two tube lens designs (see Figure 3.7 and 3.8). We found that the description of the maps using the approach of Thompson, Tessieres and others is quite satisfactory, as the residuals of the fitted map are quite small. It is also apparent from the decomposition of the maps in constant, linear and quadratic contributions that a significant component of the overall level of astigmatism and coma is due to misalignment. These misalignment contributions (constant coma, constant astigmatism, linear astigmatism) do not differ substantially between the two tube lens cases, indicating that the root cause of these aberrations is a misalignment within the lens assembly of the objective lens. The effect of tube lens design shows up in the quadratic astigmatism component, which is substantially reduced in the double achromat design ($a_{quadratic} = -0.37\lambda/mm^2$) compared to the single achromat design ($a_{quadratic} = -0.89\lambda/mm^2$), which amounts to a 2.4 times reduction. The relative improvement of the quadratic astigmatism coefficient is in good agreement with the OTF based method, but the absolute values differ by 50-60%. The coma coefficients are for

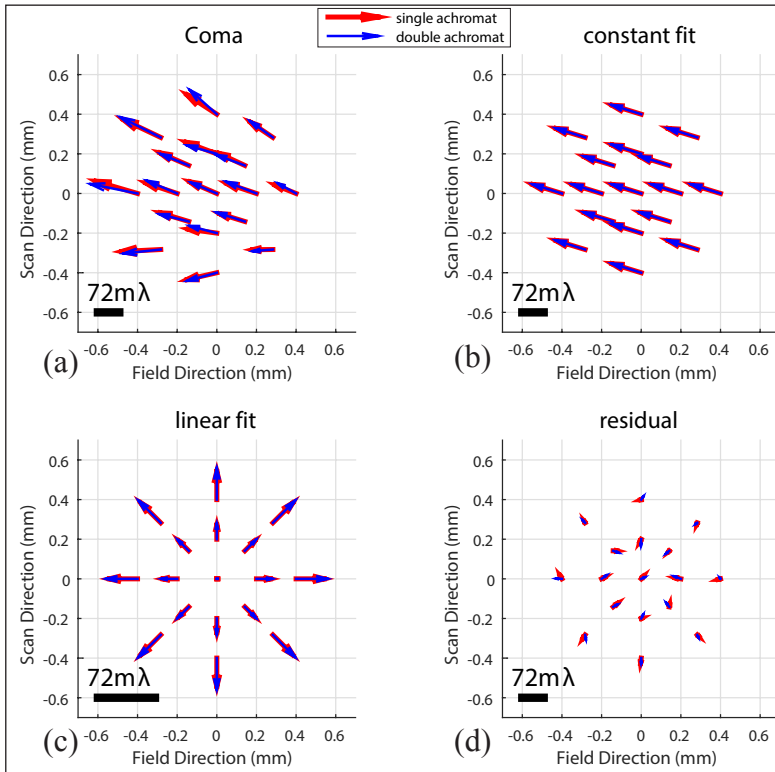


Figure 3.7: Full-field coma map for the Olympus 20x/0.75 objective lens with either the single achromat (red arrows) or the double back-to-back achromat (blue arrows) tube lens. The measured coma map (a) is decomposed to its components: (b) constant coma fit, (c) linear coma fit, and (d) residual coma.

the single achromat case: $c_{linear} = 89 m\lambda/mm$, $c_{xConstant} = -98 m\lambda$, and $c_{yConstant} = 30 m\lambda$, and for double achromat case: $c_{linear} = 99 m\lambda/mm$, $c_{xConstant} = -99 m\lambda$, and $c_{yConstant} = 31 m\lambda$. Clearly, these values do not change significantly for the two tube lens designs, which is in agreement with the OTF-based measurements. However, the coefficients themselves do differ substantially between the two methods. The constant coma coefficients agree reasonable well, but the linear coma coefficient, however, is a factor 2.1 larger for the OTF-based method.

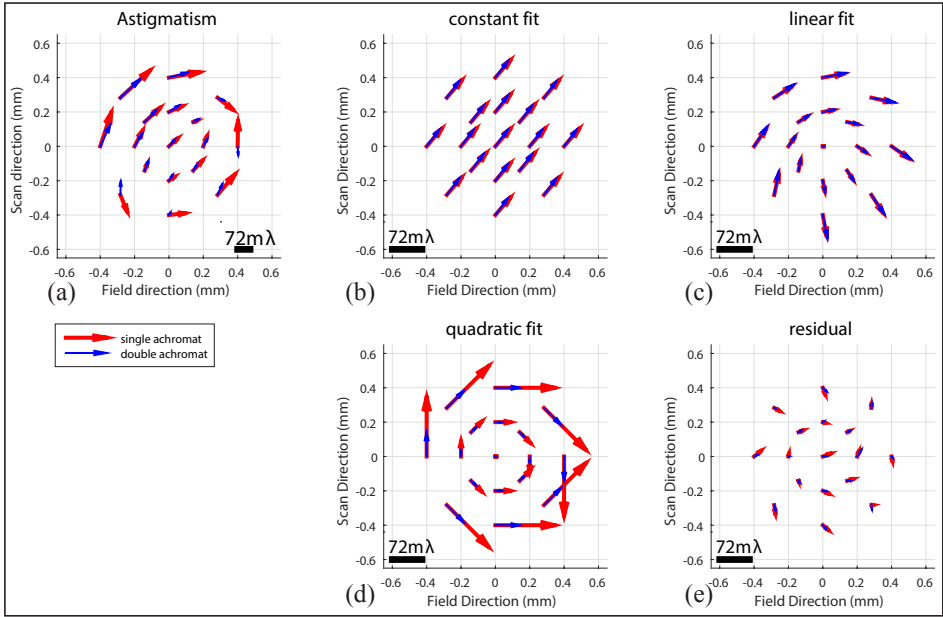


Figure 3.8: Full-field astigmatism map for the Olympus $20\times/0.75$ objective lens with either the single achromat (red arrows) or the double back-to-back achromat (blue arrows) tube lens. The measured astigmatism map (a) is decomposed to its components: (b) constant astigmatism fit, (c) linear astigmatism fit, (d) quadratic astigmatism fit, and (e) residual astigmatism.

We also measured and analyzed the full-field aberration maps for cases with intentional misalignment using the single achromat tube lens design. In particular, we have used a decenter of the objective lens of ~ 3 mm along the field direction of the scanner and a tilt of ~ 2.5 mrad of the objective lens around an axis along the scan direction of the scanner. The amount of tilt we could add is restricted by the mechanical mount of both the objective lens and the Shack-Hartmann sensor. The results are shown in Figure 3.9 and 3.10 for coma and astigmatism respectively. The estimated linear coma coefficient does not change considerably due to misalignment: $c_{linear} = 89$, 79 and 99 $m\lambda/mm$ for the aligned, decentered and tilted cases, respectively, which gives coma of 36 , 32 and 40 $m\lambda$ at 0.4 mm away from the center of the FOV. The estimated quadratic astigmatism coefficient also does not vary considerably: $a_{quadratic} = -0.89$, -0.91 and -0.88 λ/mm^2 for the aligned, decentered and tilted cases, respectively, which gives astigmatism equal to 143 , 146 , and 140 $m\lambda$ at 0.4 mm field position. The constant coma coef-

ficients ($c_{xConstant}$, $c_{yConstant}$) are $(-98,30)$, $(-141,50)$, and $(-109,27)$ $m\lambda$ for the aligned, decentered and tilted cases, respectively, which gives 103, 149, and 112 $m\lambda$ with an average angle of about 163 degree. This indicates that decenter has a significant impact on the constant coma coefficients $c_{xConstant}$ and $c_{yConstant}$. The constant astigmatism coefficients ($a_{hConstant}$, $a_{dConstant}$) are $(-8,54)$, $(-6,66)$, and $(-25,68)$ $m\lambda$ for the aligned, decentered and tilted cases, respectively, which gives 55, 66, and 73 $m\lambda$ with an average angle of 51 degree. This implies that the used misalignments do not impact these coefficients significantly. The linear astigmatism coefficients ($a_{xLinear}$, $a_{yLinear}$) are $(43,-117)$, $(4,-93)$, and $(232,-118)$ λ/mm for the aligned, decentered and tilted cases, respectively. Apparently, decenter has a minor impact on astigmatism and tilt has a major impact on astigmatism. Moreover, the effect is largely restricted to the coefficient $a_{xLinear}$ which agrees with the direction of tilt. The averaged residual coma over the FOV is 9, 30, and 11 $m\lambda$ and the averaged residual astigmatism over the FOV is 8, 12, 13 $m\lambda$ for the aligned, decentered and tilted cases, respectively. This implies that the experimental data is well described by the nodal aberration theory.

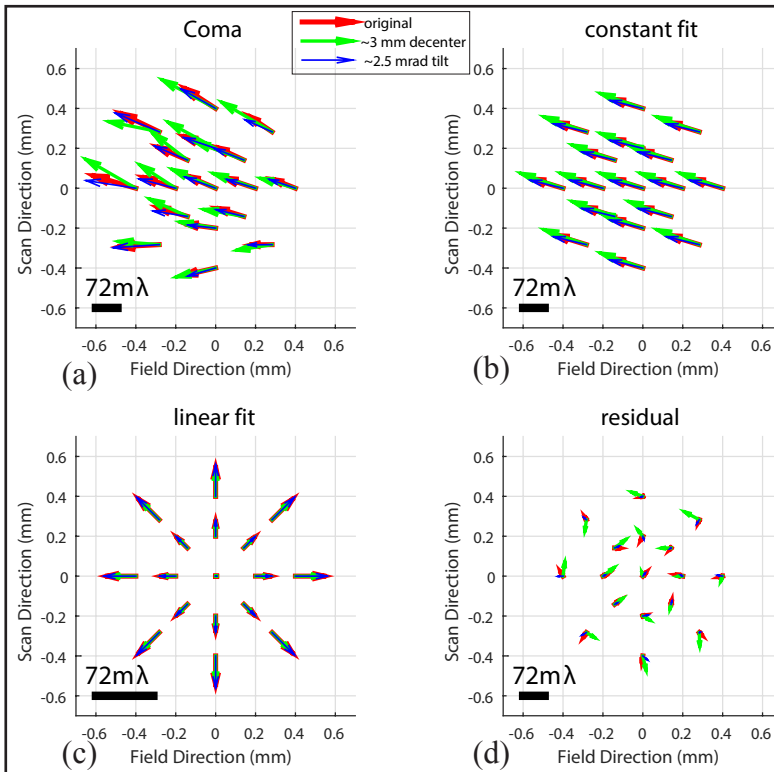


Figure 3.9: Full-field coma map for the Olympus 20 \times /0.75 objective lens with the single achromat (red arrows: original alignment, green arrows: 3mm decenter of objective lens along field position to the left, blue arrows: 2.5 mrad tilt of objective lens around an axis along the scan direction of the scanner). The measured coma map (a) is decomposed to its components: (b) constant coma fit, (c) linear coma fit, and (d) residual coma.

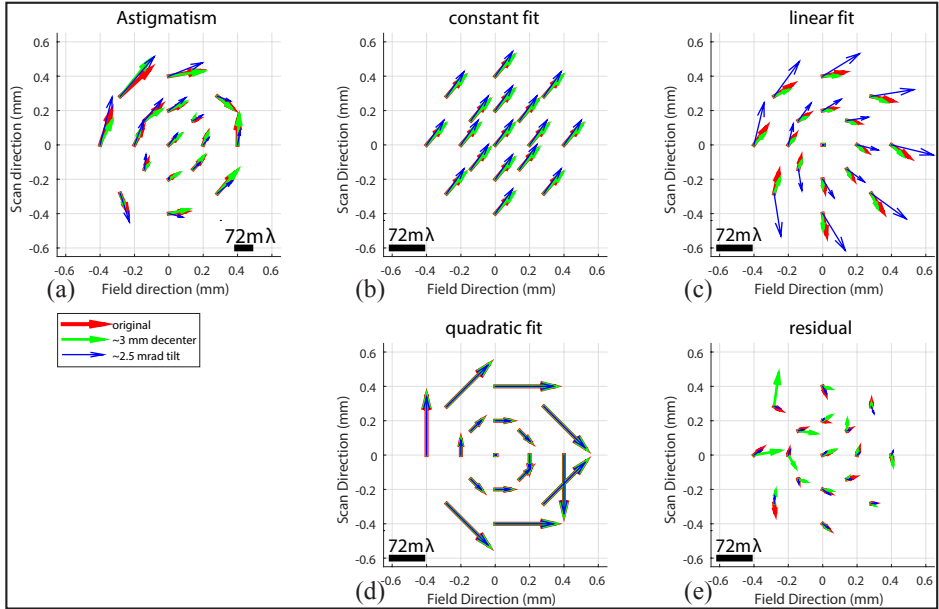


Figure 3.10: Full-field astigmatism map for the Olympus 20 \times /0.75 objective lens with the double back-to-back achromat (red arrows: original alignment, green arrows: 3mm decenter of objective lens along field position to the left, blue arrows: 2.5 mrad tilt of objective lens around an axis along the scan direction of the scanner). The measured astigmatism map (a) is decomposed to its components: (b) constant astigmatism fit, (c) linear astigmatism fit, (d) quadratic astigmatism fit, and (e) residual astigmatism.

3.4. CONCLUSION

We have measured full-field aberration maps of WSI system by using a Shack-Hartmann wavefront sensor setup. These maps have been analyzed with nodal aberration theory in order to disentangle aberrations that are inherent to the optical design from aberrations that arise from misalignment. We have restricted the analysis to the lowest order astigmatism and coma. For these two types of aberrations two coefficients quantify the level of aberrations from design and another six coefficients are a measure of the composite level of misalignment. We have experimentally compared two different tube lens designs and confirmed that only the optical design related astigmatism coefficient differs. Intentional decenter of the objective lens predominantly impacts the misalignment related coefficients for constant coma, and intentional tilt of the objective lens has a significant effect on the misalignment related coefficients for linear astigmatism. The full-field aberration map analysis we describe may be used to track root causes of aberrations that are revealed by e.g. through-focus OTF-based measurement, and in this way assess the optical quality of individual optical components such as objective lenses or tube lenses, or to improve the alignment of the different optical components within a WSI system.

REFERENCES

- [1] S. M. Shakeri, B. Hulsken, L. J. van Vliet, and S. Stallinga, *Shack-Hartmann sensor based optical quality testing of whole slide imaging systems for digital pathology*, Proc. SPIE 9315, Design and Quality for Biomedical Technologies VIII , 931504 (2015).
- [2] S. M. Shakeri, B. Hulsken, L. J. van Vliet, and S. Stallinga, *Optical quality assessment of whole slide imaging systems for digital pathology*, Opt. Express **23**, 1319–1336 (2015).
- [3] B. C. Platt and R. Shack, *History and principles of shack-hartmann wavefront sensing*, Journal of Refractive Surgery **17**, S573–S577 (2001).
- [4] P. L. Schechter and R. S. Levinson, *Generic misalignment aberration patterns in wide-field telescopes*, Publications of the Astronomical Society of the Pacific **123**, 812–832 (2011).
- [5] R. V. Shack and K. Thompson, *Influence of alignment errors of a telescope system on its aberration field*, Proc. SPIE, 24th Annual Technical Symposium **0251**, 146–153 (1980).
- [6] R. Tessieres, *Optical Sciences*, Master's thesis, University of Arizona, Tucson (2003).
- [7] J. Wang, B. H. Guo, Q. Sun, and Z. W. Lu, *Third-order aberration fields of pupil de-centered optical systems*, Opt. Express **20**, 11652–11658 (2012).
- [8] K. Thompson, *Description of the third-order optical aberrations of near-circular pupil optical systems without symmetry*, J. Opt. Soc. Am. A **22**, 1389–1401 (2005).
- [9] K. P. Thompson, T. Schmid, O. Cakmakci, and J. P. Rolland, *Real-ray-based method for locating individual surface aberration field centers in imaging optical systems without rotational symmetry*, J. Opt. Soc. Am. A **26**, 1503–1517 (2009).
- [10] K. P. Thompson, T. Schmid, and J. P. Rolland, *Recent discoveries from nodal aberration theory*, International Optical Design Conference **7652**, 76522Q (2010).
- [11] A. Manuel, *College of Optical Science*, Ph.D. thesis, University of Arizona, Arizona (2009).

4

THE IMPACT OF PARTIAL COHERENCE ON THE APPARENT OPTICAL TRANSFER FUNCTION DERIVED FROM THE RESPONSE TO AMPLITUDE EDGES

We present an investigation of the impact of partial coherence on optical imaging systems with the focus on Whole Slide Imaging (WSI) systems for digital pathology. The investigation is based on the analysis of the edge response of the optical system, which gives rise to an apparent Optical Transfer Function (OTF) that can be linked to two elementary complex functions Q and U . The function Q is directly related to the Transmission Cross-Coefficient (TCC) and can be identified with the performance function first introduced by Kintner and Stillitto. The function U depends on the TCC in a more involved way. When there are no aberrations the Q -function corresponds to the real part of the apparent OTF and the U function to the imaginary part of the apparent OTF. Close to the incoherent limit the effect of the U function is a mere shift of the edge compared to the fully incoherent case. We propose a new expression for the dependence of the Depth Of Focus (DOF) on spatial frequency and on the partial coherence factor σ , and validate it by simulation. Partial coherence effects are investigated experimentally on a WSI-system with a compact LED-based Köhler illumination unit with variable condenser NA. This unit incorporates a top hat diffuser for providing a reasonably uniform illumination field, with variations below 10% across the imaged Field Of View (FOV). The measurements of the apparent through-focus OTF derived from edges on a custom resolution chart for different σ were substantially in agreement with the simulations. Finding an optimal value for σ is not

S.M. Shakeri, L.J. van Vliet, and S. Stallinga, submitted to Applied Optics.

straightforward as lateral resolution and the level of edge ringing improve with increasing σ , whereas edge contrast and DOF improve with decreasing σ . We assess that the trade-off for the particular application of WSI systems for digital pathology is optimized for a σ value in the range of 0.55 to 0.75.

4.1. INTRODUCTION

PARTIAL coherence influences image formation in microscopy via the partial coherence factor $\sigma = NA_{\text{ill}}/NA$, the ratio between the illumination (condenser) Numerical Aperture NA_{ill} and the imaging (objective) NA [1–3]. The imaging system transmits spatial frequencies of the sample up to the cutoff $(1 + \sigma)NA/\lambda$ (with λ the wavelength), so that the resolution increases towards the incoherent limit. On the other hand, the sharpness in the image, that can be quantified by the steepness of the edge response, improves towards the coherent limit. This beneficial effect, however, is accompanied by edge ringing artefacts. A trade-off between these effects can subjectively be defined based on the imaging application that is considered. A general rule of thumb in the field of microscopy is to slightly sacrifice resolution for image sharpness by reducing the illumination NA_{ill} to about 0.75 times the imaging NA .

This partial coherence tradeoff becomes even more involved when aberrations are taken into account. Several theoretical studies have appeared with regard to this issue. Barakat [4] investigated the effect of defocus and coma on amplitude edge and bar objects under partially coherent illumination. He found that the edge in the image is shifted compared to the edge in the underlying object towards the bright side of the edge, where the shift increases with decreasing σ . This topic has received further attention by Kirk [5] in the context of linewidth measurements with a microscope. Ichioka and Suzuki [6] studied complex periodic objects, and Hild et al. [7] studied the behavior of the intensity distribution and its first derivative for amplitude, phase and amplitude/phase bars. They found that the asymmetric behavior of the first derivative is strongly correlated with σ and the phase content of the object.

In particular the sensitivity of the optical system with respect to defocus, quantified by the Depth Of Focus (DOF), is a highly relevant parameter. It appears that the DOF increases towards the coherent limit [8, 9], although no comprehensive study has appeared on this aspect. In the field of lithography, an optimum value for the imaging NA and σ is found based on a desired DOF and a particular mask pattern [10, 11], even introducing novel metrics for DOF [12]. Von Waldkirch et al. [13, 14] investigated the influence of partial coherence on the DOF for a retinal projection display. They showed that a value for σ between 0.35 and 0.5 provided the best DOF for text readability. Ren et al. [15] have empirically studied the effect of the condenser NA on cytogenetic imaging with a brightfield microscope and found an optimum value of the partial coherence factor in the range 0.6 to 0.7. These examples imply that the optimum in the partial coherence tradeoff apparently depends on the application requirements.

Previously, we proposed a method for testing and monitoring the optical quality of Whole Slide Imaging (WSI) systems using a measurement of the through-focus Optical Transfer Function (OTF) obtained from the edge response of a custom made resolution target [16]. In this analysis it was assumed that the imaging system is incoherent. As a partially coherent system is non-linear the OTF derived from the edge response is not a

true transfer function but rather an apparent OTF. It may be expected, however, that it is still possible to use it to characterize the optical quality of the imaging system. Wernick and Morris [17] have analyzed the effects of partial coherence on the apparent MTF for square apertures, and found an increase in the apparent MTF for the lower spatial frequencies with decreasing σ . This reflects the increase in edge steepness towards the coherent limit. Kintner and Stillito [18] proposed to characterize the edge response of a partially coherent optical imaging systems by a single function, the so-called "performance function", for adequately describing the cross-over between the incoherent and coherent limits.

So far, an in-depth investigation of the apparent OTF derived from the edge response has not been reported. The impact of aberrations, in particular defocus, on the apparent OTF has also remained unclear. The goals of this chapter are (i) to provide simulations and measurements of the effect of the partial coherence factor σ on the apparent OTF, (ii) assess effects of aberrations in the partial coherence regime, in particular the impact of defocus quantified by the DOF, (iii) evaluate the partial coherence tradeoff for the application in Whole Slide Imaging (WSI) systems for digital pathology.

This chapter is structured as follows. In the theory and simulation section we first briefly summarize partial coherence theory, focusing on the apparent OTF derived from the edge response, and the effects of partial coherence on edge ringing, DOF, and the impact of aberrations. In the experiments section, we describe the design of a color sequential Köhler illumination unit used to measure the effect of the partial coherence factor on the apparent OTF. Finally, we will discuss the results and the implications for WSI systems.

4.2. THEORY AND SIMULATION

4.2.1. APPARENT TRANSFER FUNCTIONS AND PERFORMANCE FUNCTION

According to Hopkins' treatment of partially coherent optical imaging systems [1, 2], the measured intensity on the detector is given by:

$$I(\vec{r}) = \int d^2r_1 d^2r_2 P(\vec{r} - \vec{r}_1) P^*(\vec{r} - \vec{r}_2) J(\vec{r}_1 - \vec{r}_2) T(\vec{r}_1) T(\vec{r}_2)^* \quad (4.1)$$

where $P(\vec{r})$ is the coherent Point Spread Function (PSF), $J(\vec{r})$ is the mutual intensity, and $T(\vec{r})$ is the complex amplitude transmission of the object. The integration domain is taken to extend from $-\infty$ to $+\infty$ for all integration variables. We adopt this convention in this paper unless the domain is specified explicitly. The Fourier Transform (FT) of the coherent PSF as a function of spatial frequency \vec{q} is:

$$\hat{P}(\vec{q}) = C(\vec{q}\lambda/\text{NA}) \exp(2\pi i W(\vec{q}\lambda/\text{NA})/\lambda), \quad (4.2)$$

where $W(\vec{\rho})$ is the aberration function, depending on the normalized pupil coordinates $\vec{\rho} = \vec{q}\lambda/\text{NA}$, and where $C(\vec{\rho})$ is the circle function (equal to one inside the unit circle, equal to zero outside the unit circle). The FT of the mutual intensity is:

$$\hat{J}(\vec{q}) = \frac{1}{\pi a^2} C(\vec{q}\lambda/(\sigma\text{NA})), \quad (4.3)$$

where $a = \min(\sigma, 1)$ and σ is the partial coherence factor. The intensity can be expressed in terms of the FT quantities as:

$$I(\vec{r}) = \int d^2 q d^2 q' S(\vec{q}, \vec{q}') \hat{T}(\vec{q}) \hat{T}(\vec{q}')^* \exp(2\pi i (\vec{q} - \vec{q}') \cdot \vec{r}), \quad (4.4)$$

where the so-called Transmission Cross Coefficient (TCC) is given by:

$$S(\vec{q}, \vec{q}') = \int d^2 q'' \hat{J}(\vec{q}'') \hat{P}(\vec{q} + \vec{q}'') \hat{P}(\vec{q}' + \vec{q}'')^*. \quad (4.5)$$

The FT of the mutual intensity is normalized such that $S(0, 0) = 1$, implying that a uniform normalized object $T(\vec{r}) = 1$ gives rise to a uniform normalized intensity signal $I(\vec{r}) = 1$. It may be deduced that object spatial frequencies below $(1 + \sigma) \text{NA}/\lambda$ contribute to the intensity signal and that the highest spatial frequency in the intensity signal is $2\text{NA}/\lambda$, regardless of the partial coherence factor σ . For $\sigma = 0$ we retrieve the fully coherent case, for $\sigma \rightarrow \infty$ we retrieve the fully incoherent case.

An important function in the subsequent analysis is:

$$\hat{Q}(\vec{q}) \equiv S(\vec{q}, 0) = \int d^2 q' \hat{J}(\vec{q}') \hat{P}(\vec{q}')^* \hat{P}(\vec{q} + \vec{q}'), \quad (4.6)$$

Taking the inverse Fourier transform of this complex function gives:

$$Q(\vec{r}) = P(\vec{r}) \tilde{P}(\vec{r})^*, \quad (4.7)$$

where:

$$\tilde{P}(\vec{r}) = \int d^2 q \hat{J}(\vec{q}) \hat{P}(\vec{q}) \exp(2\pi i \vec{q} \cdot \vec{r}). \quad (4.8)$$

The function $Q(\vec{r})$ is called the performance function by Kintner and Stillitto [18]. For $\sigma \geq 1$ it reduces to the incoherent PSE, for $\sigma \ll 1$ it reduces to the coherent PSE. Sheppard arrives at (the FT of) the same function in the analysis of the response to weak objects in the context of quantitative phase imaging [19] and calls it the Weak OTF (WOTF).

We now apply this formalism to the analysis of the step response. First, we use a change of integration variables to express the image as:

$$\begin{aligned} I(\vec{r}) &= \frac{1}{4} \int d^2 q_1 d^2 q_2 S\left(\frac{\vec{q}_2 + \vec{q}_1}{2}, \frac{\vec{q}_2 - \vec{q}_1}{2}\right) \\ &\quad \times \hat{T}\left(\frac{\vec{q}_2 + \vec{q}_1}{2}\right) \hat{T}\left(\frac{\vec{q}_2 - \vec{q}_1}{2}\right)^* \exp(2\pi i \vec{q}_1 \cdot \vec{r}), \end{aligned} \quad (4.9)$$

For a step object we have:

$$T(\vec{r}) = \theta(x), \quad (4.10)$$

with FT:

$$\hat{T}(\vec{q}) = \frac{\delta(q_y)}{2\pi i (q_x - i\epsilon)}, \quad (4.11)$$

and ε an infinitesimal real positive number. Inserting this expression in the general formula for the intensity gives the edge response. The Line Spread Function (LSF) then follows by differentiation as:

$$\frac{dI(x)}{dx} = \int dq \hat{H}(q, 0) \exp(2\pi i q x). \quad (4.12)$$

with:

$$\hat{H}(q, 0) = \frac{i}{\pi} \int_{-\infty}^{+\infty} dq' \frac{qS((q' + q)/2, 0, (q' - q)/2, 0)}{q'^2 - (q - i\varepsilon)^2}. \quad (4.13)$$

The transfer function $\hat{H}(q, 0)$ is the apparent OTF extracted from the LSF. The apparent OTF is Hermitian ($\hat{H}(q, 0) = \hat{H}(-q, 0)^*$) because the line spread function is real. Using the Plemelj formula of complex analysis:

$$\frac{1}{q - i\varepsilon} = P\left(\frac{1}{q}\right) + i\pi\delta(q), \quad (4.14)$$

where 'P' indicates the principal value, it may be shown that:

$$\hat{H}(q, 0) = \frac{1}{2} (\hat{Q}(q, 0) + \hat{Q}(-q, 0)^*) + \hat{U}(q, 0), \quad (4.15)$$

with:

$$\hat{U}(q, 0) = \frac{i}{\pi} P \int_{-\infty}^{+\infty} dq' \frac{qS((q' + q)/2, 0, (q' - q)/2, 0)}{q'^2 - q^2}. \quad (4.16)$$

a Hermitian function of q ($\hat{U}(q, 0) = \hat{U}(-q, 0)^*$). Apparently, the first term on the right hand side of Eq. (4.15) can be directly related to the TCC and the performance function, but the second term on the right hand side of Eq. (4.15) is considerably more involved. The apparent OTF can be similarly defined for an arbitrary edge orientation as:

$$\hat{H}(\vec{q}) = \frac{1}{2} (\hat{Q}(\vec{q}) + \hat{Q}(-\vec{q})^*) + \hat{U}(\vec{q}), \quad (4.17)$$

The edge response and the LSF derived from it depend on the edge type for partially coherent systems. Repeating the previous analysis for a general edge profile $T(x, y) = a - b/2 + b\theta(x)$ with a and b arbitrary complex numbers, gives a LSF:

$$\frac{dI(x)}{dx} = \text{Re} \{2a^* b Q(x, 0)\} + |b|^2 U(x, 0), \quad (4.18)$$

where $U(\vec{r})$ is the inverse FT of $\hat{U}(\vec{q})$. The apparent OTF for an arbitrary edge orientation then follows as the linear combination:

$$\hat{H}(\vec{q}) = a^* b \hat{Q}(\vec{q}) + ab^* \hat{Q}(-\vec{q})^* + |b|^2 \hat{U}(\vec{q}). \quad (4.19)$$

The amplitude edge case, for which the Hermitian part of the performance function appears, is retrieved for $a = 1/2$ and $b = 1$. For a $\pi/2$ phase edge ($a = 1$, $b = 2i$) the ant-Hermitian (imaginary & antisymmetric) part of the performance function appears

rather than the Hermitian part. For a π phase edge ($a = 0, b = 2i$) the performance function plays no role at all. In the weak object limit ($|a| \gg |b|$) the partially coherent system becomes linear and the LSF is fully determined by the performance function.

For the unaberrated case it appears that $\hat{Q}(\vec{q})$ is real and symmetric, and $\hat{U}(\vec{q})$ is imaginary and antisymmetric. It follows that the real symmetric part of the apparent OTF is determined by the FT of the performance function, and the imaginary antisymmetric part of the apparent OTF is determined by the transfer function $\hat{U}(\vec{q})$. An asymptotic analysis of Eq. (4.16) in the limit $\sigma \gg 1$ (see Appendix) results in an apparent Phase Transfer Function (PTF) equal to:

$$\arg\{\hat{H}(\vec{q})\} = -\frac{q\lambda}{\pi NA\sigma}, \quad (4.20)$$

which implies that close to the incoherent limit the primary effect of partial coherence is an apparent shift of the edge over a distance $\Delta x = \lambda / (2NA\pi^2\sigma)$ towards the bright side of edge. This provides a quantitative description of the edge shifting effect first noted by Barakat [4]. It is noteworthy that this apparent edge shift persists for all finite σ , even though the real part of the OTF remains equal to the incoherent OTF for all $\sigma \geq 1$.

4.2.2. EDGE RINGING

For the aberration-free case the FT of the performance function corresponds to the overlap integral of two displaced pupils, one with normalized radius equal to one, and the other with normalized radius equal to σ . An analytical expression for this overlap integral is [19]:

$$\begin{aligned} \hat{Q}(\vec{q}) = & \frac{1}{\pi\sigma^2} \left[\arccos\left(\frac{\rho^2 + 1 - \sigma^2}{2\rho}\right) \right. \\ & \left. + \sigma^2 \arccos\left(\frac{\rho^2 - 1 + \sigma^2}{2\sigma\rho}\right) - \sqrt{\rho^2 - \left(\frac{\rho^2 + 1 - \sigma^2}{2}\right)^2} \right], \end{aligned} \quad (4.21)$$

with the normalized spatial frequency $\rho = |\vec{q}| \lambda / NA$, and where $1 - \sigma \leq \rho \leq 1 + \sigma$. For $\rho < 1 - \sigma$ we have $\hat{Q}(\vec{q}) = 1$ and for $\rho > 1 + \sigma$ we have $\hat{Q}(\vec{q}) = 0$, giving a spatial frequency cutoff equal to $(1 + \sigma) NA / \lambda$. Figure 4.1 shows the effective Modulation Transfer Function (MTF) $|\hat{Q}(\vec{q})|$ according to Eq. (4.21) for different σ values, showing the crossover from the fully coherent behavior at $\sigma = 0$ to the fully incoherent behavior at $\sigma = 1$. The performance function for the non-aberrated system is the product of two Airy-distributions:

$$Q(\vec{r}) = \pi \left[\frac{2J_1(2\pi r NA / \lambda)}{2\pi r NA / \lambda} \right] \left[\frac{2J_1(2\pi r \sigma NA / \lambda)}{2\pi r \sigma NA / \lambda} \right]. \quad (4.22)$$

Kintner and Stillitto [18] have derived a condition on the performance function that is necessary and sufficient for avoiding edge ringing. This condition is:

$$\operatorname{Re}\{Q(\vec{r})\} \geq 0 \quad (4.23)$$

for all positions \vec{r} . The performance function of Eq. (4.22) can become negative for any value $\sigma < 1$, thereby violating Kintner and Stillitto's condition. It may be concluded that

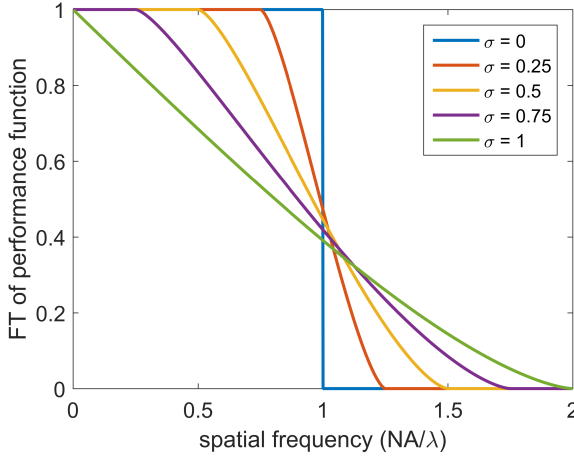


Figure 4.1: FT of the performance function, equal to the real part of the apparent OTF, as a function of spatial frequency of aberration-free in-focus partially coherent imaging systems for different values of the partial coherence factor σ .

edge ringing can never be completely avoided in partially coherent imaging systems. The appearance of edge ringing may also be related to violations of the so-called Lukosz-bound [20]. A practical tolerance limit to avoid edge ringing may be found by requiring that the first minimum of the first Airy distribution in Eq. (4.22) at $r = 0.817\lambda/\text{NA}$ coincides with the first zero of the second Airy distribution in Eq. (4.22) at $r = 0.610\lambda/\sigma\text{NA}$, implying that $\sigma = 0.610/0.817 \approx 0.75$. The rule-of-thumb is therefore that edge ringing will only become appreciable if σ drops below this critical value. The limit of $\sigma = 0.75$ corresponds to the actual practice in microscopy.

In digital imaging the edge ringing fringes in the measured step response are smoothed because the signal is integrated over the non-zero pixel size. Figure 4.2a shows the edge response taking this smoothing effect into account, and Fig. 4.2b shows the corresponding edge overshoot values for different σ . We assume a pixel size $\lambda/4\text{NA}$, in agreement with the Nyquist criterion. It is mentioned that the highest spatial frequency in the intensity signal $I(\vec{r})$ for an arbitrary 2D-object is $2\text{NA}/\lambda$ for all σ , even though the highest spatial frequency of the complex amplitude object function $T(\vec{r})$ contributing to the intensity signal is $(1 + \sigma)\text{NA}/\lambda$. This justifies the use of the same Nyquist size pixels for all values of σ . It may be seen that the edge overshoot approaches zero when $\sigma \rightarrow 1$ and remains below 20% for all σ , for $\sigma = 0.75$ the edge overshoot is just 3.4%. Figure 4.2c shows the apparent MTF, and Fig. 4.2d shows the apparent PTF derived from the edge responses shown in Fig. 4.2a. The MTF-curves confirm that the signal contains spatial frequencies up to $2\text{NA}/\lambda$, the non-zero PTF-curves result from the asymmetry in the LSF and approach the linear slope of Eq. (4.20) close to the incoherent limit. The increase in the apparent MTF for the lower spatial frequencies with decreasing σ agrees with the findings of Ref. [17] for the square aperture case. For $\sigma < 1$ the OTF is fully imaginary for spatial frequencies $q > (1 + \sigma)\text{NA}/\lambda$, giving a plateau equal to $-\pi/2$ in the PTF (up to numerical errors of a few degrees). Figure 4.2 e and f show the numerically simulated real and imaginary part of the apparent OTF. The real part of the apparent OTF substan-

tially agrees with the theoretical curves shown in Fig. 4.1, the non-zero imaginary part of the apparent OTF prove that the FT of the performance function is not identical to the apparent OTF for an amplitude edge.

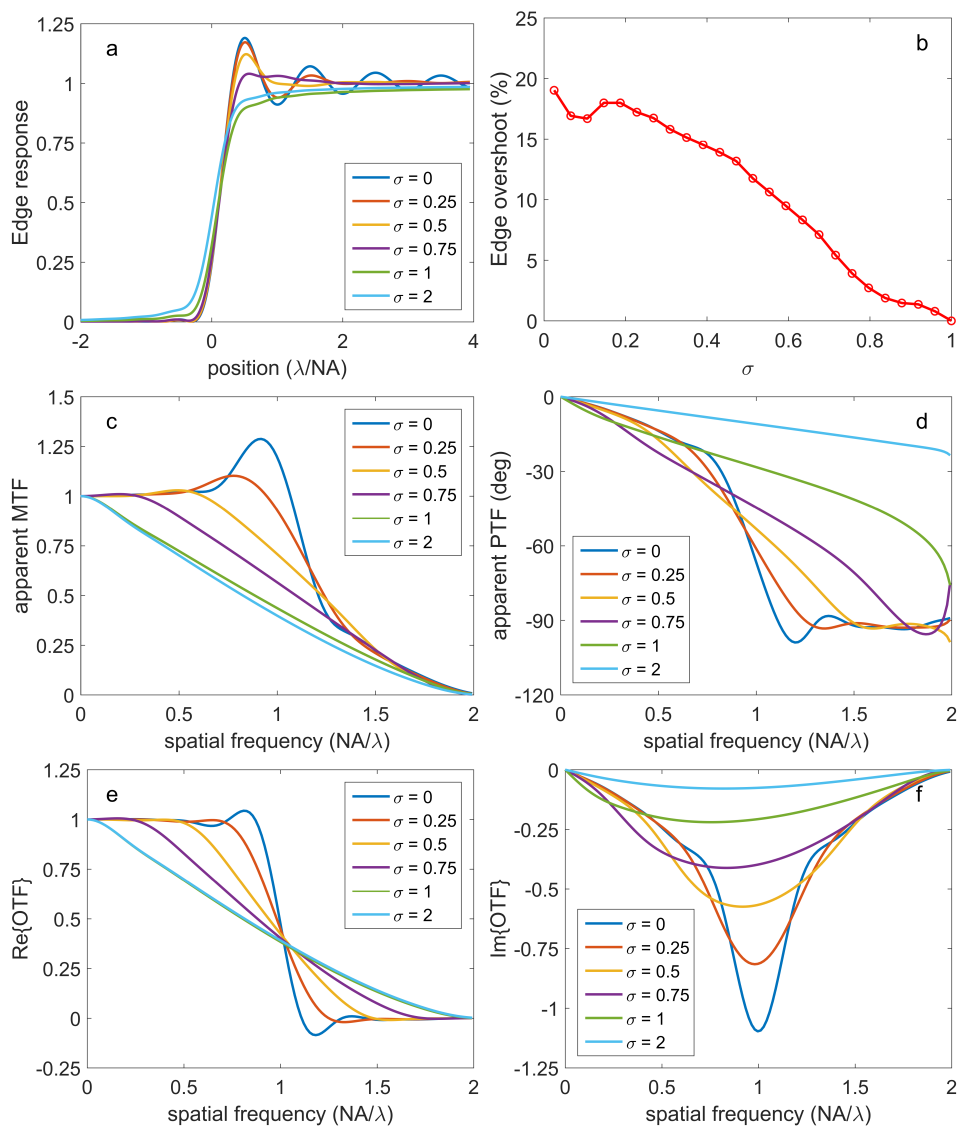


Figure 4.2: (a) Numerically computed edge response for different values of the partial coherence factor σ . (b) Edge overshoot as a function of the partial coherence factor σ . (c-d) Apparent MTF and PTF derived from the edge response for different values of the partial coherence factor σ . (e-f) Real and imaginary part of the apparent OTF derived from the edge response for different values of the partial coherence factor σ .

4.2.3. DEPTH OF FOCUS

The next important factor to investigate is the dependence on defocus. There are two complications in this analysis. The first is that the edge response and the attendant LSF depend on the object type and appear to depend on the FT of the performance function $\hat{Q}(\vec{q})$ for a weak edge, or generally on the transfer function $\hat{U}(\vec{q})$ as well. The second is that the sensitivity to defocus appears to depend on the spatial frequency.

We will first focus our attention on the transfer function $\hat{Q}(\vec{q})$ defined by the overlap integral Eq. (4.6) between a circle with unit radius and a circle with radius σ displaced over a distance $\rho = |\vec{q}| \lambda / \text{NA}$. The aberration function for defocus in the paraxial limit of low NA is:

$$W(x, y) = \frac{1}{2} z \text{NA}^2 (x^2 + y^2). \quad (4.24)$$

with z the defocus and $\vec{\rho} = (x, y)$ the normalized pupil coordinates. The phase in the overlap region of the two circles with unit radius and radius σ then is:

$$\begin{aligned} \Delta\Phi(\rho, x, y) &= \frac{2\pi}{\lambda} (W(x, y) - W(x - \rho, y)) \\ &= \frac{\pi z \text{NA}^2}{\lambda} (2\rho x - \rho^2), \end{aligned} \quad (4.25)$$

which has a maximum value in the overlap region at $(x, y) = (1, 0)$ and a minimum at $(x, y) = (\rho - \sigma, 0)$, giving a peak-valley value:

$$\begin{aligned} \Phi_{\text{p-v}}(\rho) &= \Delta\Phi(\rho, 1, 0) - \Delta\Phi(\rho, \rho - \sigma, 0) \\ &= \frac{2\pi z \text{NA}^2 \rho (1 + \sigma - \rho)}{\lambda}. \end{aligned} \quad (4.26)$$

A significant decay of the modulus $|\hat{Q}(\vec{q})|$ due to a defocus z may be typically found if the distribution of phases in Eq. (4.25) across the overlap region spans the range from 0 to $\beta\pi$, where β is a numerical factor on the order of unity. Requiring $\Phi_{\text{p-v}}(\rho) = \beta\pi$ results in an 'in-focus' layer $\Delta z/2 \leq z \leq \Delta z/2$ for which $-\beta\pi \leq \Phi_{\text{p-v}}(q) \leq \beta\pi$ with thickness:

$$\Delta z = \frac{\beta\lambda}{\text{NA}^2 \rho (1 + \sigma - \rho)}. \quad (4.27)$$

The minimum of this defocus range as a function of normalized spatial frequency ρ occurs at $\rho = (1 + \sigma)/2$ and may be identified with the Depth Of Focus:

$$\text{DOF} = \frac{4\beta\lambda}{\text{NA}^2 (1 + \sigma)^2}. \quad (4.28)$$

The numerical factor β takes different values depending on the degree of defocus which is tolerated. The analogon to Maréchal's diffraction limit may be found by requiring a peak-valley phase in the overlap integral $\Phi_{\text{p-v}}(q) = \pi$, which corresponds to the crossover point from constructive to destructive interference. This results in a value $\beta = 1/2$. Capturing the largest fraction of the 'in-focus' layer typically corresponds to $\beta = 2$, i.e. four times larger than the diffraction limit. It appears empirically that the Full Width Half

Maximum (FWHM) of the through-focus transfer function $|\hat{Q}(\vec{q})|$ corresponds to $\beta \approx \sqrt{2}$. The use of a threshold on the through-focus MTF for defining a DOF metric has been proposed for incoherent imaging systems previously by Qiu et al. [21]. The scaling of Eq. (4.28) with σ as $1/(1+\sigma)^2$ has also been found by Ren et al. [15].

This analysis may be generalized to focusing into a medium with refractive index n and beyond the paraxial limit. The aberration function for defocus is then:

$$W(x, y) = nz \left(1 - \sqrt{1 - \text{NA}^2 (x^2 + y^2) / n^2} \right). \quad (4.29)$$

This results in a predicted allowable defocus range:

$$\begin{aligned} \Delta z &= \beta\lambda \left[\sqrt{n^2 - \text{NA}^2 (1 - \rho)^2} + \sqrt{n^2 - \text{NA}^2 (\sigma - \rho)^2} \right. \\ &\quad \left. - \sqrt{n^2 - \text{NA}^2} - \sqrt{n^2 - \sigma^2 \text{NA}^2} \right]^{-1}. \end{aligned} \quad (4.30)$$

At normalized spatial frequency $\rho = (1 + \sigma) / 2$ we find the DOF as:

$$\begin{aligned} \text{DOF} &= \beta\lambda \left[2\sqrt{n^2 - \text{NA}^2 (1 - \sigma)^2} / 4 \right. \\ &\quad \left. - \sqrt{n^2 - \text{NA}^2} - \sqrt{n^2 - \sigma^2 \text{NA}^2} \right]^{-1}. \end{aligned} \quad (4.31)$$

This analysis points to two salient features. First, the decay of the through-focus transfer function $|\hat{Q}(\vec{q})|$ as a function of defocus depends on the spatial frequency: For the middle spatial frequencies the decay is steep, for low and high spatial frequencies the decay is only mild. Second, for low σ the decay of the through-focus transfer function $|\hat{Q}(\vec{q})|$ with defocus is steeper than for high σ , implying that the DOF increases toward the coherent limit.

These predictions may be tested with a numerical computation of the through-focus transfer function $|\hat{Q}(\vec{q})|$ for different σ . Figure 4.3 shows these numerical results for a range of σ values. We have taken $\text{NA} = 0.15$ so as to be close to the paraxial limit. Figure 4.4 shows the FWHM-values as a function of spatial frequency numerically determined from the through-focus transfer function, and the model curves according to Eq. (4.27) with $\beta = \sqrt{2}$. The agreement between the curves is very good for $\sigma \geq 0.5$ and describes the trend qualitatively for $\sigma < 0.5$.

As mentioned before, the transfer function $\hat{Q}(\vec{q})$ does not fully describe the LSF derived from the edge response. Figure 4.5 shows the apparent through-focus MTF $|\hat{H}(\vec{q})|$ derived from the amplitude edge response, and Fig. 4.6 shows the numerically determined FWHM-values as a function of spatial frequency. It appears that for spatial frequencies $q < \text{NA}/\lambda$ the dependence of the FWHM on spatial frequency and partial coherence factor agrees reasonably well with the FWHM derived from the FT of the performance function. For larger spatial frequencies, typically above NA/λ , the FWHM drops to levels comparable to the FWHM for $\sigma = 1$ for all σ .

Focus errors in whole slide scanning occur for two reasons. First, the standard thickness of a tissue slide in pathology applications is $4 \mu\text{m}$, which usually exceeds the DOF.

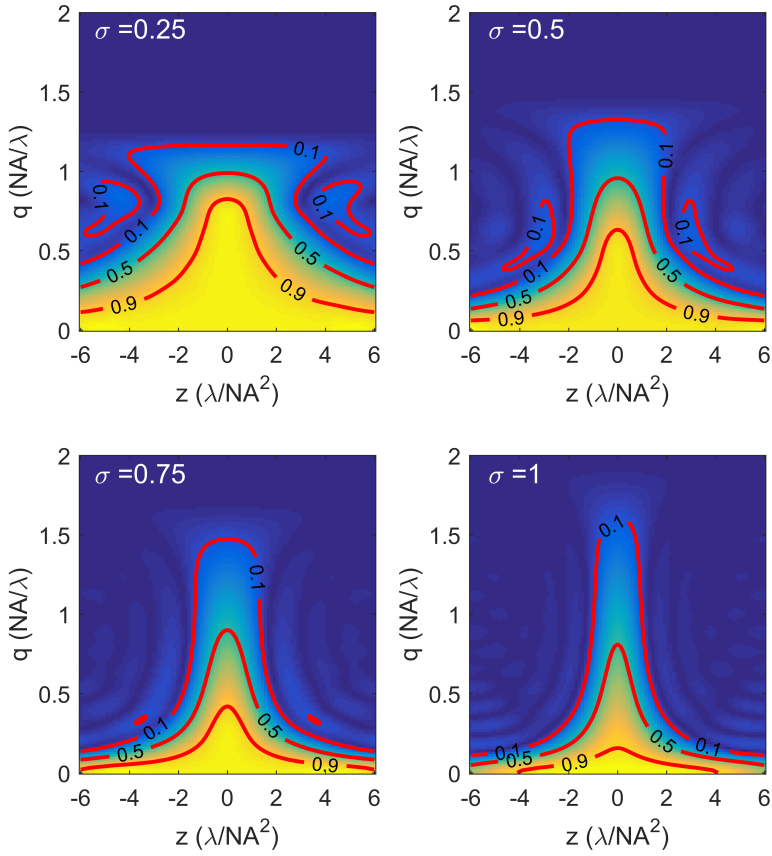


Figure 4.3: Numerically computed absolute value of the FT of the through-focus transfer function $|\hat{Q}(\vec{q})|$ for different values of the partial coherence factor σ .

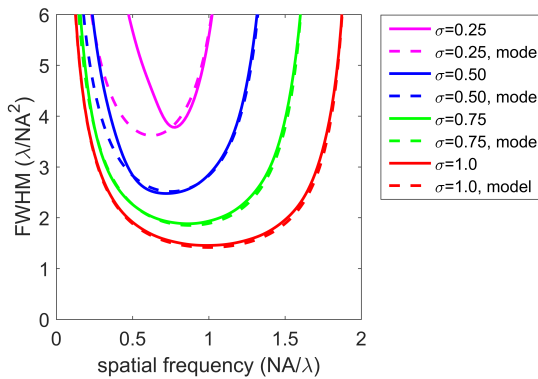


Figure 4.4: Numerically computed FWHM of the through-focus transfer function $|\hat{Q}(\vec{q})|$ as a function of the spatial frequency for different values of the partial coherence factor σ and the corresponding predictions of Eq. (4.27) with $\beta = \sqrt{2}$.

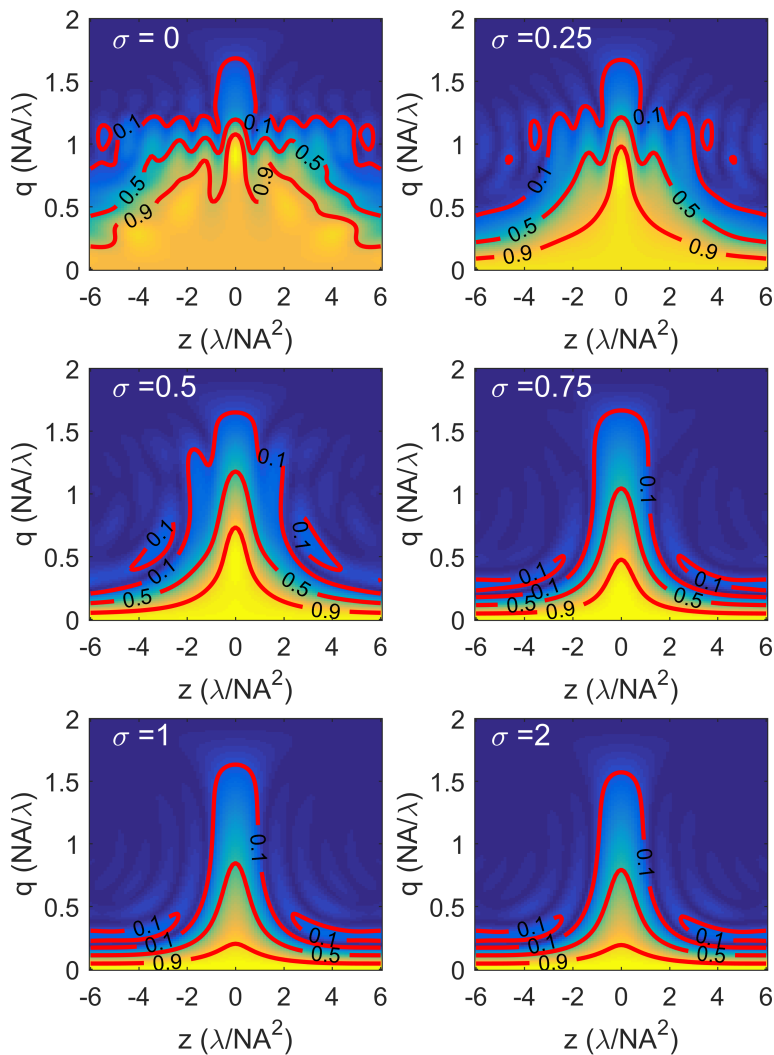


Figure 4.5: Numerically computed absolute value of the FT of the amplitude edge derived apparent MTF $|\hat{H}(\vec{q})|$ for different values of the partial coherence factor σ .

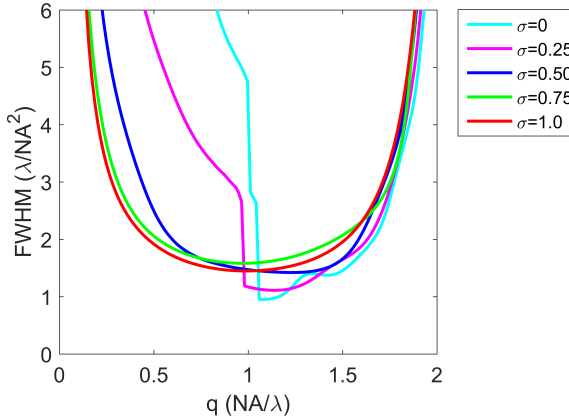


Figure 4.6: Numerically computed FWHM of the through-focus apparent transfer function derived from an amplitude edge $|\hat{H}(\vec{q})|$ as a function of the spatial frequency for different values of the partial coherence factor σ .

Second, there are topography variations in the tissue layer across the total area of the tissue slide. Usually, an autofocus system is employed to let the objective lens follow these topography variations, but there may be residual focus errors, especially close to folds in the tissue layer where there is a steep rise in the topography. For these reasons it is advantageous to have a large DOF, because then focus errors have less impact on overall image quality. For example, it may be required that spatial details in the tissue structure down to about $2\ \mu\text{m}$ remain clearly visible across a focus range equal to twice the tissue thickness of $4\ \mu\text{m}$ (in order to be robust against topography variations and focus errors). Taking $\lambda = 0.56\ \mu\text{m}$, $\text{NA} = 0.75$ and $n = 1.5$ this corresponds to a spatial frequency of about $0.37\text{NA}/\lambda$ and a defocus range of $\pm 2.99\lambda/2 \left(n - \sqrt{n^2 - \text{NA}^2} \right)$. From Eq. (4.30) it may then be inferred that the upper limit for σ should be in the range 0.65-0.70, somewhat smaller than typically used in microscopy.

4.2.4. ABERRATION ESTIMATION

Partial coherence also poses a challenge for extracting the primary aberrations from the through-focus apparent OTF derived from the step response, as proposed in our previous work [16]. In that work we described a method to measure coma from the maximum and minimum value of a third order polynomial fitted through the PTF. For σ values close to one or exceeding one it appears the apparent PTF in the aberration free case is more or less linear, pointing to an apparent shift in the edge position. It follows that this does not affect the estimation of coma. Figure 4.2 shows that for σ values considerably below one this is no longer the case.

Figure 4.7 shows the in-focus apparent PTF in case of $72\ \text{m}\lambda$ root mean square (rms) coma for different values of the partial coherence factor σ and the coma estimated from these PTF-curves. The linear term in the PTF as a function of spatial frequency is calibrated by requiring the PTF to be zero at $q = \text{NA}/2\lambda$, which determines the apparent edge shift. It appears that the procedure cannot be reliably used for $\sigma < 0.5$, as the PTF

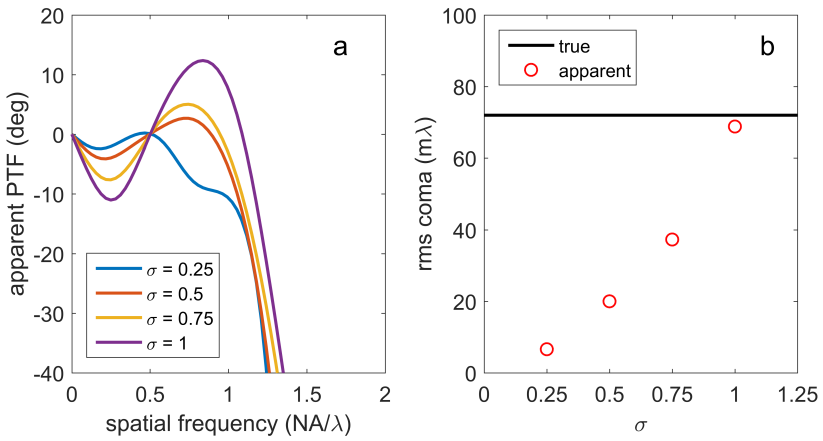


Figure 4.7: (a) Simulated PTF with 72 mλ rms coma for different values of the partial coherence factor σ values as a function of the spatial frequency. (b) The estimated coma based on the method of Ref. [16] as a function of σ .

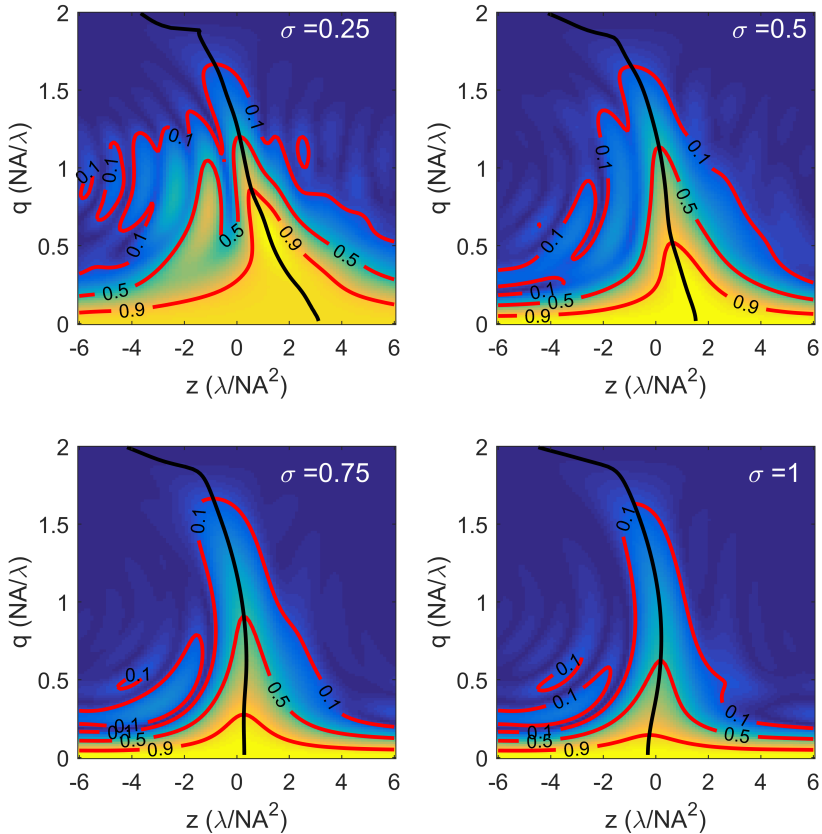


Figure 4.8: Simulated through-focus apparent MTF for 72 mλ rms spherical aberration and the best focus curves for different values of the partial coherence factor σ .

curve can then have multiple local maxima/minima. For values $0.5 < \sigma < 1$ the procedure results in an underestimation of the true coma with errors up to a factor of 3. Clearly, depending on the value of σ the conversion factor between the coefficient of the third order polynomial that describes the PTF and the amount of coma must be adapted.

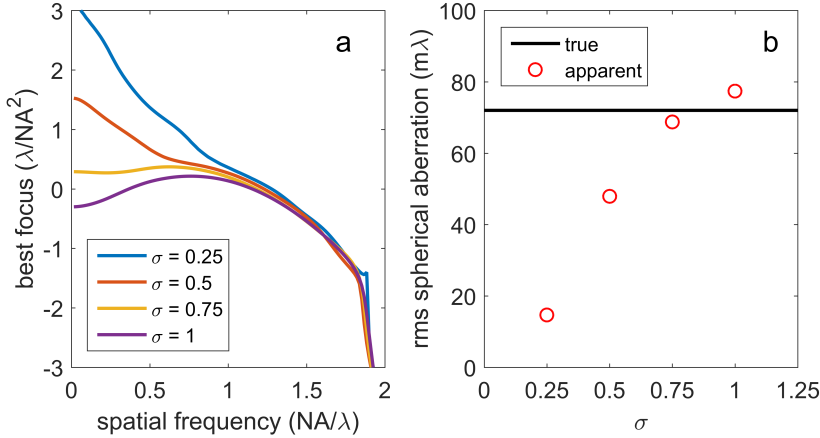


Figure 4.9: (a) Best focus as a function of spatial frequency for $72m\lambda$ rms spherical aberration. (b) Apparent spherical aberration estimated from the curvature of the best focus lines in (a).

Spherical aberration deforms and bends the through-focus MTF pattern towards one focus side [16] resulting in a parabolic shape for the best focus line (which is defined as the maximum in the MTF as a function of defocus for each spatial frequency). The curvature of the best focus line appears to be a measure for spherical aberration [16]. Figure 4.8 shows a simulated through-focus apparent MTF in the presence of $72m\lambda$ rms spherical aberration. The best focus lines and the estimated spherical aberration according to the curvature of the best focus line for the different σ are plotted in Fig. 4.9. It can be seen that the curvature of the parabolic shape of the best focus curve decreases with decreasing σ , leading to an underestimation of the spherical aberration when the method of Ref. [16] is used. For small σ , typically for $\sigma < 0.5$, the best focus curve is even better approximated with a linear curve than a parabolic curve. So, similar to the case for coma, we may infer that the aberration estimation is unreliable for $\sigma < 0.5$ and the conversion factor between the parabolic curvature of the best focus line and the amount of spherical aberration must be adapted to the value of σ in the range $0.5 < \sigma < 1$.

4.3. EXPERIMENT

4.3.1. SCANNER WITH COMPACT FLAT-FIELD KÖHLER ILLUMINATION UNIT

The experimental setup in use for whole slide imaging setup has been described in detail elsewhere [16]. Briefly, slides are imaged with a Nikon 20X/NA0.75 Plan Apochromat objective lens and a double back-to-back achromat tube lens (two Thorlabs AC508-500-A, 500 mm focal length). The image data is captured using a Dalsa Piranha HS-40-04k40 TDI line scan sensor (4096 pixels, pixel size $7\ \mu\text{m} \times 7\ \mu\text{m}$, maximum frame rate 36 kHz) using pushbroom scanning. The apparent through-focus OTF is derived from the am-

plitude edge response of a custom-built resolution target that is imaged through-focus with $0.2 \mu\text{m}$ steps [16]. The resolution target consists of edges parallel and perpendicular to the scan direction. As the line sensor that scans the object is perpendicular to the scan direction the edges parallel to the scan direction are tangentially oriented w.r.t. the position in the Field Of View (FOV) of the objective lens and the edges perpendicular to the scan direction are sagittally oriented in the FOV of the objective lens. Both types of edges therefore give rise to an apparent OTF for two mutually perpendicular cross-sections of the pupil plane (the q_x and q_y directions). Both edges are measured for three positions in the FOV of the objective lens ($x \pm 0.5 \text{ mm}$ and $x = 0 \text{ mm}$ field position).

We have developed an illumination unit with the capacity to individually address the three primary colors red, green and blue. This can be used to test chromatic aberration effects with a single camera and eventually to make color sequential scanning possible. Figure 4.10(a-b) show the realized illumination unit. It consists of three white LEDs selected from the Philips Luxeon Rebel series: cool white PWC1-0120, neutral white PWN1-0100, and warm white PWW1-0060 which are labeled as LED1, LED2, and LED3 respectively. Each LED has a 12 degree parabolic diffuse collimator (185-Polymer optics). A pair of dichroic filters from the Semrock catalog, FF495 (dichroic 1) and FF593 (dichroic 2), are used to divide the broad input light spectrum into the required red, green and blue bands. A photodiode sensor (PDA36A, Thorlabs), not drawn in Fig. 4.10b, monitors the light output of the LEDs. This photosensor is needed to guarantee a stable output with variable temperature and drift and to adjust relative intensities for maintaining color fidelity in a final RGB image generated with this illumination unit. Each LED is controlled by one general purpose laser diode driver (WLD-3343, Wavelength Electronics). It can modulate the LED current (maximum amplitude 3A) through an input voltage signal with a bandwidth limit of 2 MHz for a continuous sinusoidal signal, or 1 MHz for a square pulse train. A small mechanical mount for each LED-collimator assembly with 5 degrees of freedom alignment ($x\gamma z\alpha\beta$) was constructed in order to align the beam profile of each LED at the entrance aperture of the condenser.

The collimated LED beams pass a circular top hat diffuser (ED1-C20, Thorlabs) with an engineered surface that provides a uniform angular distribution of the scattered light with a 20 degree scatter angle. As the top hat diffuser is placed at the back focal plane of the condenser this will result in a flat illumination field at the front focal plane with an inherent field stop with a diameter of 17 mm defined by the maximum scattering angle of the top-hat diffuser and the condenser focal length. The spectrum measured with an optical spectral analyzer (AQ-6315, Yokogawa) is shown in Fig. 4.10c. The three channels appear to cover and divide the entire visible spectrum in a reasonably acceptable way. The line profiles of the illumination beam at the targeted sample plane are shown in Fig. 4.10d-e. The illumination intensity across the imaged FOV (with diameter of about 1 mm) has good uniformity (variations typically below 10%) because of the top-hat diffuser.

The condenser is a triplet design of ordinary CVI-MellesGriot catalogue BK7 plano-spheres, one $f=15\text{mm}/D=12.5\text{mm}$ lens and two $f=37.5\text{mm}/D=25.0\text{mm}$ lenses, producing a condenser with $\text{NA} = 0.75$ and an overall focal length $F = 10 \text{ mm}$. ZEMAX ray tracing simulations are shown in Fig. 4.10f. This condenser design provides sufficient alignment margins and opportunities for creating a uniform intensity in the FOV and for provid-

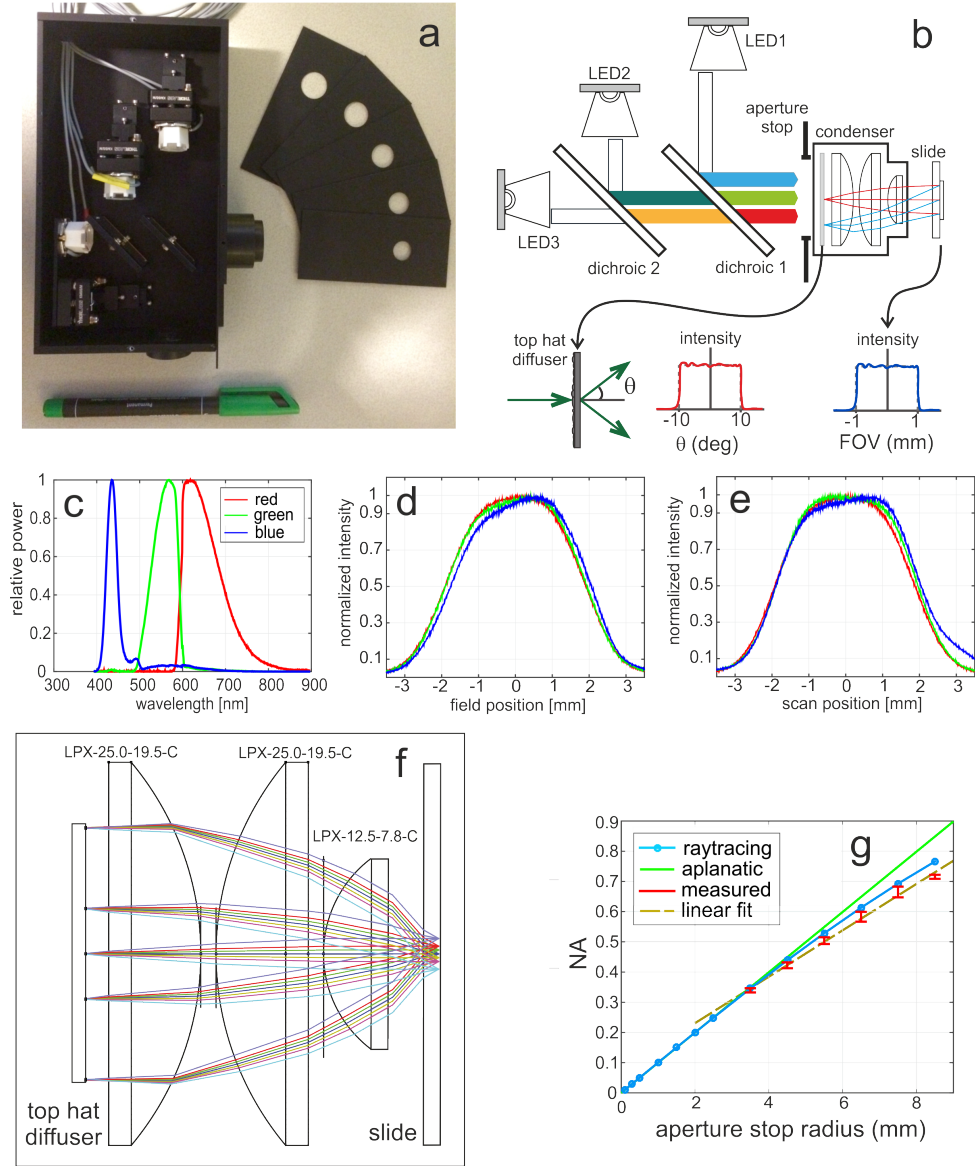


Figure 4.10: (a) Photo of the realized illumination unit with variable aperture stop size. (b) Schematic layout of the three-color LED-based illumination unit. The top hat diffuser scatters incident light uniformly within the angular range of (-10 deg, 10 deg). This results in a flat and spatially confined light distribution across the FOV. (d) Measured illumination box output light spectrum for red, green and blue color channels. (e-f) Measured condenser light profile along the field and scan direction, showing less than typically 10% intensity variation across the 1 mm diameter FOV. (g) Ray tracing picture of the triplet condenser design, rays are color coded for position in the FOV. (h) Condenser NA as a function of aperture stop radius, showing small deviations from aplanaticity.

ing Köhler-illumination to a good degree. Placing an aperture stop at the entrance pupil allows for precise tuning of the partial coherence factor σ . The condenser NA for the complete set of apertures used was determined from a calibration measurement. For a set of apertures the condenser NA was measured by placing a pinhole at the focal plane of the condenser and a paper screen at a given distance d from the pinhole. The image of the projected circle on the screen is captured by a camera, which is used to calculate the radius a . The condenser NA then follows as $\sin(\theta) = a / \sqrt{a^2 + d^2}$. For each aperture stop, the displayed NA data point is the average value of estimations for different distances d . The measurement results are shown in Fig. 4.10g along with the corresponding NA values from a ZEMAX ray tracing simulation. The variation of the condenser NA with aperture stop radius R for an ideal condenser follows from the Abbe sine condition [3]. According to this condition the ratio of the off-axis object height (here the aperture radius R) to the sine of the angle of the rays in image space (here the condenser NA) must be constant to have the optical system free of aberrations (coma) to first order in the field coordinates. This ratio is the effective focal length of the condenser. This implies a linear relation $\text{NA} = R/F$, with R the aperture radius and F the condenser focal length. It appears that the estimated NA from the ray tracing simulation deviates from the aplanatic line, which possibly indicates inherent spherical aberration in the condenser design. The deviation in the measured NA is even a bit larger. This can possibly be due to misalignment induced spherical aberration in the experimentally realized condenser. The calibration data can be reasonably fitted with a straight line $0.077 + R/(13.0\text{mm})$. This linear fit is subsequently used to assess the condenser NA for apertures used in the measurements of the through-focus apparent OTF. The aperture diameters equal to 4.0, 7.0, 8.5, 10.0, 11.5, 14.0, and 17.0 mm then result in partial coherence factors σ equal to 0.31, 0.46, 0.54, 0.62, 0.69, 0.82, 0.97, respectively.

4.3.2. EXPERIMENTAL RESULTS

A typical example of the measured edge response is shown in Fig. 4.11, which shows measured intensity profiles at the center of the FOV of the objective lens for tangentially oriented edges. It appears that the edge overshoot is typically below 10% for all σ values tested, a bit lower than expected from the simulations. The edge overshoot does vary with edge orientation, FOV position, and color, occasionally giving rise to higher values for the edge overshoot.

Figure 4.12 and 4.13 show the measured apparent MTFs and PTFs at the best focus for different values of σ for both tangentially and sagittally oriented edges for three positions in the FOV. Overall we observe an increase in the apparent MTF with decreasing σ for spatial frequencies below NA/λ , in agreement with theoretical expectations, but the flat plateau for spatial frequencies below $(1 - \sigma)\text{NA}/\lambda$ is in most cases not seen. The apparent PTF also increases in absolute value with decreasing σ , but only slightly. The apparent PTF is determined with the procedure outlined in Ref. [16], which effectively cancels the PTF term linear in spatial frequency (the apparent edge shift) described in the theory section. The residual PTF that depends non-linearly on spatial frequency appears to be somewhat smaller than expected from theory. It is noted that the overall edge response and edge overshoot, as well as the apparent MTF and PTF vary quite a bit with edge orientation and FOV position. This is indicative for field-dependent aberrations.

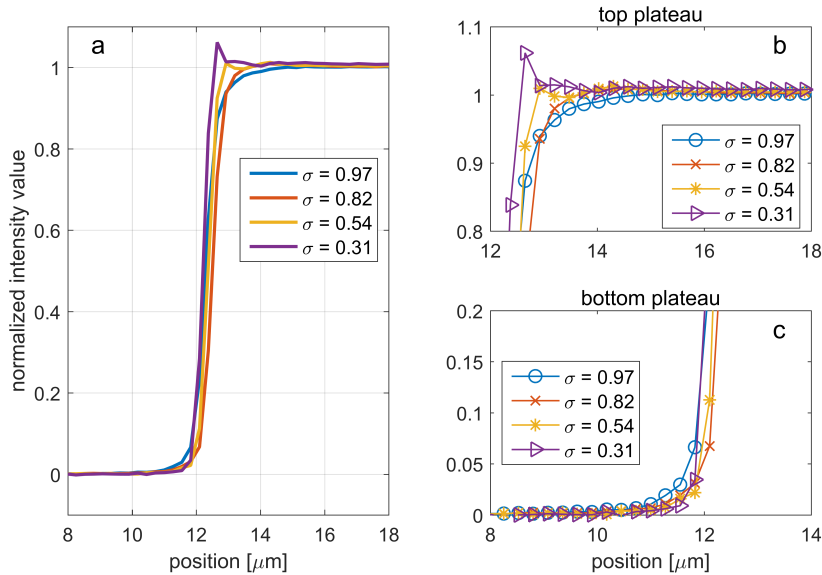


Figure 4.11: (a) Measured edge responses at the center of the FOV for tangentially oriented edges for different values of the partial coherence factor σ . (b-c) Insets of the top and bottom plateau, showing edge ringing for smaller σ .

Applying the estimation method of Ref. [16] to the PTF-data for $\sigma = 0.97$ results in rms tangential coma values that vary linearly with the field coordinate between $35 \pm 24 \text{ m}\lambda$ rms for the left position in the FOV to $-53 \pm 24 \text{ m}\lambda$ for the right position in the FOV. Sagittal coma is largely independent of the field position and takes a rms value equal to $-5 \pm 13 \text{ m}\lambda$. The dependence of these aberrations on the field coordinate is in good agreement with so-called Nodal Aberration Theory (NAT) [22], which describes the impact of misalignment on the field dependence of the primary aberrations following from basic optical theory [3].

The overall through-focus apparent MTF data for tangentially and sagittally oriented edges is shown in Fig. 4.14 and Fig. 4.15, respectively. The overall shape fits reasonably well with the expectations from theory and simulation. Differences may be attributed to aberrations. For example, the mild curvature of the best focus lines for $\sigma = 0.97$ and the small asymmetry between the apparent MTF above and below best focus indicates the presence of spherical aberration. Averaging the spherical aberration estimates for all recorded through-focus edges in the resolution target gives an estimate of $49 \pm 17 \text{ m}\lambda$ rms spherical aberration. The difference between the best focus curves for tangentially and sagittally oriented edges is indicative for astigmatism. It appears that the astigmatism is below $10 \text{ m}\lambda$ at the center of the FV and close to the diffraction limit at $\pm 0.5 \mu\text{m}$ in the FOV. This corresponds to a difference in best focus between sagittally and tangentially oriented edges of about $1.5 \mu\text{m}$. The overall dependence of astigmatism (and field curvature) on the field coordinate is well described by a quadratic function, in agreement with basic optical theory [3, 22].

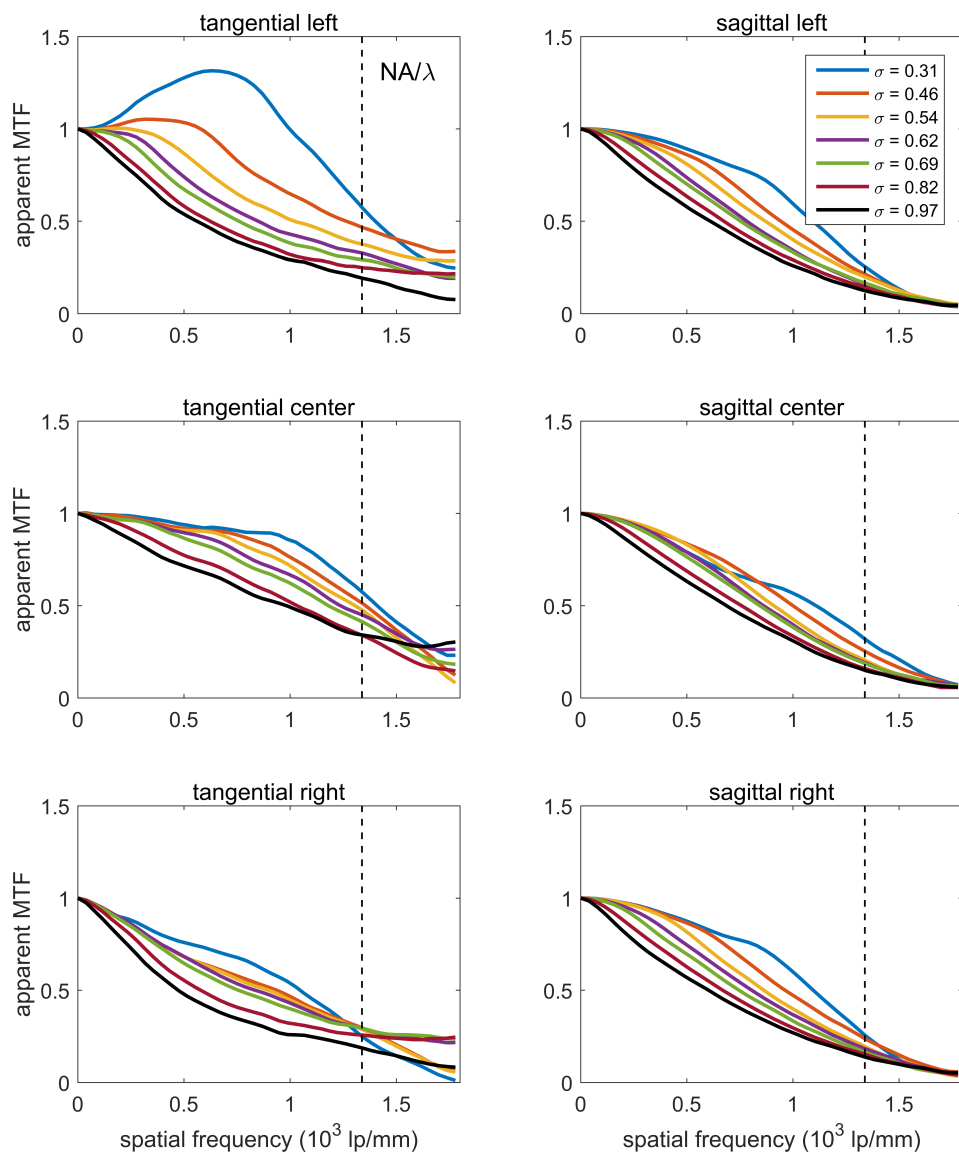


Figure 4.12: Measured in-focus apparent MTF curves for the green channel and for tangentially and sagittally oriented edges for the left (-0.5 mm), center and right (+0.5 mm) of the FOV for different values of the partial coherence factor σ . The dashed lines indicates the spatial frequency NA/λ .

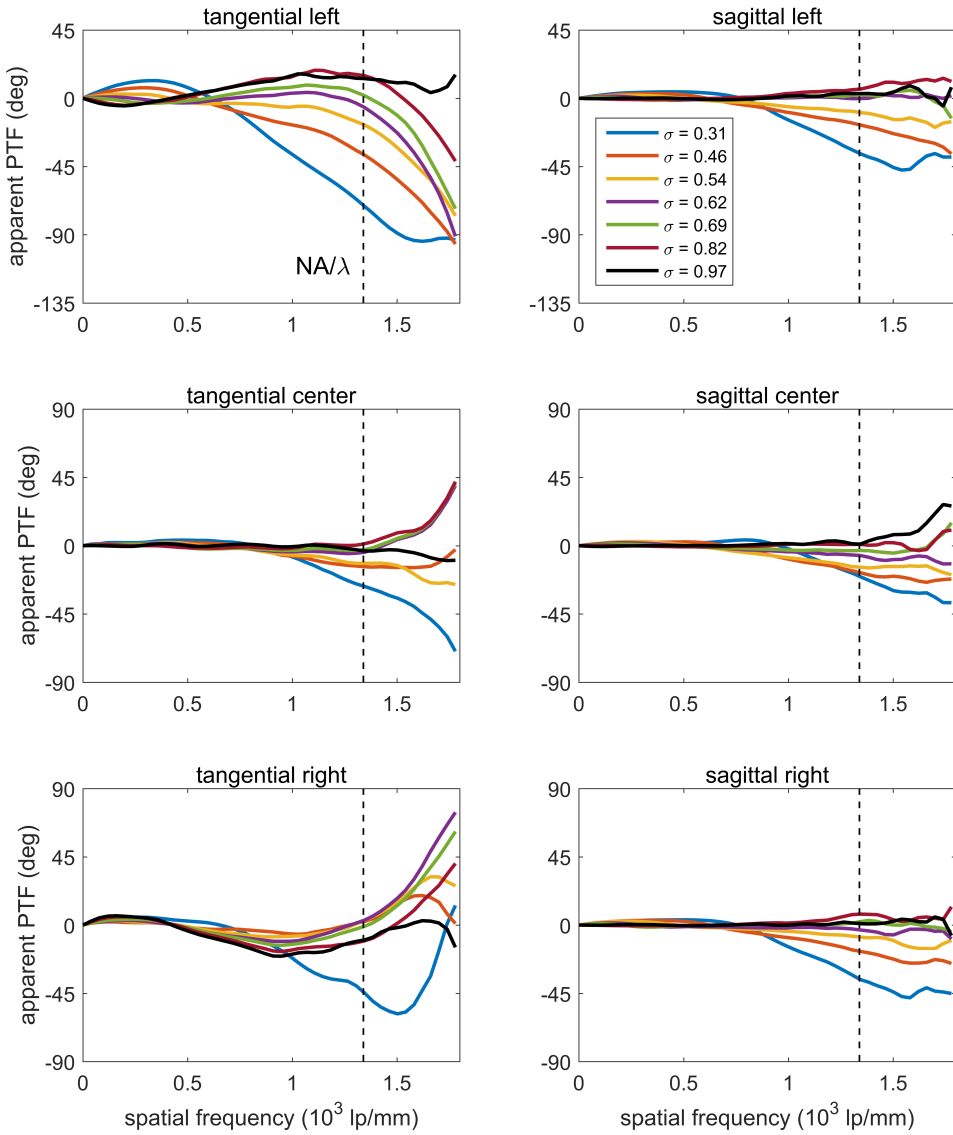


Figure 4.13: Measured in-focus apparent PTF curves for the green channel and for tangentially and sagittally oriented edges for the left (-0.5 mm), center and right (+0.5 mm) of the FOV for different values of the partial coherence factor σ . The dashed lines indicates the spatial frequency NA/λ .

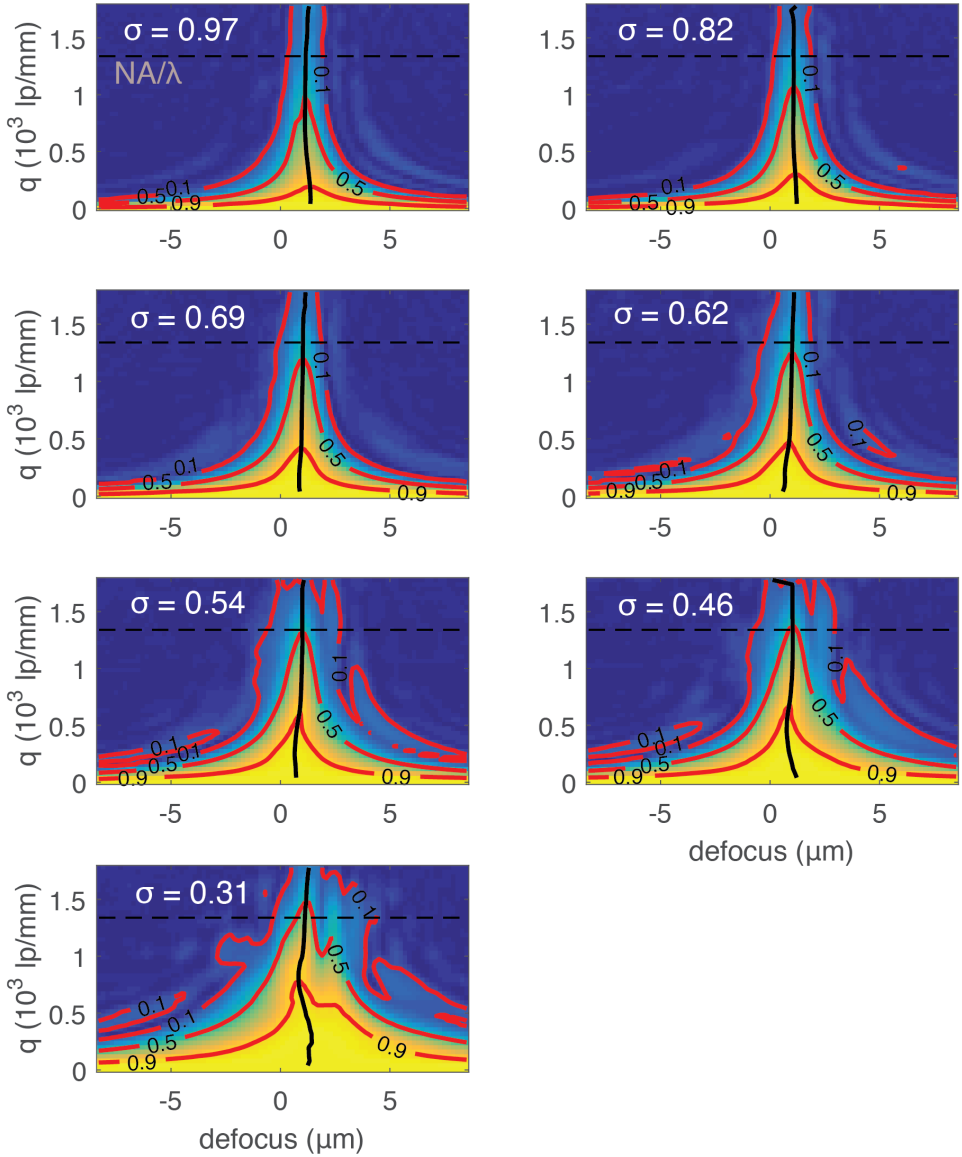


Figure 4.14: Measured through-focus apparent MTF curves for the green channel and for tangentially oriented edges in the center of the FOV for different values of the partial coherence factor σ . The dashed lines indicates the spatial frequency NA/λ .

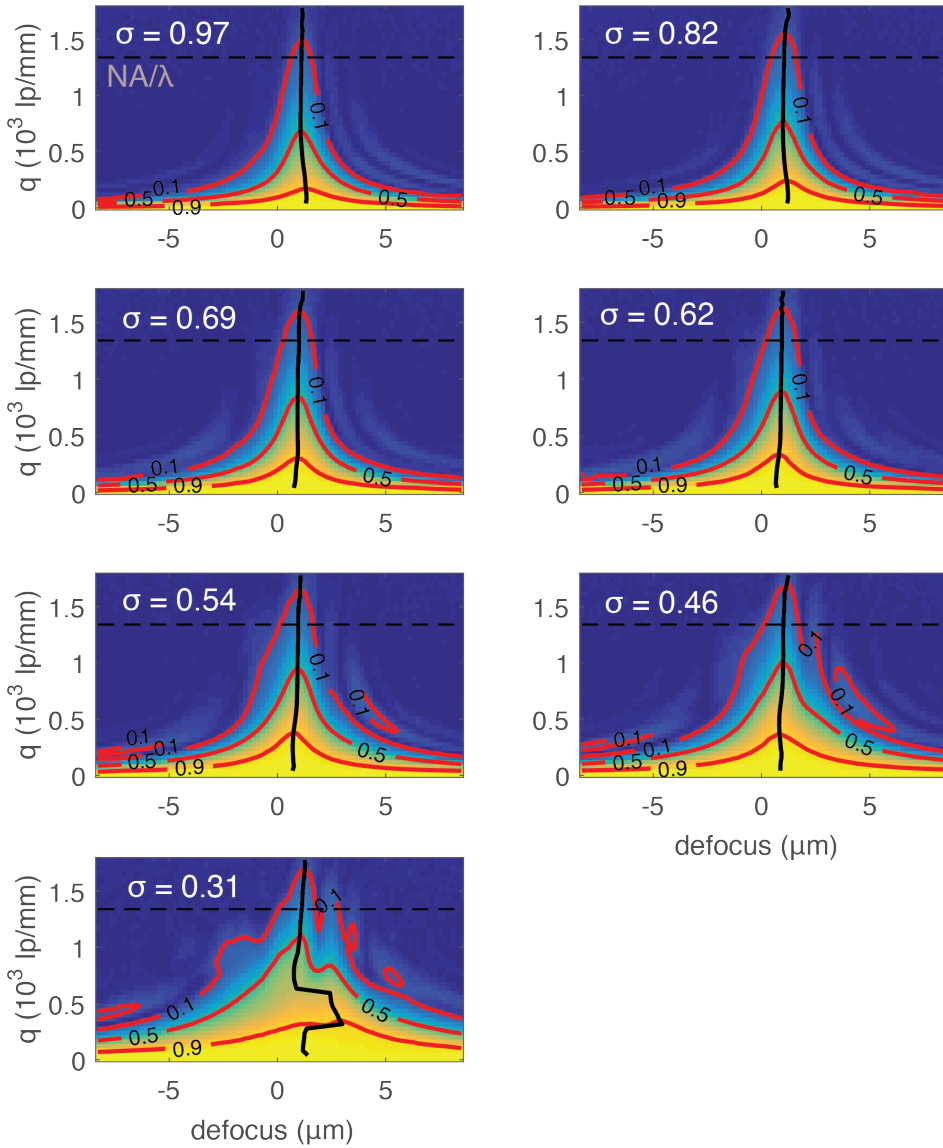


Figure 4.15: Measured through-focus apparent MTF curves for the green channel and for sagittally oriented edges in the center of the FOV for different values of the partial coherence factor σ . The dashed lines indicates the spatial frequency NA/λ .

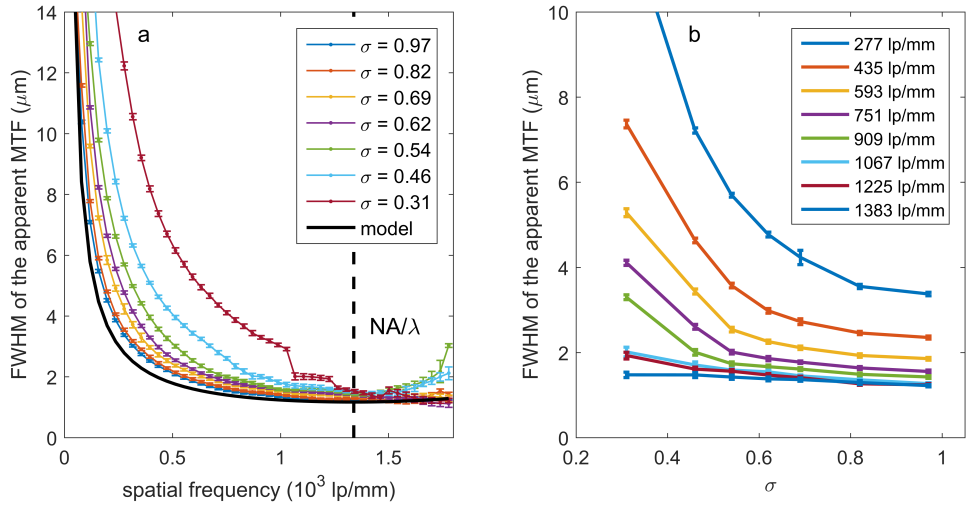


Figure 4.16: (a) FWHM of the apparent MTF (center of the FOV, green color channel) as a function of spatial frequency for different values of the partial coherence factor σ . The model curve is Eq. (4.30) for $\beta = \sqrt{2}$. (b) FWHM of the apparent MTF as a function of the partial coherence factor for different spatial frequencies.

The sensitivity to defocus in the experiment is also analyzed. Figure 4.16 shows the FWHM of the apparent MTF as a function of spatial frequency for different σ . The FWHM increases with decreasing spatial frequency (in the range below NA/λ) and with decreasing partial coherence factor, roughly in agreement with the simulation data shown in Fig. 4.6. The FWHM data for σ close to one appears to follow the theoretical prediction of Eq. (4.30) rather well. This is reasonable as for higher values of σ the apparent MTF closely resembles the modulus of the FT of the performance function. The increase of the FWHM with decreasing σ , however, is steeper than the typical $1/(1+\sigma)^2$ factor derived for the axial width of the FT of the performance function. Close to the spatial frequency NA/λ the FWHM for all σ values reach the same minimum value of about $\lambda/\sqrt{2}/(1-\sqrt{1-\text{NA}^2})$.

4.4. DISCUSSION

We have presented results concerning the effect of partial coherence on edge contrast, edge overshoot, and tolerance for defocus via a study of the through-focus apparent OTF derived from the response of the imaging system to amplitude edges. The analytical, numerical and experimental data agree reasonably well, where the deviations of the experiment from theory and simulation is attributed to aberrations.

There are several shortcomings to our experimental analysis. First of all, the measured edge response is somewhat undersampled, which makes the apparent OTF for the aliased higher spatial frequencies unreliable and which complicates the quantitative assessment of edge overshoot. In future studies it may be advisable to implement the slanted edge approach in measuring the apparent OTF [23, 24]. The second aspect concerns the experimental assessment of the mutual intensity. Although the back aperture

of the condenser is well filled and the condenser NA is determined from an experimental calibration, we have not actually measured the distribution of illumination light over the different illumination angles, let alone quantitatively measured the correlation between the light field at different positions in the illuminated FOV. So, the use of the mutual intensity following from Eq. (4.3) described by a single experimentally determined parameter σ may be too idealized.

Several factors have to be taken into account in order to determine the optimum value for σ for the application in WSI systems for digital pathology. A larger value of σ is beneficial for lateral resolution and edge ringing, whereas a smaller value of σ is beneficial for the edge contrast and DOF. It is questionable whether sufficient signal-to-noise ratio can be achieved for the very highest spatial frequencies in the range $(1.75 - 2) \text{NA}/\lambda$, corresponding to spatial details in the range $(0.37 - 0.42) \mu\text{m}$ for $\lambda = 0.56 \mu\text{m}$ and $\text{NA} = 0.75$. This implies that σ values above 0.75 hardly have an impact on the practical lateral resolution, even though the theoretical limit increases as $(1 + \sigma) \text{NA}/\lambda$. On the other hand, the edge contrast, which is correlated to the transfer for lower spatial frequencies, typically up to NA/λ (spatial detail down to $0.75 \mu\text{m}$), improves when σ is decreased to even lower values than 0.75 (see Fig. 4.12). The DOF also improves for this lower range of spatial frequencies. The DOF quantified by the FWHM of the through-focus apparent MTF (see Fig. 4.16) improves by 20 to 60%, depending on spatial frequency, when σ is lowered from 0.75 to 0.5. It appears that the FWHM of the apparent through-focus MTF is about equal to the typical tissue thickness of $4 \mu\text{m}$ for spatial details on the order of $2 \mu\text{m}$ when σ is decreased to about 0.5 for the set of imaging parameters used in the experiments. The major drawback of this further lowering of σ is the increase in edge ringing. The edge overshoot percentage used to quantify edge ringing is below 10% in simulation when $\sigma > 0.55$, and even a bit lower in the actual experiment. Taking all these factors into account it seems a reasonable assessment that the optimum value of the partial coherence factor σ is in the range 0.55-0.75. Although the research methods differ, this is substantially the same result as found by Ren et al. [15].

The current analysis has focused exclusively on circular apertures. An extension to different illumination apertures, in particular annular apertures and other variants of off-axis illumination, may have relevance to applications using such apertures. Starting point in that direction may be the work of Watanabe, who has analyzed the effects of partial coherence on DOF for an illumination system with one on-axis beam and two off-axis beams [25]. An entirely different generalization of the treatment described in this paper is towards other object types than edge objects. Point objects or periodic objects, for example, may lead to alternative approaches for measuring and monitoring optical image quality in the framework of a particular application. For any object $w(\vec{r})$ against a uniform background (object function $T(\vec{r}) = a + bw(\vec{r})$) the term in the image signal linear in $w(\vec{r})$ is in fact the real part of the convolution of the object function and the performance function $\text{Re}\{a^*bQ(\vec{r}) \otimes w(\vec{r})\}$. For a weak object ($|b| \ll |a|$) this convolution term contains all the relevant information on the object, making the performance function the weak object PSF and its FT the weak object OTF [19]. In that sense the FT of the performance function is the most relevant transfer function to assess the effects of partial coherence in general. An alternative may be found in the phase-space imaging kernel recently proposed in Ref. [26].

REFERENCES

- [1] H. H. Hopkins, *The concept of partial coherence in optics*, Proceedings of the Physical Society of London. Section A **208**, 263–277 (1951).
- [2] H. H. Hopkins, *On the diffraction theory of optical images*, Proceedings of the Physical Society of London. Section A, Mathematical and Physical Sciences **217**, 408–432 (1953).
- [3] M. Born and E. Wolf, *Principles of Optics* (Cambridge University, 1999).
- [4] R. Barakat, *Partially coherent imagery in the presence of aberrations*, Journal of Modern Optics **17**, 337–347 (1970).
- [5] C. P. Kirk, *Aberration effects in an optical measuring microscope*, Appl. Opt. **26**, 3417–24 (1987).
- [6] Y. Ichioka and T. Suzuki, *Image of a periodic complex object in an optical system under partially coherent illumination*, J. Opt. Soc. Am. **66**, 921–932 (1976).
- [7] R. Hild, G. Nitzsche, S. Kessler, and L. Leine, *Partially coherent defocused imaging of bar and periodic objects*, Journal of Modern Optics **34**, 555–567 (1987).
- [8] C. A. Mack, *Fundamental Principles of Optical Lithography: The Science of Microfabrication* (Wiley, 2011).
- [9] W. Singer, M. Totzeck, and H. Gross, *Handbook of Optical Systems, Physical Image Formation*, Vol. 2 (Wiley, 2006).
- [10] C. A. Mack, *Understanding focus effects in submicrometer optical lithography: a review*, Opt. Eng. **32**, 2350–2362 (1993).
- [11] M. o. de Beeck, et al., *Na/σ optimization strategies for an advanced DUV stepper applied to 0.25-μm and sub-0.25-μm critical levels*, Proc. SPIE 3051, 320–332 (1997).
- [12] C. A. Mack, *Focus effects in submicron optical lithography, part 4: metrics for depth of focus*, Proc. SPIE 2440, 458–471 (1995).
- [13] M. von Waldkirch, P. Lukowicz, and G. Tröster, *Effect of light coherence on depth of focus in head-mounted retinal projection displays*, Opt. Eng. **43**, 1552 (2004).
- [14] M. von Waldkirch, P. Lukowicz, and G. Tröster, *Multiple imaging technique for extending depth of focus in retinal displays*, Opt. Express **12**, 6350–6365 (2004).
- [15] L. Ren, et al., *The impact of the condenser on cytogenetic image quality in digital microscope system*, Analytical Cellular Pathology **36**, 45–59 (2013).
- [16] S. M. Shakeri, B. Hulsken, L. J. van Vliet, and S. Stallinga, *Optical quality assessment of whole slide imaging systems for digital pathology*, Opt. Express **23**, 1319–1336 (2015).

- [17] M. N. Wernick and G. M. Morris, *Effect of spatial coherence on knife-edge measurements of detector modulation transfer function*, Appl. Opt. **33**, 5906–13 (1994).
- [18] E. C. Kintner and R. M. Sillitto, *Edge-ringing in partially coherent imaging*, Journal of Modern Optics **24**, 591–605 (1977).
- [19] C. J. Sheppard, *Defocused transfer function for a partially coherent microscope and application to phase retrieval*, J. Opt. Soc. Am. A **21**, 828–31 (2004).
- [20] C. H. Righolt, et al., *Image filtering in structured illumination microscopy using the Lukosz bound*, Opt. Express **21**, 24431–51 (2013).
- [21] Y. Qiu, et al., *Impact of the optical depth of field on cytogenetic image quality*, J. Biomed. Opt. **17**, 96017–1 (2012).
- [22] S. M. Shakeri, B. Hulsken, L. J. van Vliet, and S. Stallinga, *Shack-Hartmann sensor based optical quality testing of whole slide imaging systems for digital pathology*, Proc. SPIE 9315, Design and Quality for Biomedical Technologies VIII , 931504 (2015).
- [23] S. E. Reichenbach, S. K. Park, and R. Narayanswamy, *Characterizing digital image acquisition devices*, Opt. Eng. **30**, 170–177 (1991).
- [24] K. Masaoka, T. Yamashita, Y. Nishida, and M. Sugawara, *Modified slanted-edge method and multidirectional modulation transfer function estimation*, Opt. Express **22**, 6040–6046 (2014).
- [25] H. Watanabe, *Analytical description of partially coherent optical systems for optimization of numerical aperture and degree of coherence*, Jpn. J. Appl. Phys. **33**, 6549–6556 (1994).
- [26] S. B. Mehta and C. J. Sheppard, *Equivalent of the point spread function for partially coherent imaging*, Optica **2**, 736–739 (2015).

APPENDIX

Here we present the asymptotic analysis for the imaginary part of the aberration free OTF for $\sigma \gg 1$. The TCC may generally be written as:

$$S\left(\frac{\vec{q}' + \vec{q}}{2}, \frac{\vec{q}' - \vec{q}}{2}\right) = \int d^2 q'' \hat{J}\left(\vec{q}'' - \frac{\vec{q}'}{2}\right) \hat{P}\left(\vec{q}'' + \frac{\vec{q}}{2}\right) \hat{P}\left(\vec{q}'' - \frac{\vec{q}}{2}\right)^* \quad (4.32)$$

Substituting in the expression for the transfer function $\hat{U}(q, 0)$ Eq. (4.16) gives:

$$\hat{U}(q, 0) = \frac{i}{\pi a^2} \int d^2 q'' R(\vec{q}'', q') \hat{P}\left(\vec{q}'' + \frac{q}{2} \hat{e}_x\right) \hat{P}\left(\vec{q}'' - \frac{q}{2} \hat{e}_x\right)^*, \quad (4.33)$$

with the weighting factor:

$$R(\vec{q}'', q') = a^2 P \int_{-\infty}^{+\infty} dq' \frac{q \hat{J}(\vec{q}'' - \frac{q'}{2} \hat{e}_x)}{q'^2 - q^2}, \quad (4.34)$$

where $a = \min(\sigma, 1)$. With $\vec{q}'' = (q_x, q_y)$ and Eq. (4.3) we find that:

$$\begin{aligned} R(\vec{q}'', q') &= \frac{1}{\pi} P \int_{2q_x - 2\sqrt{\tau^2 - q_y^2}}^{2q_x + 2\sqrt{\tau^2 - q_y^2}} dq' \frac{q}{q'^2 - q^2} \\ &= \frac{1}{2\pi} P \int_{2q_x - 2\sqrt{\tau^2 - q_y^2}}^{2q_x + 2\sqrt{\tau^2 - q_y^2}} dq' \left[\frac{1}{q' - q} - \frac{1}{q' + q} \right], \end{aligned} \quad (4.35)$$

where $\tau = \sigma NA/\lambda$. We may now use that:

$$P \int_a^b dx \frac{1}{x} = \log \left| \frac{b}{a} \right|, \quad (4.36)$$

to find:

$$\begin{aligned} R(\vec{q}'', q') &= \frac{1}{2\pi} \left[\log \left| \frac{q_x + \sqrt{\tau^2 - q_y^2} - q/2}{q_x - \sqrt{\tau^2 - q_y^2} - q/2} \right| \right. \\ &\quad \left. - \log \left| \frac{q_x + \sqrt{\tau^2 - q_y^2} + q/2}{q_x - \sqrt{\tau^2 - q_y^2} + q/2} \right| \right] \\ &= \frac{1}{2\pi} \log \left| \frac{q_x^2 + q_y^2 - \tau^2 - q^2/4 + q\sqrt{\tau^2 - q_y^2}}{q_x^2 + q_y^2 - \tau^2 - q^2/4 - q\sqrt{\tau^2 - q_y^2}} \right|, \end{aligned} \quad (4.37)$$

For $\sigma \gg 1$ we may approximate this factor as:

$$R(\vec{q}'', q') \approx \frac{1}{2\pi} \log \left| \frac{\tau - q}{\tau + q} \right| \approx -\frac{q}{\pi\tau}. \quad (4.38)$$

It then follows that:

$$\text{Im} \{ \hat{H}(q, 0) \} \approx -\frac{q}{\pi\tau} \text{Re} \{ \hat{H}(q, 0) \}, \quad (4.39)$$

giving as final result Eq. (4.20).

5

NOVEL 3D MULTISPECTRAL WHOLE SLIDE IMAGING PLATFORM FOR DIGITAL PATHOLOGY

In this chapter, we introduce a novel 3D multispectral Whole Slide Imaging (WSI) platform for application in digital pathology. This modular platform enables simultaneous multi-layer scanning of thick samples as well as auto-focus scanning of standard thin 4 μm thick tissue slides. It features a new custom-designed image sensor to provide 3D scanning and a compact LED-based Köhler illumination unit with five color channels for multispectral imaging. We achieve simultaneous scanning of 10 different focus levels with a speed of 5 k lines/s per color channel. An algorithm based on Principle Component Analysis (PCA) is used to suppress line-to-line noise arising from an error in design and manufacturing of the prototype sensor. We present a method to characterize the optical quality of the entire platform along with a discussion on alignment verification using Nodal Aberration Theory. We also show the ability of this platform to perform other microscopy modalities based on computational imaging approaches: multispectral imaging and defocus-based quantitative phase imaging. Our PCA-based multispectral image analysis shows promising result in removing/highlighting targeted stains in the scanned images provided that the combinations of stains have sufficiently low spectral overlap. Regarding the application to digital pathology, we image H&E stained prostate tissue slides with different specimen thicknesses and staining concentration using two different objective lenses, because a smaller objective NA turns out to be needed for thicker samples to reduce the sensitivity to spherical aberration. For specimen thicknesses up to 20 μm , we find that having a relatively low staining concentration can ensure that the 3D image stack has reasonable axial contrast. The results, however, for 60 μm and 100 μm thick tissue slides with further dilution in staining concentration show substantial axial crosstalk

S.M. Shakeri, L. van der Graaff, G.J.L.H. van Leenders, L.J. van Vliet, B. Hulsken, and S. Stallinga, manuscript in preparation.

between the different layers in the 3D image stack. This indicates the need for more subtle staining protocols and/or the use of novel tissue clearing techniques in sample preparation when these thick tissue slices are imaged.

5.1. INTRODUCTION

A Higher resolution and a larger field of view has always been an important concern in the design of optical systems. The use of an objective lens with a higher numerical aperture (NA) provides a higher resolution but at the same time decreases the field of view (FOV) of the optical system. This implies a trade-off between resolution and FOV. A number of methods have been proposed to overcome this limitation, e.g. multi-spot scanning with array illuminators [1], Fourier Ptychography [2–4] in which a series of low resolution images of a large FOV [5, 6] acquired with different illumination beam angles are combined to produce a single high-resolution image of the entire FOV. Although these methods do overcome the resolution-FOV trade-off, they do not optimally use the space-bandwidth-time product of the optical system [4] (basically corresponding to the throughput in Mpixels/s) as a fraction of the data stream is lost to overhead or carries redundant information. In addition, non-scanning approaches are still limited in FOV by the low magnification objective lenses used. Scanning systems optimally use the space-bandwidth-time product of the optical system and provides a truly unlimited FOV.

This approach has numerous benefits especially for the field of digital pathology. In a pathology lab, a high number of large area tissue slides needs to be digitized daily. So-called Whole Slide Imaging (WSI) systems enable scanning slides at high-resolution ($\sim 0.25 \mu\text{m}/\text{pixel}$) and high-throughput ($\sim 15 \times 15 \text{ mm}^2/\text{min}$). Among the possible scanning methods [7–9], the so-called “pushbroom” or line scanning method combines simplicity and speed by scanning the slide with a line sensor at a constant velocity. Currently, the majority of the WSI systems provide high quality two-dimensional (2D) images of tissue slides, mostly for brightfield microscopy with white light illumination [7]. Additionally, with the help of an autofocus mode, the WSI imaging optics tracks the topographic variations of the tissue layer and acquire an in-focus image of the entire slide. The benefits of WSI systems make them an attractive technology for primary diagnosis [10–12] as well as education [13–15] and research [16, 17] in digital pathology.

This technology, however, encounters limitations and challenges in design and application. The first challenge is the implementation of the autofocus mode, which is needed to guarantee high-quality in-focus 2D images. Autofocus is mostly implemented using image-based algorithms in which a stack of images at different focus level is examined to pinpoint the sharpest layer [18]. Most autofocus system designs use an additional camera and imaging optics synchronized with the main scanning engine to provide this volumetric information [19–21]. This increases the overall system complexity and requires synchronization between the autofocus and imaging branches. The second challenge is that the diagnosis in pathology is not limited to just examining one in-focus 2D image of a tissue slide. In some cases pathologists may need to scan through different focus levels to assess the three-dimensional (3D) morphology of tissues before making a final diagnosis [7, 22]. Additionally, in the field of cytology, it is important to study the cells in three dimensions [23]. The 3D functionality of current WSI systems is mostly realized through multiple scans at different focus levels to create a so-called “3D virtual

slide" [24–26]. This increases the scanning time and image file size considerably and consequently hampers its large-scale use. The third challenge is that the current bright-field WSI systems do not fully exploit the full potential of the available stains, including the increasing number of immunolabeling protocols. The standard three color channels (Red, Green, Blue) suffice for generating images that can be displayed on a computer screen [7]. This limits the possibilities of using multiple labels on a single tissue section. In particular the combination of conventional Haematoxylin and Eosin (H&E) staining and immunolabeling are hampered by the overlap of different chromogens in the three color channels. Currently, this problem is addressed by multiple staining and scanning passes with different stains. Such a sequential process is not only labor intensive, but it also requires cumbersome registration of the scanned images of the slides after each staining and scanning pass. Multispectral imaging could possibly enable the detection of multiple stains and labels from a single scan [27–29]. The fourth and last challenge is that the current scope of WSI systems is limited to samples that are labeled with absorption stains. Imaging unstained samples, however, would open up the prospect of establishing a non-invasive and label-free imaging platform in cell biology and pathology [30–32]. It is well-known that unstained cells and tissues are largely transparent, preventing the use of absorption contrast. Instead, the native variations in refractive index could be visualized using computational phase-contrast imaging techniques [31, 33]. Defocus-based phase-contrast imaging is easy to integrate into standard brightfield microscopes as it only requires a through-focus stack of intensity images [34–37].

Here, we present proof-of-principle experiments on and a characterization of a novel platform for WSI systems based on the line scanning method with a new custom-designed image sensor to lift the current limitations and tackle the aforementioned challenges. The concept of this WSI-platform and the design of the image sensor on which it is based originate from Philips and have been described in the patent literature [38–40]. Figure 5.1 shows a layout of the system. The new sensor contains separate sensorlets, which can be configured and read-out independently. Placing the sensor tilted (about 30°) to the optical axis corresponds to a tilted object plane covering an axial depth of ~20 μm. As a result, each sensorlet scans the tissue at a different focus level and a 3D image stack can be acquired in a single scan. A full color image with inherent color registration is acquired with a color-sequential illumination scheme based on fast switchable (100 kHz) LEDs. This configuration enables: 1) 3D imaging of tissue slides in one scan. Parallel scanning has the additional benefit that it uses the available illumination etendue more efficiently compared to scanning multiple focal layers sequentially. 2) 2D in-focus imaging by selecting the output of the sensorlet that is in focus, thus eliminating the need for an additional autofocus camera. 3) Multispectral imaging with up to five color channels with automatic color registration. 4) Defocused based phase-contrast imaging of unstained thin tissue layers in a single scan. The novel sensor also eliminates the need for multiple cameras for imaging and autofocusing (see Fig.5.1a), which reduces the components costs of a WSI system and simplifies its manufacturing and maintenance.

This chapter is structured as follows. First, we describe the 3D scanner architecture including the novel image sensor, the multispectral illumination unit, and the effect of finite conjugate imaging. Then we present an in-depth system characterization of the entire platform by measuring the gain and readout noise of the individual sensorlets,

quantifying the lowest order primary aberrations for each sensorlet, and by analyzing the measured full-field aberration maps assembled from the aberration data of the different sensorlets. We conclude the methods section by presenting a new denoising technique to suppress patterned noise such as line-to-line noise, a multispectral image analysis procedure, and quantitative phase imaging based on this new platform. In the results section, the outcomes of the system characterization are presented along with experimental 3D images of stained pathology slides of varying thickness (ranging from $4\ \mu\text{m}$ to $100\ \mu\text{m}$) and unstained cheek cells for phase-contrast imaging. Finally, the discussion section gives a brief summary and evaluation of the findings and our vision for the future of this highly modular WSI platform.

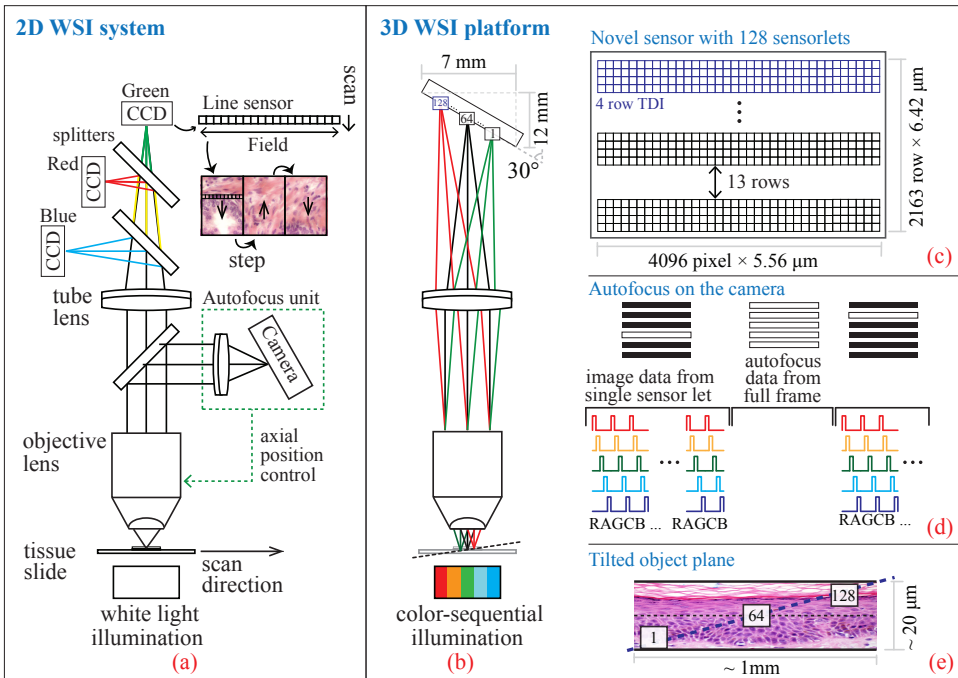


Figure 5.1: Schematic layout of our home-built WSI system. (a) 2D brightfield scanner with the possibility of adding an autofocus system. (b) Novel 3D multispectral WSI platform. It replaces the four cameras with a single custom-designed imaging sensor placed tilted in the scan direction of the image plane. The sensor is synchronized with a color-sequential illumination unit to provide multiple color channel images of a tissue slide. (c) A schematic overview of the pixel layout of the new sensor. It has 128 sensorlets of 4×4096 pixels placed under an angle of 30 deg in the image plane. (d) An autofocus strategy that can be implemented on the sensor to provide 2D in-focus images. A frame of line images from a set of sensorlets will be analyzed (white rectangles) and the sensorlet containing the sharpest image is selected for readout (a white rectangle among the black ones). (e) A projection of the sensorlets in the object plane. It covers about 1 mm of the field and a depth range of about $20\ \mu\text{m}$. Each sensorlet produces an image of one focus level of a tissue slide.

5.2. METHODS

5.2.1. 3D SCANNER ARCHITECTURE

We have built a 3D WSI platform (Fig. 5.1b) using a Nikon 20×/NA0.75 Plan apochromat VC, or a 10×/NA0.45 Plan Apochromat objective lens, a custom-designed tube lens by Nikon (effective back focal length of 222.4 ± 2.2 mm), a PI M-505 low profile translation stage (for positioning of the slide in the field direction), a Newport XM1000 ultra precision linear motor stage (for the scanning motion of the slide), a PI M-111 compact micro-translation stage (for coarse positioning of the objective lens in the axial direction), and a PI P-721.CL0 piezo nano-positioner (for fine positioning of the objective lens in the axial direction). The heart of the setup is a custom-designed CMOS imaging sensor [38–40], which comprises 128 sensorlets of 4×4096 pixels (Fig. 5.1c) separated from each other by 13 rows of pixels. The pixel size is $5.56 \mu\text{m}$ in the field direction and $6.42 \mu\text{m}$ in the scan direction. It covers a total area of about $23\text{mm} \times 12\text{mm}$ in the image plane. Each sensorlet has Time Delay Integration (TDI) functionality [41] over 4 lines of pixels for increasing the signal to noise ratio. The sensor is tilted over an angle of around 30 deg so that each line sensor (sensorlet) scans at a different focal depth. The sensor has two control engines, one at the top and one at the bottom (see Fig. 5.2). Both engines can read-out each sensorlet with a specific gain and offset. This flexibility enables the implementation of various scanning strategies. The first one is the autofocus of the 2D scanning strategy, which removes the need for additional optics and a camera in the 2D WSI architecture (Fig. 5.1d). At each scanning step, the sensorlet with the sharpest image is identified. This can be done by processing a full frame obtained from all the 128 sensorlets. Then the image data from the best focused sensorlet will be read out and stored. They form the next set of lines of the final image. This process is repeated until the entire slide is scanned. To perform full 3D scanning, the full set or a subset of the 128 sensorlets is selected and divided between the top and bottom engines. As the sample moves, both engines read out the images of the selected sensorlets independently.

Fig. 5.2 shows the electronic layout of our experimental setup. A development board (idFLEX modular platform, Aspect-System) is attached to the tilted sensor for streaming out image data. It has two sets of a reconfigurable module and a dual full Camera Link (CL) module for reading the image data of the sensor from the top and bottom control engines. The reconfigurable module has a field-programmable gate array (FPGA) integrated circuit (XC2VP20-FG676, Xilinx VirtexII pro), which is programmed for controlling the sensor and implementing scanning strategies. Each engine reads out the serialized image data on the sensor and prepares it for the corresponding dual full-CL module. Each full-CL stream has a maximum possible throughput of 680 MB/s. There are two computers in the setup, one for controlling the stages (PC1) and one for controlling the image sensor (PC2). The process of scanning begins at PC2 by sending a scan request through a network connection to PC1. Then PC1 initializes the stages and moves the sample in the scan direction. At each step, it sends a trigger signal to the development board. Then the development board turns the LEDs on sequentially and streams out the image data to four frame grabbers (microEnable IV AD4-CL, SiliconSoftware) in PC2. The sensor is designed to achieve a maximum 200 k lines/sec when scanning a single sensorlet. Each line consists of 4096 two-byte pixels which leads to a throughput of 1600 MB/s. The first prototype sensor cannot reach this designed maximum speed due to manufac-

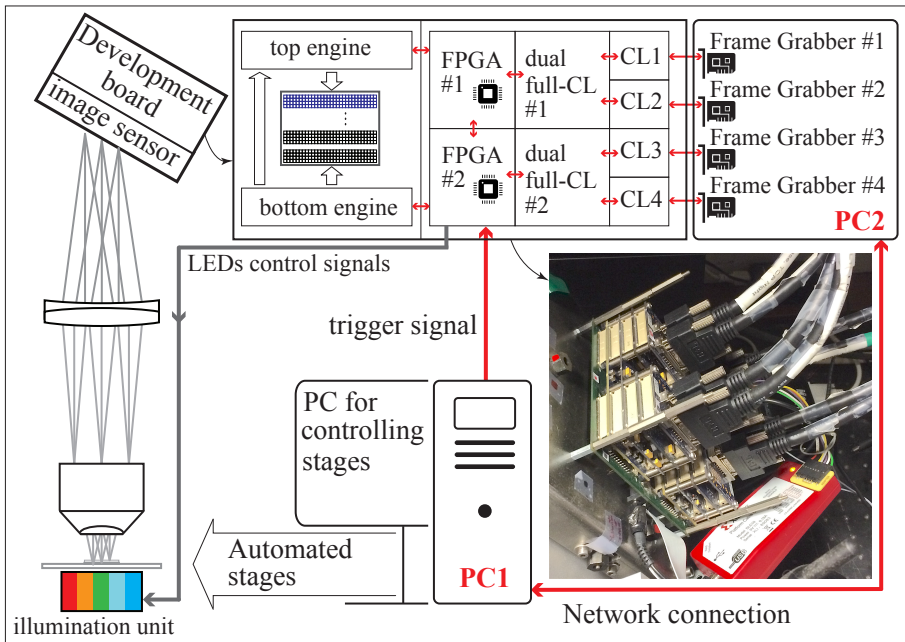


Figure 5.2: Schematic overview of the electronic layout of the experimental setup. Bottom right of the figure shows a photo of the new sensor attached to the development board to stream out image data via 8 camera link cables.

turing and design bugs, speed limitations on the development board electronics, and a memory limit on the computer with the acquisition software. It is anticipated that the sensor will reach the maximum speed after a redesign round. In the scanner that has been built in the lab, we can scan one focus level with five colors at a speed of 1 k lines/s. The speed for one color scanning is thus 5 k lines/s. The major cause of this low scanning speed is the necessarily long integration time for each color channel due to a limitation in adjusting the gain and offset of the AD-converter for each sensorlet. It has turned out that the offset must be set at a large number to prevent a zero output for each pixel and the gain must be set close to its maximum to have a reasonable image contrast. Therefore, in order to collect enough photons for each pixel both the illumination power and the integration time had to be increased. In the next design, these problems will be addressed and also new custom-built acquisition electronics will replace the development board.

ILLUMINATION

For the illumination we designed a multispectral LED-based unit and a condenser, matched in NA to the objective lens, for providing Köhler illumination. It offers five colors: red, amber, green, cyan, and blue with a maximum power at 627, 590, 530, 505, 447 nm wavelength respectively (selected from the Philips Luxeon Rebel color series). The corresponding spectral full width at half maximum values are 20, 20, 30, 30, and 20 nm, which provide sufficient spectral overlap to generate faithful color representations of tissue slides prepared with arbitrary absorption stains. Fig. 5.3 shows the schematic layout

of the box and the spectral power distribution of the LEDs. Each LED is mounted with 5 degrees of freedom adjustment (3 position, 2 angle) and the box has a compact size of $240\text{mm} \times 96\text{mm} \times 80\text{mm}$.

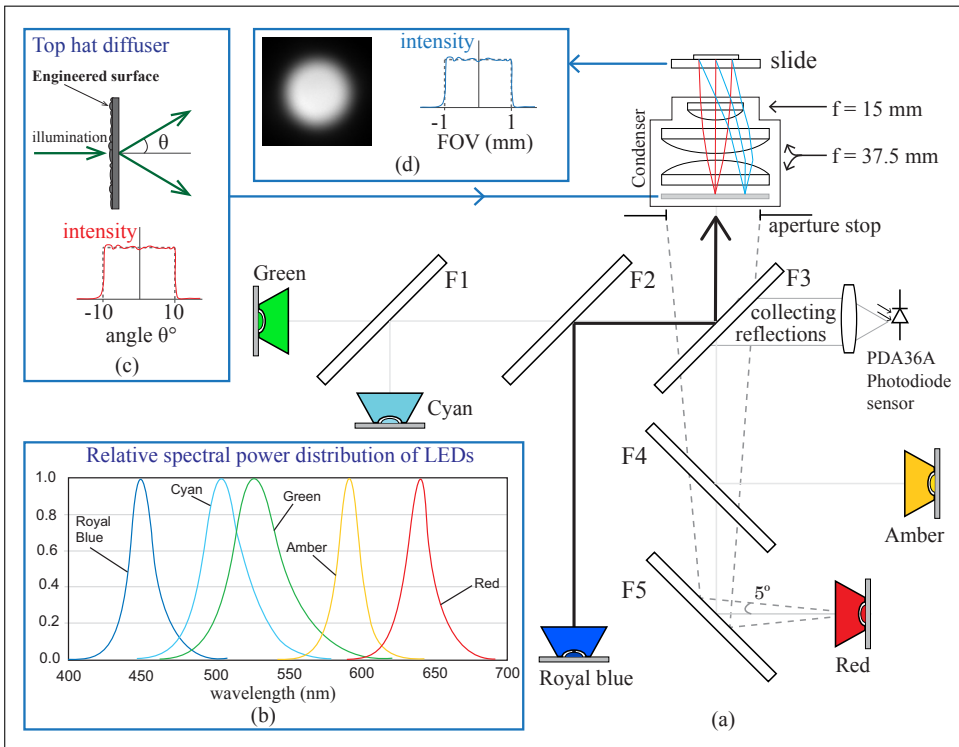


Figure 5.3: (a) Schematic layout of the LED-based multispectral illumination unit. The 5-color LEDs are selected from the Philips Luxeon Rebel series: LXML-PM01-0100 (Green), LXML-PE01-0070 (Cyan), LXML-PR02-A900 (Royal Blue), LXM2-PD01-0050 (Red) and LXML-PL01-0050 (Amber). The dichroic mirrors are from the Semrock catalog: FF518-Di01 (F1), FF484-FDi01 (F2), FF552-Di02 (F3), FF605-Di02 (F4), FF591-SDi01 (F5). (b) Relative spectral power distribution of the LEDs (from the manufacturer data sheet). (c) The top-hat diffuser scatters the incident light uniformly within an angular range of $(-10$ deg, 10 deg). (d) This results in a flat and spatially confined light distribution across the FOV.

The light emitted by the LEDs is collimated by 5 degree collimators (OPC1-1-SPOT, Dialight) and combined by a set of dichroic mirrors. A small part of the light is split off to a forward sense photodiode (PDA36A, Thorlabs) for monitoring and controlling the emitted intensity. The collimated LED beams pass a circular top-hat diffuser (ED1-C20, Thorlabs) with an engineered surface such that it provides a uniform angular distribution of the scattered light with a 20 degree scatter angle (Fig.5.3c). As the top-hat diffuser is placed at the back focal plane of the condenser this will result in a flat illumination field at the front focal plane with an inherent field stop with diameter of 17 mm defined by the maximum scattering angle of the top-hat diffuser and the condenser focal length. The condenser has an overall focal length $F=10$ mm and is made from two $F=25$ mm achromats (LPX-25.0-19.5, CVI Melles Griot) and one $F=12.5$ achromat (LPX-12.5-

7.8, CVI Melles Griot). Each LED is controlled by one general purpose laser diode driver (WLD-3343, Wavelength Electronics). It can modulate the LED current (maximum amplitude 3A) through an input voltage signal with a bandwidth limit of 2MHz for a continuous sinusoidal signal, or 1MHz for a square-wave pulse sequence. The limiting factor is the ability of the control electronics (here the development board) to generate the voltage signal for the driver. In principle, the FPGA modules on the development board could generate the 200 kHz pulse signal for the designed maximum line rate, which is in the bandwidth range of the LED drivers.

FINITE CONJUGATE IMAGING AND SPHERICAL ABERRATION

The matched set of objective and tube lens define a 4F telecentric aplanatic optical system. The telecentricity is maintained across the visible spectrum leading to a lateral color error that is less than half a pixel for all sensorlets. Axial color alignment, field curvature and astigmatism are also controlled by the matched lens design. Nevertheless, all but the central sensorlet are operated at finite conjugate, which necessarily entails that there is spherical aberration present (Fig. 5.4). The amount of spherical aberration can be estimated starting from the analysis of the aberration function for a 4F aplanatic system. It involves the effect of the three degrees of freedom, namely the axial object position Δz_{ob} , the objective working distance Δz_{fwd} and the axial image position Δz_{im} . All distances are relative to the nominal aberration-free case:

$$W(\rho) = \Delta z_{ob} \sqrt{n^2 - \rho^2 NA^2} + \Delta z_{fwd} \sqrt{1 - \rho^2 NA^2} - \Delta z_{im} \sqrt{1 - \rho^2 NA^2 / M^2}, \quad (5.1)$$

where ρ is the scaled radial pupil coordinate ($0 \leq \rho \leq 1$) so that the pupil is scaled to the unit circle, NA denotes the objective NA, $M = F_{tube}/F_{ob}$ is the lateral magnification, equal to the ratio of the tube focal length and the objective focal length, and n is the medium refractive index. This may be written in a compact form as:

$$W(\rho) = \sum_{j=1}^3 z_j f_j(\rho), \quad (5.2)$$

with $z_1 = \Delta z_{ob}$, $z_2 = \Delta z_{fwd}$, and $z_3 = \Delta z_{im}$, and:

$$f_1(\rho) = \sqrt{n^2 - \rho^2 NA^2}, \quad (5.3)$$

$$f_2(\rho) = \sqrt{1 - \rho^2 NA^2}, \quad (5.4)$$

$$f_3(\rho) = \frac{\rho^2 NA^2}{2M^2}, \quad (5.5)$$

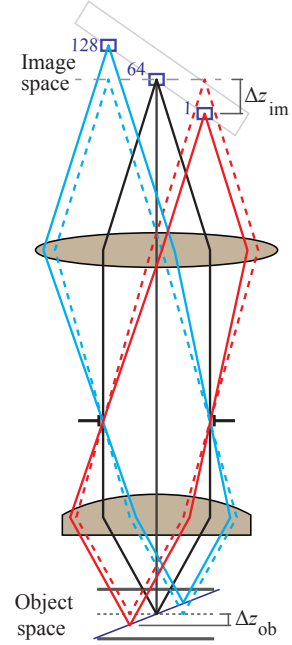


Figure 5.4: The effect of the axial position of the sensorlets on focus and conjugate.

where a Taylor approximation is used for the third aberration term based on $M \gg 1$ and neglecting a piston term. Given the axial position of the image sensor and the objective's working distance, the axial position of the object is found by minimizing the rms aberration function as a function of the axial object position, i.e. given z_2 and z_3 , z_1 is found by solving:

$$\frac{dW_{\text{rms}}}{dz_1} = 0. \quad (5.6)$$

The rms value of the aberration function is given by:

$$W_{\text{rms}}^2 = \sum_{j,l=1}^3 g_{jl} z_j z_l, \quad (5.7)$$

with:

$$g_{jl} = \langle f_j(\rho) f_l(\rho) \rangle - \langle f_j(\rho) \rangle \langle f_l(\rho) \rangle. \quad (5.8)$$

Here the angular brackets indicate averaging over the pupil (i.e. integration over the unit circle with radial coordinate ρ). These averages can be evaluated analytically using Mathematica and are given in [42]. Minimization of W_{rms}^2 with respect to z_1 is straightforward and leads to:

$$z_1 = -\frac{g_{12}}{g_{11}} z_2 - \frac{g_{13}}{g_{11}} z_3, \quad (5.9)$$

which directly gives the axial magnification as:

$$M_{\parallel} = -\frac{g_{11}}{g_{13}} = \chi \frac{M^2}{n}, \quad (5.10)$$

where χ is a non-paraxial correction factor depending on NA/n , which satisfies $\chi \rightarrow 1$ in the limit $\text{NA}/n \rightarrow 0$. The tilted image sensor spans a range of axial positions $z_c - d/2 \leq z_3 \leq z_c + d/2$ in image space, where d is the total axial range and z_c is the axial position of the middle sensorlet. In object space, this corresponds to the axial range $0 \leq z_1 \leq d/M_{\parallel}$, assuming that the upper focal slice is directly adjacent to the cover slip. This implies that the working distance of the objective must be set such that:

$$z_2 = -\frac{g_{13}}{g_{12}} \left(z_c - \frac{d}{2} \right). \quad (5.11)$$

Using the expressions we derived for the object axial position z_1 and the working distance z_2 we can write the rms value of the aberration function as a function of the axial image position z_3 . With some algebra it may be shown that:

$$\begin{aligned} W_{\text{rms}}^2 &= \left(g_{33} - \frac{g_{13}^2}{g_{11}} \right) z_3^2 + 2 \left(\frac{g_{13}^2}{g_{11}} - \frac{g_{23}g_{13}}{g_{12}} \right) \left(z_c - \frac{d}{2} \right) z_3 \\ &\quad + \left(\frac{g_{22}g_{13}^2}{g_{23}^2} - \frac{g_{13}^2}{g_{11}} \right) \left(z_c - \frac{d}{2} \right)^2. \end{aligned} \quad (5.12)$$

Clearly, the square of the rms value of the aberration function depends quadratically on the axial image position z_3 . The lowest overall value is obtained if the minimum of this

parabola is at $z_3 = z_c$. This condition can be used to find an expression for the optimum axial position for the middle sensorlet. This results in:

$$z_c = \frac{g_{13}^2/g_{11} - g_{23}g_{13}/g_{12}}{g_{33} - g_{23}g_{13}/g_{12}} \frac{d}{2}. \quad (5.13)$$

We may now write the square of the rms value of the aberration function as:

$$W_{\text{rms}}^2 = W_c^2 \left(\frac{d}{2M_{\parallel}} \right)^2 + (W_e^2 - W_c^2) \left(\frac{z_3 - z_c}{M_{\parallel}} \right)^2, \quad (5.14)$$

where the spherical aberration sensitivity at the center of the image sensor W_c and at the edge of the image sensor W_e are given by:

$$W_c^2 = M_{\parallel}^2 \left[\frac{g_{22}g_{13}^2}{g_{23}^2} - \frac{g_{13}^2}{g_{11}} - \frac{(g_{13}^2/g_{11} - g_{23}g_{13}/g_{12})^2}{g_{33} - g_{13}^2/g_{11}} \right] \left[\frac{g_{33} - g_{13}^2/g_{11}}{g_{33} - g_{23}g_{13}/g_{12}} \right]^2 \quad (5.15)$$

$$W_e^2 = M_{\parallel}^2 \left[g_{33} - \frac{g_{13}^2}{g_{11}} \right] + W_c^2,$$

By using a Nikon 20×/NA0.75, the lateral magnification is $M = 22.2$. This gives a pixel size in object space equal to $0.25 \mu\text{m}$ for a pixel size in image space equal to $5.56 \mu\text{m}$. For a medium refractive index $n = 1.5$ and the objective NA = 0.75 it is found that $\chi = 1.07$ and the axial magnification is $M_{\parallel} = 352$. The image sensor size in the direction perpendicular to the line sensors is $127 \times 17 \times 6.42 \mu\text{m} = 13.9 \text{ mm}$. With a tilt angle $\beta = 30 \text{ deg}$ the axial range in image space is $d = 8.0 \text{ mm}$ and the axial range in object space is $d/M_{\parallel} = 19.7 \mu\text{m}$.

For the given numbers we find that the optimum axial position of the middle sensorlet is $z_c = 0.32d$, giving an axial range in image space of $-0.18d \leq z_c \leq 0.82d$. The reason for the significant asymmetry is the use of finite conjugate compensation of the spherical aberration arising from focusing into the tissue layer below the cover slip. The spherical aberration for the middle sensorlet is only $1.4 \text{ m}\lambda$ for a green wavelength of $\lambda = 0.5 \mu\text{m}$, composed mainly of higher order spherical aberration, and $21 \text{ m}\lambda$ for the sensorlets at the edge of the chip. In case the axial position of the middle sensor is not chosen optimally, the spherical aberration varies in an unsymmetrical way from the first sensorlet to the last sensorlet. For $z_c = 0$ we find a spherical aberration of $35 \text{ m}\lambda$ for the worst-case sensorlet at one edge of the chip.

For a 10×/NA0.45 objective we find different numbers. Now $M = 11.1$ giving a pixel size in object space equal to $0.50 \mu\text{m}$, $\chi = 1.02$ and an axial magnification of $M_{\parallel} = 84.1$. The axial range in object space is now $d/M_{\parallel} = 82.4 \mu\text{m}$. The spherical aberration at the middle sensorlet is only $0.2 \text{ m}\lambda$ and around $10 \text{ m}\lambda$ for sensorlet at the edge of the sensor.

5.2.2. SYSTEM CHARACTERIZATION

Characterization of the entire system comprises both the sensor and the optics. The first aspect is the measurement of the gain, offset and readout noise of the sensorlets. Then we focus on assessing the optical quality underneath each sensorlet by extracting the primary aberrations by analyzing a complete through-focus stack of images [43].

Combining the results for each sensorlet will then result in a full-field aberration map for each of the primary aberrations that are estimated. Finally, the analysis of these full-field aberration maps with Nodal Aberration Theory enables an assessment of the alignment quality [44].

GAIN AND READOUT NOISE

The first step in characterizing the system is to determine the gain, offset and readout noise of the sensor. Each sensorlet suffers from shot noise and readout noise. Shot noise obeys Poisson statistics and as a consequence the detected photons are Poisson distributed. The readout noise is independent of the signal and can be modeled as additive zero-mean Gaussian noise. This results in a pixel variance over repeated acquisitions given by [45, 46]:

$$\text{var}(I) = G(\bar{I} - c) + \sigma^2 \quad (5.16)$$

where I is the pixel signal in ADU, c is the image offset, G is the gain of the camera in photons per ADU (Analog-to-Digital Unit), σ is the RMS of the readout noise, and the overhead bar denotes the mean value. A suitable measurement for this purpose is taking an image of an out-focus knife edge object as this will create a large spread in gray scale values, making the linear fit of Eq.(5.16) more reliable. Typically 10 images are sufficient for a precise measurement. The offset is found from the average of a set of dark images. A dark image is a recorded image without any light reaching the sensor.

OTF-BASED ABERRATIONS EXTRACTION

Previously we have developed a non-invasive optical quality assessment tool [43], which uses the through-focus edge response of a custom-made resolution target. From these data we estimated the through-focus OTF, which on its turn was the input for extracting the primary aberrations. The pipeline for quantifying astigmatism, coma, and spherical aberration is depicted in Fig. 5.5. This procedure expresses the aforementioned aberrations in the standard Zernike aberration coefficients, which can be used later on in the full-field aberration analysis to test and improve alignment. The details have been explained extensively in chapter 2.

Additionally, the image of horizontal and vertical edges of the custom-built resolution target can be analyzed to extract distortion information. This information, however, only holds for a fixed position and only along a line in the scan direction, because each sensorlet images only one line in the circular FOV. Having this limitation, two parameters can be measured that characterize distortion. The first parameter indicates the deformation of a straight line due to the change of magnification along the scan direction. This can be quantified by fitting a parabola to the edge response of the horizontal bars. The second parameter is the magnification error $\Delta M(x_f)$ along the field direction, which is equal to $l(x_f)/l_{ref} - 1$ where x_f is the position in the field direction, $l(x_f)$ is the length of the vertical bar at x_f , and l_{ref} is the true length. This can also be modeled by a parabola. The distortion effect on the image can be corrected for by post processing using the calibrated values for these parameters.

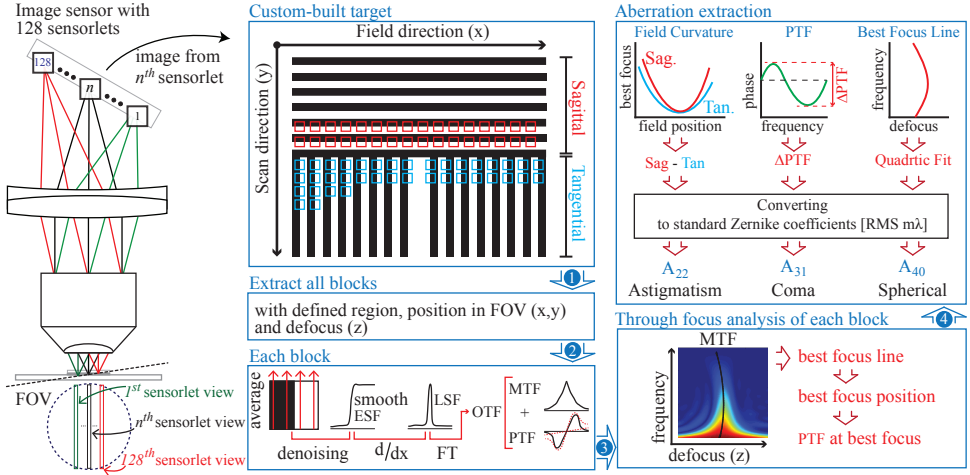


Figure 5.5: Aberration extraction pipeline for the lowest-order aberrations such as astigmatism, coma and spherical aberration [43]. The measured aberrations of all the sensorlets provide the full-field aberration map.

5

NODAL ABERRATION THEORY BASED ANALYSIS OF FULL-FIELD ABERRATION MAPS

We explained in chapter 3 how aberrations such as astigmatism and coma can be decomposed into a constant component and a component that varies along the field direction. Since our 3D WSI platform has 128 sensorlets distributed along the scan direction, each of them projects onto a different position in the object plane and hence has a different overall constant aberration component. The variation of the measured aberration components across the different sensorlets provides insightful information about the alignment of the whole optical system based on Nodal Aberration Theory (NAT). NAT is an appropriate framework for analyzing the effect of misalignment on the field dependency of aberrations for small field-angle optical imaging systems, i.e. systems for which the field coordinates in object space (x, y) are much smaller than the objective's focal length [44, 47–49]. In this subsection, we will briefly present the predictions of NAT for the field dependency of the measured aberrations of our line scan WSI platform. The topology of full-field aberration maps can be characterized by the nodes, which are defined as the points in the FOV where the aberration under study is zero. For well-aligned rotationally symmetrical optical systems, the full-field aberration map is rotationally symmetric as well. The map will then have one node at the center of the FOV (the optical axis). Misalignment breaks the rotational symmetry and shifts or even creates new nodes. For example, the field dependency of the lowest-order astigmatism in a well-aligned system is quadratic and any kind of misalignment will add terms that are constant and linear in the field and scan coordinates. The Zernike coefficients for horizontal/vertical and diagonal astigmatism according to NAT are [44]:

$$\begin{aligned}
 A_{22}(x, y) &= a_q(x^2 - y^2) - a_y y + a_x x + a_h, \\
 A_{2-2}(x, y) &= 2a_q xy + a_y x + a_x y + a_d,
 \end{aligned}
 \tag{5.17}$$

with x and y the positions in the field direction and the scan direction respectively. The linear and constant terms are non-zero only in misaligned systems. The quadratic coefficient a_q is determined by the optical design and is independent of misalignment. The nodes are found at field positions, which can be conveniently expressed in complex notation as:

$$x_n + iy_n = \frac{-(a_x + ia_y) \pm \sqrt{(a_x + ia_y)^2 - 4a_q(a_h + ia_d)}}{2a_q} \quad (5.18)$$

Each sensorlet has a fixed position y_s along the scan direction and hence the field dependency of A_{22} can be rewritten as:

$$\begin{aligned} A_{22}(x, y_s) &= a_q x^2 + a_x x + a_c, \\ a_c &= (a_h - a_q y_s^2 - a_y y_s), \end{aligned} \quad (5.19)$$

The position y_s at which the component a_c , that is independent of the field coordinate x , reaches zero corresponds to the center of the FOV.

For coma the field dependency is linear. According to NAT the coma Zernike coefficients along the field (x , tangential) and scan (y , sagittal) directions are given by:

$$\begin{aligned} A_{31}(x, y) &= c_l x + c_x, \\ A_{3-1}(x, y) &= c_l y + c_y, \end{aligned} \quad (5.20)$$

The linear coma coefficient c_l is inherent to the optical design and measures the deviation of aplanaticity ("Offense against the Sine Condition", OSC). For each sensorlet having a fixed position in the scan direction, it appears that A_{3-1} is constant over the FOV.

5.2.3. IMAGE ANALYSIS

DENOISING

The raw images generated by the prototype sensor show visible vertical and horizontal line-to-line noise. The vertical line-to-line noise is due to pixel-to-pixel variations in gain and offset, the horizontal line-to-line noise is due to a manufacturing bug of the first prototype. The image content affects the black level offset of the Analog-to-Digital Converter (ADC). In order to remove this noise we exploit the powerful statistical technique of Principle Component Analysis (PCA) [50]. Starting point is the full dataset $Z = [z_1 z_2 \dots z_n]$, a $k \times n$ matrix where z_j is a column vector of k elements for the j^{th} observation. Here z_j represents the signal of a row of pixels for scan position y_j , so k is the number of pixels in a single row and n is the number of samples taken in the scan direction. PCA computes an orthonormal matrix P , which transforms Z to $Q = P(Z - m_z)$ such the covariance matrix $C_q = PC_z P^T$ is diagonal. Here the mean m_z and the covariance matrix C_z are defined by:

$$\begin{aligned} m_z &= \frac{1}{n} \sum_{i=1}^n z_i \\ C_z &= \frac{1}{n} \sum_{i=1}^n z_i z_i^T - m_z m_z^T \end{aligned} \quad (5.21)$$

The m rows of P , the eigenvectors of P , are called the principal components. The corresponding diagonal elements of C_q , the eigenvalues, determines the relative importance of the principal components.

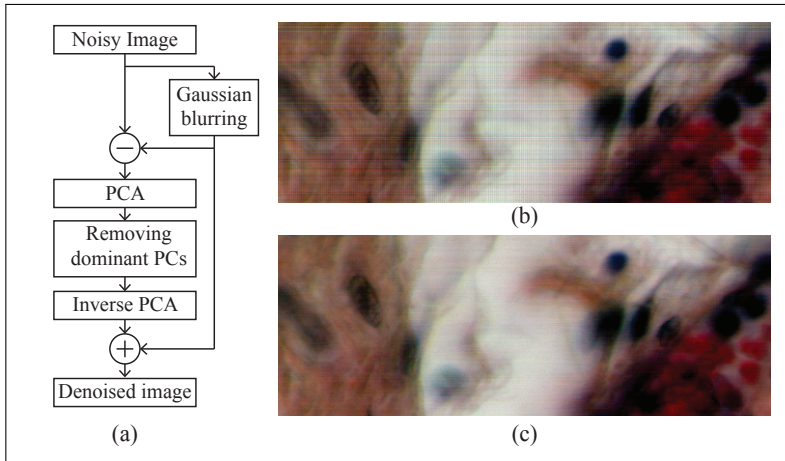


Figure 5.6: (a) Diagram of the PCA-based denoising algorithm to suppress line-to-line noise. (b) Before denoising. (c) After denoising.

Under the assumption that the image content is not translation-invariant along the rows or columns of the image, the principal component with the highest eigenvalue corresponds to the line-to-line noise feature. Removing this principal component and then reconstructing the signal with the orthonormal matrix P will suppress the line-to-line noise. Before applying this PCA-based noise suppression, a blurred version of the input image is subtracted from the raw image in order to remove the object dependent low-frequency structures. This blurred image is added after the inverse PCA operation to form the final denoised image. This denoising algorithm (Fig.5.6) is repeated in the other orthogonal direction to remove the vertical line-to-line noise as well.

MULTISPECTRAL ANALYSIS

The scanner platform provides 5 color channel images. A standard 3-channel RGB representation can be obtained by taking a suitable weighted sums of the 5 color channels. For relatively simple stains, such as the pink and blue Haematoxylin & Eosin (H&E) stains, such a representation is sufficient to clearly recognize the highlighted structures. When multiple stains are used concurrently, there will be significant cross-talk between the differently stained structures in an RGB image. Using the full 5-color channels opens the opportunity to disentangle the structures highlighted by different stains, provided the spectral overlap between the stains is sufficiently small. We can also employ PCA in this context to find the dominant color channels in the image, which are hypothesized to be associated to the different stains that are used.

The first step in the algorithm (see Fig.5.7) is to prepare a 5-dimensional data set $I_{N \times C}$ from a 5-color channel image, where N is the total number of pixels of the image in each color layer and C is the number of color layers. Applying PCA to the dataset I gives

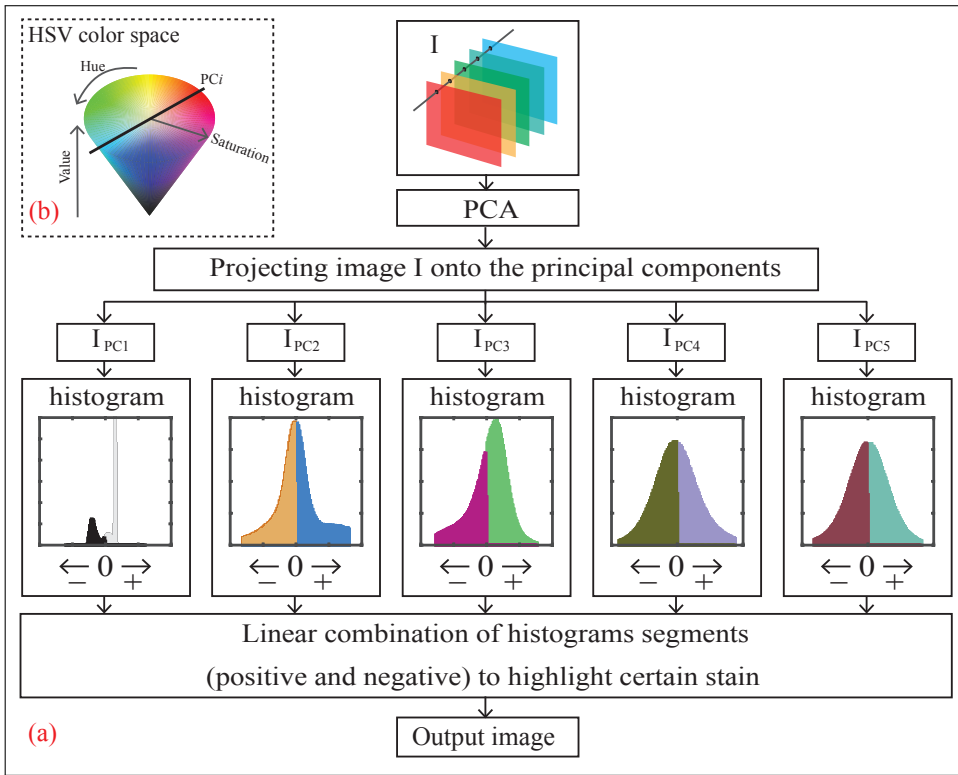


Figure 5.7: (a) PCA-based algorithm to analyze 5-color images with the aim of highlighting certain stains in a scanned tissue slide. (b) Hue Saturation Value (HSV) color space. Hue is an angle that represents color. Saturation is the pureness value of the specific color and Value denotes its brightness. The circular distribution of Hue shows that a color pair can be located in opposite direction, for example yellow-blue or red-green. PCA finds sets of new axes in multicolor image space along which the image has the largest variations. Each axis covers one pair of opposite colors in color space.

five principal components. Then I is projected onto each of these principal components to compute the projected images I_{PCi} , where $i=1$ to 5. Each principal component is defined by a vector in the 5-dimensional color space along which the dataset has a large variation. This vector covers two opposite colors (see HSV color map in 5.7b). Therefore I_{PCi} mostly contains data points with these two dominant colors which can be separated using its histogram. The histogram of I_{PCi} consists of a positive segment $H^+(I_{PCi})$ and a negative segment $H^-(I_{PCi})$, since the mean value of the image is subtracted in the PCA computation (Fig.5.7a). These two segments correspond to the surplus of the first color and the deficit of the second color respectively. After decomposing the image into these histogram segments, the output image can be reconstructed by:

$$I_{out} = \sum_{i=1}^5 (p_i H^-(I_{PCi}) + n_i H^+(I_{PCi})), \quad (5.22)$$

where p_i and n_i are the weight coefficients for positive and negative segments respectively. Their values can be chosen depending on which stain (i.e. combination of seg-

ments) is to be highlighted or removed.

QUANTITATIVE PHASE IMAGING

Native, unprocessed cells and tissues are translucent as they absorb light only weakly. An absorption stain is needed for viewing relevant structures under a conventional trans-illuminated (brightfield) microscope. In some cases it is not possible, however, to apply staining, e.g. in live cell imaging, or when the morphology can be changed by chemical reactions between the native biological material and the staining chemicals. One way to view the structure of the sample in its native unstained state is phase-contrast imaging. Phase-contrast imaging visualizes the refractive index variations across the sample, which are not visible in trans-illuminated microscopy when the specimen is in focus. Defocusing the sample can make the refractive index variations visible as it causes local phase changes in the passing wavefront, which cause contrast by interference of the propagation wavefront [51]. This has been exploited in defocused-based phase imaging techniques [33, 35] in which several images at different focus levels are used to reconstruct a single phase image of a thin object. The simplest method to find the phase uses the Transport of Intensity Equation (TIE) [52]:

$$\frac{2\pi}{\lambda} \frac{dI}{dz} = -\vec{\nabla} \cdot (I \vec{\nabla} \phi), \quad (5.23)$$

where I is the intensity, ϕ is the phase, z is the axial position and λ is the wavelength. If the intensity I is known then Eq.5.23 can be written as the Poisson equation:

$$\nabla^2 \psi = \frac{-2\pi}{\lambda} \frac{dI}{dz}, \quad (5.24)$$

where ψ satisfies $\vec{\nabla} \psi = I \cdot \vec{\nabla} \phi$. Several computational techniques exist to solve the TIE to provide an estimate of the phase image ϕ [36, 53, 54]. We use a Kalman-filtering based method proposed by Waller and co-workers [34, 37]. Kalman filtering is a well-known

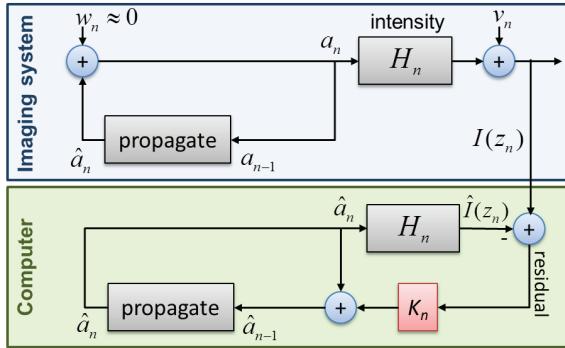


Figure 5.8: Schematic diagram of the Kalman Filter algorithm for solving the TIE (image from [37]).

algorithm in the field of stochastic signal analysis to estimate the unknown parameters that describe the dynamics of a system from a series of noise corrupted measurements. The dynamical system in the current context is the 2D optical complex-field as a function of the axial position z , which is estimated recursively using the set of measured

through-focus intensity images. Fig. 5.8 shows the schematic diagram of the Kalman filter algorithm. The model of the imaging system consists of two sub-models. One for propagating the previous state of the 2D optical complex field a_{n-1} at axial distance z_{n-1} to the current state a_n , and the other is an observation model H_n to provide the intensity image $I(z_n)$ from the optical complex field at each axial position. At each iteration the predicted intensity image $\hat{I}(z_n)$ is compared to the measured intensity image $I(z_n)$, and the residual is used to correct the next estimation of the states. The Kalman gain matrix K_n is also updated based on the covariance matrix of the states. The Kalman filter is a linear estimator, however, translating an optical field to intensity images is a nonlinear process. To address this, a nonlinear version called the Extended Kalman filter (EKF) is used. EKF linearizes the model around an estimate of the current mean and covariance. The updating process needs the covariance matrix and its inverse, which introduces a computational complexity of $\mathcal{O}(N^3)$ where N is the image total number of the pixels. To reduce the computational complexity we employ theorems that were derived to simplify the update equations and gain of an augmented complex EKF [34].

5.3. RESULTS

5.3.1. SENSOR CHARACTERIZATION

The sensor characterization is illustrated by showing the pixel variance as a function of pixel value, which is shown for five color channels of the 65th sensorlet (see Fig.5.9). The results are based on the analysis of 19 sets of out-of-focus edge and dark images from the sensorlet 65 after the PCA based suppression of the line-to-line noise. Due to a bug in the design, the sensorlets are only sensitive to a gain variation close to the maximum limit. This forced us to set a high gain for each sensorlet to have the largest possible dynamic range, which is about 20% of the full dynamic range (1024 ADUs for the 10 bit AD converter that was used). The graphs of pixel variance as a function of pixel value are shown in 5.9 for the five color channels. The average gain is 83 e^- /ADU which is estimated from the obtained intensity range of 0-160 ADU. The offset of about 56 ADU is removed. The average readout noise is 1.17 ADU rms which leads to 97 e^- /ADU because of the high gain.

5.3.2. OPTICAL CHARACTERIZATION

The result of our optical quality analysis for a single sensorlet (62^{nd}) are shown in Figs 5.10 to Fig.5.13 for astigmatism, field curvature, coma, spherical aberration and barrel/pincushion distortion. We used the Nikon 20 \times /NA0.75 Plan apochromat VC with its matched tube lens of 222.4 mm focal length and the 3-color sequential illumination unit (see Chapter 4). The analysis is presented for the red, green and blue color channels of the three-color illumination unit. The measured astigmatism close to the edge of the field is slightly above 72 $m\lambda$ (Fig.5.10d). The best focus curve for the blue color channel in Fig.5.10b is more 4th order than 2nd order, indicating the presence of higher-order field curvature and astigmatism. The measured PTF of the green color is shown in Fig.5.11a and b for the tangential and sagittal regions of the resolution target respectively. The variation in tangential coma (part c), across half the FOV for the red, green and blue color channels is $24\pm 16 m\lambda$, $22\pm 21 m\lambda$, $80\pm 43 m\lambda$, respectively. The missing

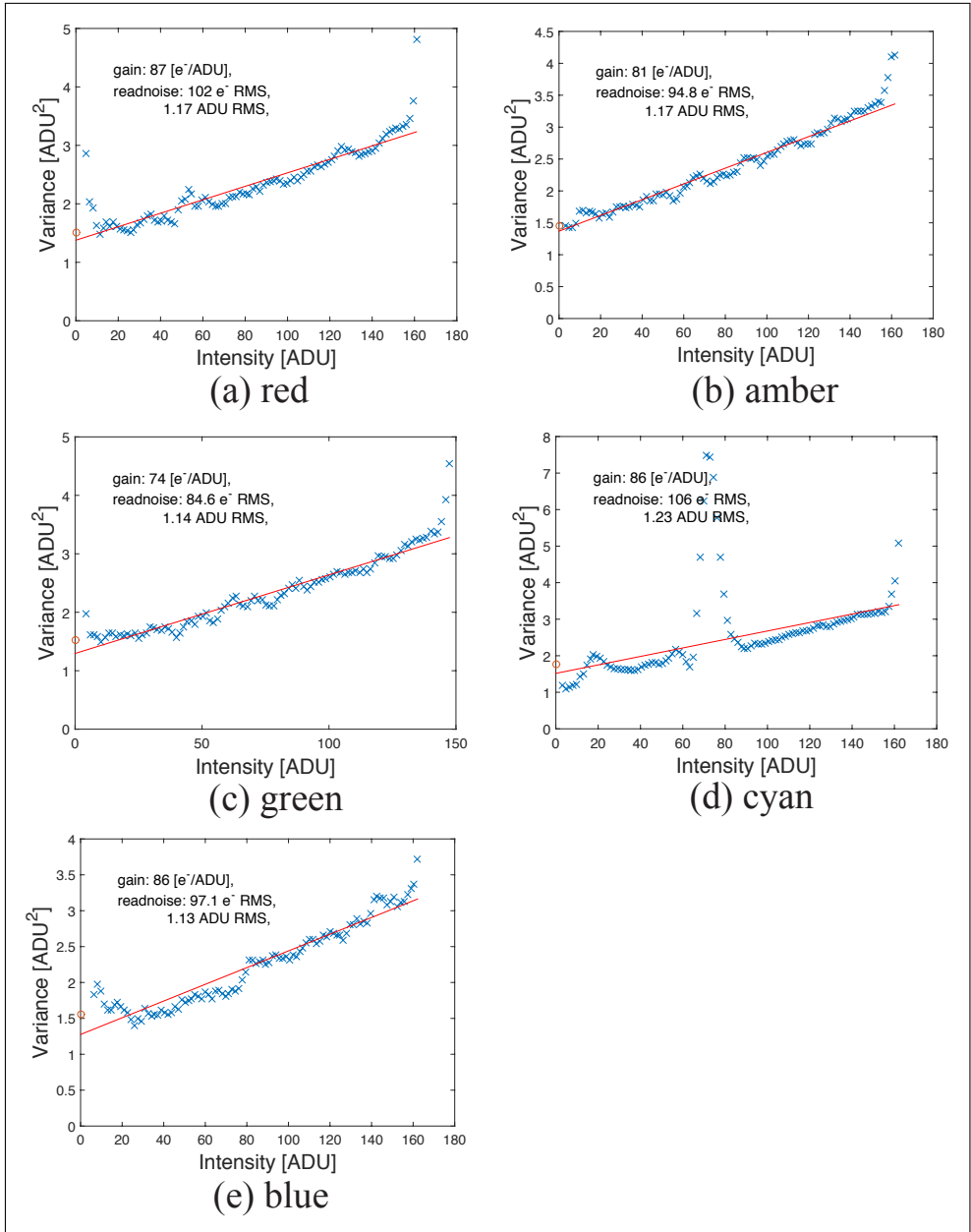


Figure 5.9: Pixel variance as a function of pixel value for the five color channels of the 65th sensorlet.

data points are due to the failure of finding the maximum deviation from the measured PTF (see section 2.2.3 in chapter 2). This occurs more for the sagittal coma (part d) due to the relatively higher uncertainty and noise in that region. The maximum coma values for the valid data points across the FOV are 14 ± 44 m λ , 3 ± 38 m λ , 13 ± 47 m λ for the red, green, and blue color channels respectively. For both tangential and sagittal regions, coma values for the blue color channel are higher than the diffraction limit.

In Fig.5.12, the measured spherical aberration across the FOV is plotted for three colors. The estimated aberrations for red, green, and blue are -14 ± 18 m λ , 20 ± 14 m λ , 28 ± 40 m λ . These values are obtained from the weighted mean of about 1200 data points with the inverse-square of their uncertainty as weight. The distortion analysis is shown in Fig.5.13. The lateral magnification error is below 6 pixels across the FOV (Fig.5.13a), and the errors between different colors is below 0.5 pixel (Fig.5.13b) implying that a post-acquisition color registration is not needed. However, the deformation of straight lines along the field direction (Fig.5.13c) is visible and do need post-processing for correction.

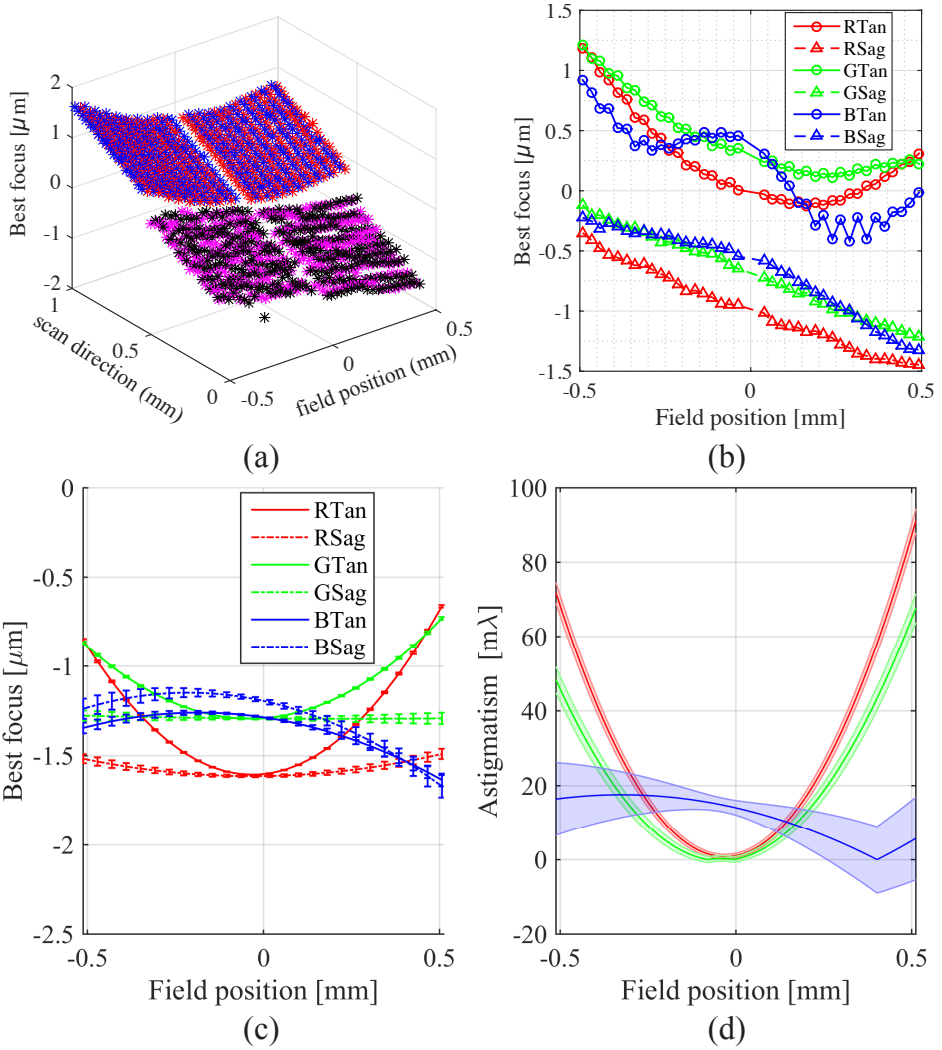


Figure 5.10: Field curvature and astigmatism analysis for sensorlet 62. (a) Distribution of the measured best focus across the field and scan direction for the green color channel. (b) Averaged field curvatures for three color channels in the tangential (solid line) and sagittal (dashed line) regions. (c) Calibrated field curvatures. Both tilt in field and scan direction are estimated and then removed from field curvatures. (d) RMS value of the astigmatism for three color channels with their statistical uncertainty (shaded area).

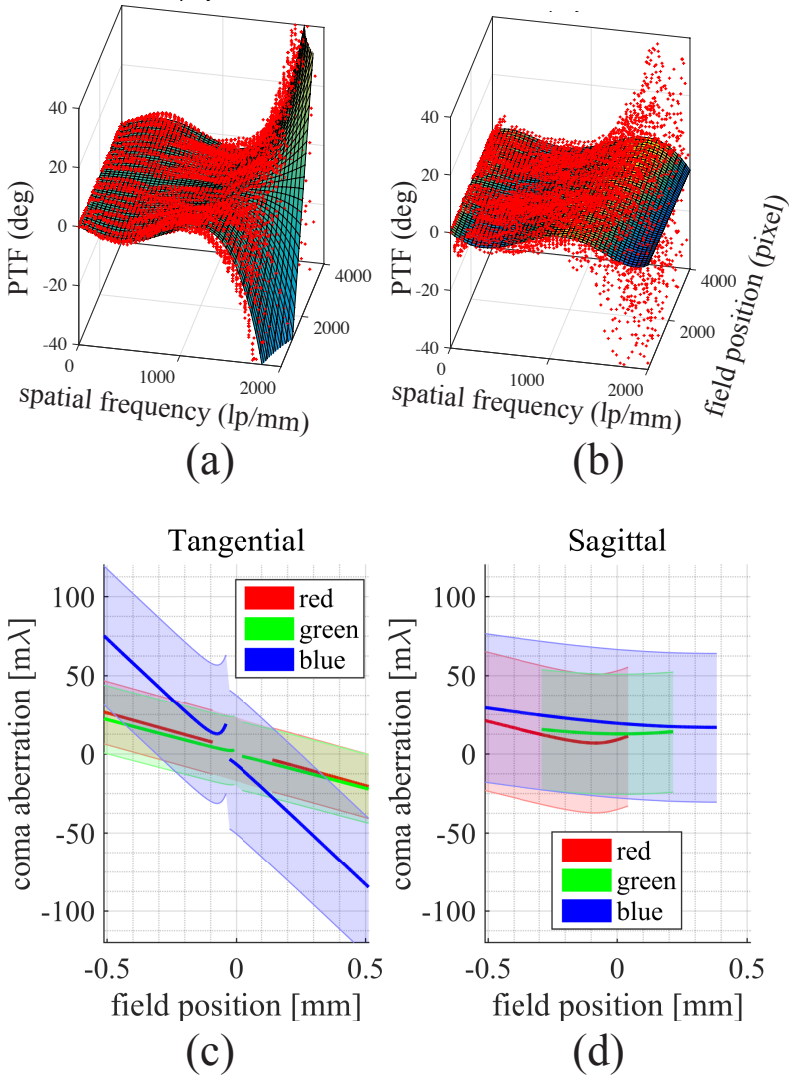


Figure 5.11: Coma analysis for sensorlet 62. Graphs (a) and (b) show the measured PTF for the green color channel in tangential and sagittal region of the resolution target. Red dots denote the measured data points and the surface is a 2D polynomial fit. Graph (c) and (d) shows the RMS value of the tangential and sagittal coma.

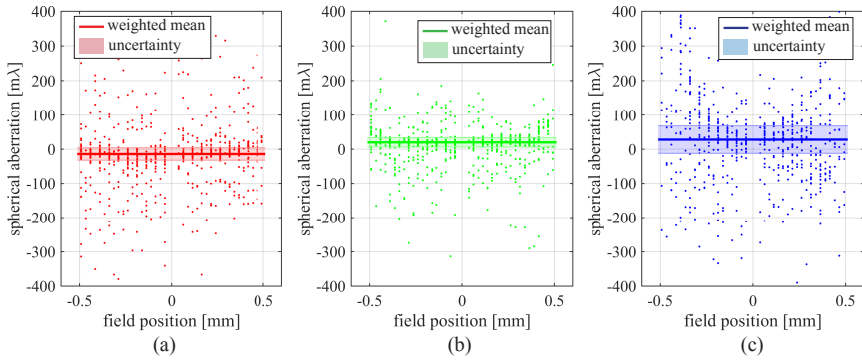


Figure 5.12: Measured spherical aberration of sensorlet 62 for (a) red, (b) green, (c) blue.

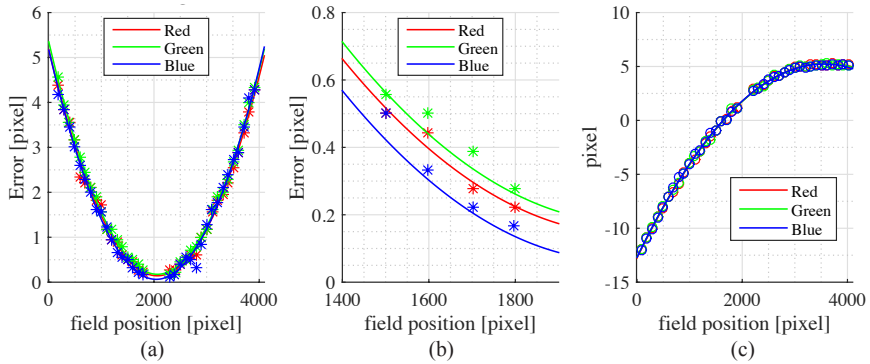


Figure 5.13: Distortion analysis for sensorlet 62. (a) Lateral magnification error in pixels for three colors. (b) Zoomed in version of part a. (c) Line deformation for three colors.

The full-field aberration analysis of the measured aberrations from five sensorlets (1, 32, 62, 96, and 128) is shown in Fig.5.14 and Fig.5.15. The quadratic, linear and constant coefficients for astigmatism are plotted in Fig.5.14a for red, green, and blue colors. The constant coefficients increase with the sensorlet number, in agreement with expectations. We see noticeable variation for the quadratic coefficients, which might be caused by the change in conjugate across the sensorlets. Part (b) shows the linear and constant coefficients for coma. The zero-crossing for the constant coefficient of sagittal coma is around sensorlet 90, which suggests that the zero node for coma in the scan direction must be around this sensorlet. The linear coefficients for tangential coma (red and green color) also reach a minimum around the same sensorlet. In this way the sensorlet with the least amount of coma can be identified. The maximum of the measured statistical uncertainties for the coma coefficients are smaller than those for astigmatism and spherical aberration. The maximum values for c_l in tangential and sagittal regions, c_x , and c_y are 2.1, 9.3, 0.1 and 1.7 respectively. There might be an additional systematic error originating from the calculation of coma for each field point (see section 2.2.3 in chapter 2).

In part (c), the amount of spherical aberration is shown. We measured a change of 94 mλ from the first to the last sensorlet, which is about 2.3 times larger than the expected

value from the model presented in the method section. This deviation can possibly be attributed to the relatively large uncertainty of the measurements. In Fig.5.15a, coefficients of the 2nd order polynomial used to fit the measured line deformation are shown. The quadratic coefficient crosses zero around the 105th sensorlet (interpolated value) which is close to the number found from the zero-crossing of the constant coefficient for sagittal coma. Lateral magnification coefficients have less variation over the set of sensorlets (Fig.5.15b), although the quadratic coefficient decreases slightly around sensorlet 95.

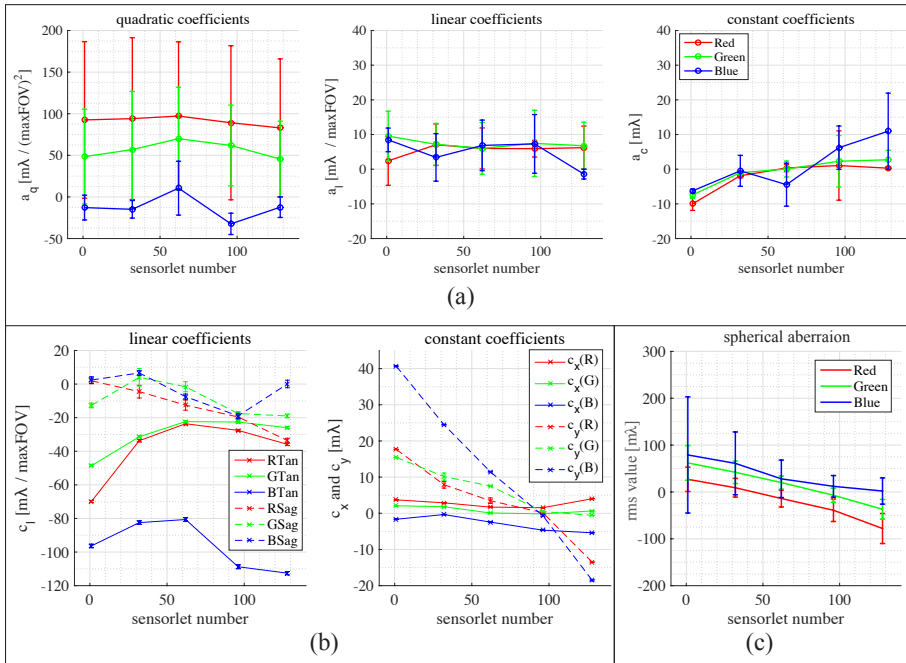


Figure 5.14: Full-field aberration analysis. R, G, B stands for red, green and blue color. Tan and Sag refer to tangential and sagittal regions. (a) Quadratic, linear, and constant coefficients for astigmatism. (b) Linear and constant coefficients for coma. (c) Estimated spherical aberrations with uncertainty for five sensorlets.

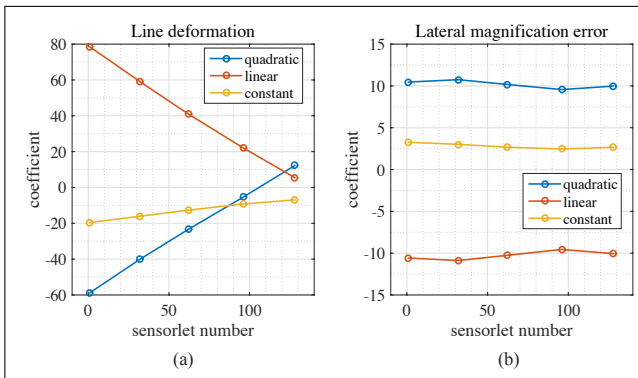


Figure 5.15: Distortion analysis of five sensorlets for the green color. Coefficients of the 2nd order polynomial fitted to: (a) Deformed straight line from five sensorlets. (b) Measured lateral magnification error.

5.3.3. H&E STAINED TISSUE SLIDES

Here we present images of four H&E stained prostate tissue slides of different specimen thickness. The results depict a satisfactory overall image quality in terms of: a low noise visibility by applying the PCA noise suppression method, a good color fidelity due to the well-designed optical system with virtually zero lateral chromatic aberration, and a good level of sharpness in agreement with the diffraction-limited performance found in the optical quality test. This tissue slides are stained using H&E and have different staining dilution. Fig. 5.16 shows the result of a scan with 10 sensorlets of a prostate tissue slide of the standard 4 μm thickness and standard dilution scanned with the Nikon 20 \times /NA0.75 objective lens. Part of the tissue layer is folded and creates a 3D structure in the slide. In Fig. 5.17, a thicker slab (20 μm) prepared using a 5 \times higher dilution (lower stain concentration) than the standard dilution is shown. Using more diluted H&E staining provides more clear images for the 20 μm thick specimen. To scan even thicker specimen, we used the Nikon 10 \times /NA0.45 objective lens to reduce spherical aberrations. In Figs. 5.18 and 5.19 scans of prostate tissue slides of 60 and 100 μm specimen thickness are shown. The focus difference between the layers is 16 μm . For the scan of the 60 μm thick specimen shown in Fig. 5.18, the different cell layers can hardly be recognized in the through-focus images. The images are mostly blurred by light scattered from the out of focus layers of the specimen. The dominant scattering mechanism may be related to the lipid structures in the tissue, which have a refractive index that deviates from the surrounding media. This effect gets even worse in the images of the 100 μm thick specimen (Fig. 5.19).

5.3.4. MULTISPECTRAL IMAGE ANALYSIS

In Fig. 5.20, we present the results of our PCA-based multispectral analysis on an image of a prostate tissue slide stained with H&E and two additional stains: brown for marking the basal cell layer (Keratin 5, K5) and blue for highlighting the cell layer directly above the basal cell layer (K8/K18). In column (a), all the five color channels of the original image are shown where the RGB rendering is obtained from the LED spectrum. The projection of these five color layers onto the principal components are shown in column (b). As explained in the methods section, each of these projections contains data points of two dominant colors. We observe that there are three dominant principal components. The first (b_1) contains mostly intensity information, the second (b_2) projects data points along the blue-yellow color axis, and the third (b_3) projects data points along the pink-green color axis. The last two principal components do not contain relevant color information for this sample, and are subsequently discarded. The histogram segments of the first three principal components allowed us to remove or highlight a specific stain/information in the scanned image. Column (c) shows the resulting images. In (c_1) the original image is shown in which the brown stained layer between the H&E and blue colored cells is hardly visible. Using the information from (b_2), this stain can be highlighted (see c_2) or removed (see c_3). The Eosin (pink color) and the blue coloring are removed in c_4 and c_5 respectively.

5.3.5. DEFOCUS-BASED PHASE RETRIEVAL

We prepared an unstained slide of several cheek cells for testing the defocus based phase retrieval algorithm. A single 10-sensorlet scan provides a through-focus stack of images, which is used in the ACEKF algorithm to retrieve the phase and the intensity. The result is shown in Fig.5.21. In part (a), the intensity image of the green color layer for 4 of the sensorlets that have scanned at different focus levels are shown. It can be seen that the nuclei of these cells are invisible in the scanned plane where the layer is in focus and change appearance from bright to dark as the focus changes. The retrieved phase from the stack of through-focus images gives a clear view of the cells and their nuclei. We retrieved the intensity and phase for each color channel and the average over the five color channels are shown in Fig.5.21b & c).

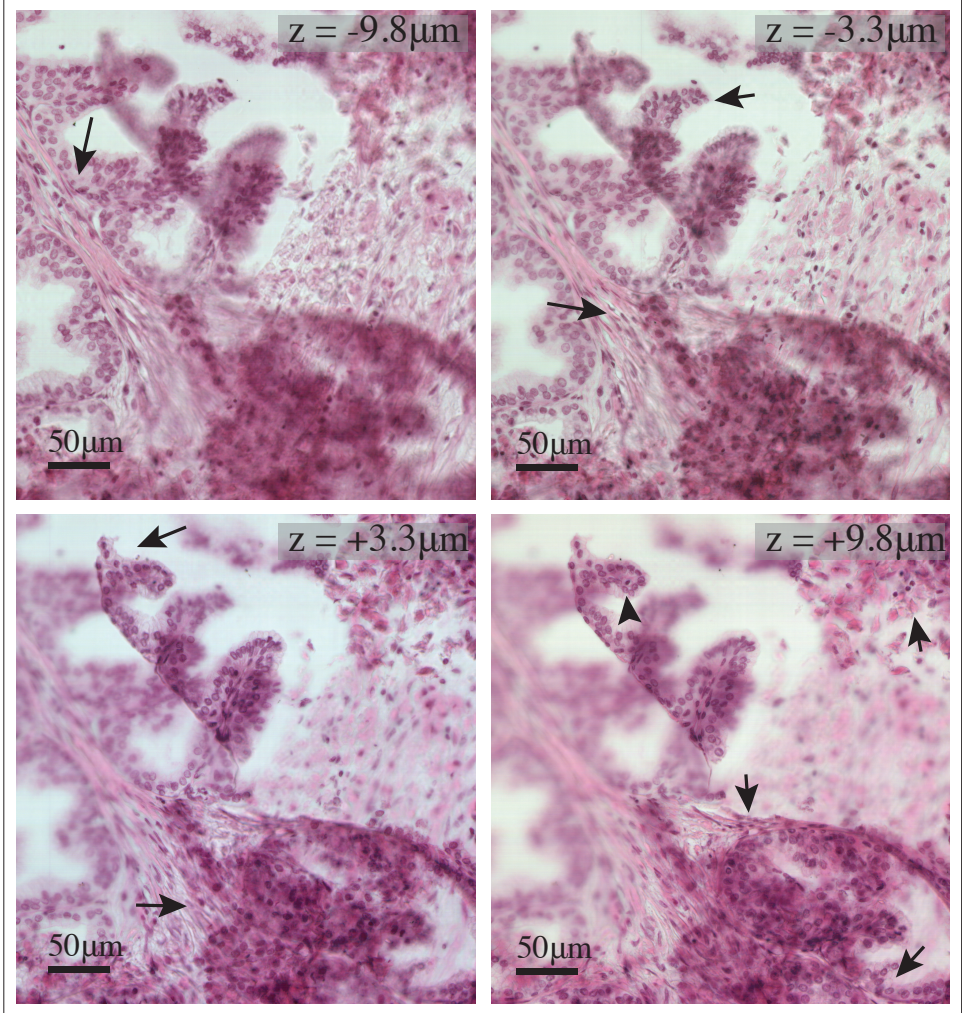


Figure 5.16: A $4\mu\text{m}$ thick prostate tissue slide stained with H&E at 4 out of 10 scanned focus levels from a single pass 10-sensorlet scan. Indicated z is the distance from the axial position of the middle sensorlet projected in object space. The main in-focus areas are annotated with arrows. It can be seen that part of the tissue is folded, which creates a visible focus transition through the layers.

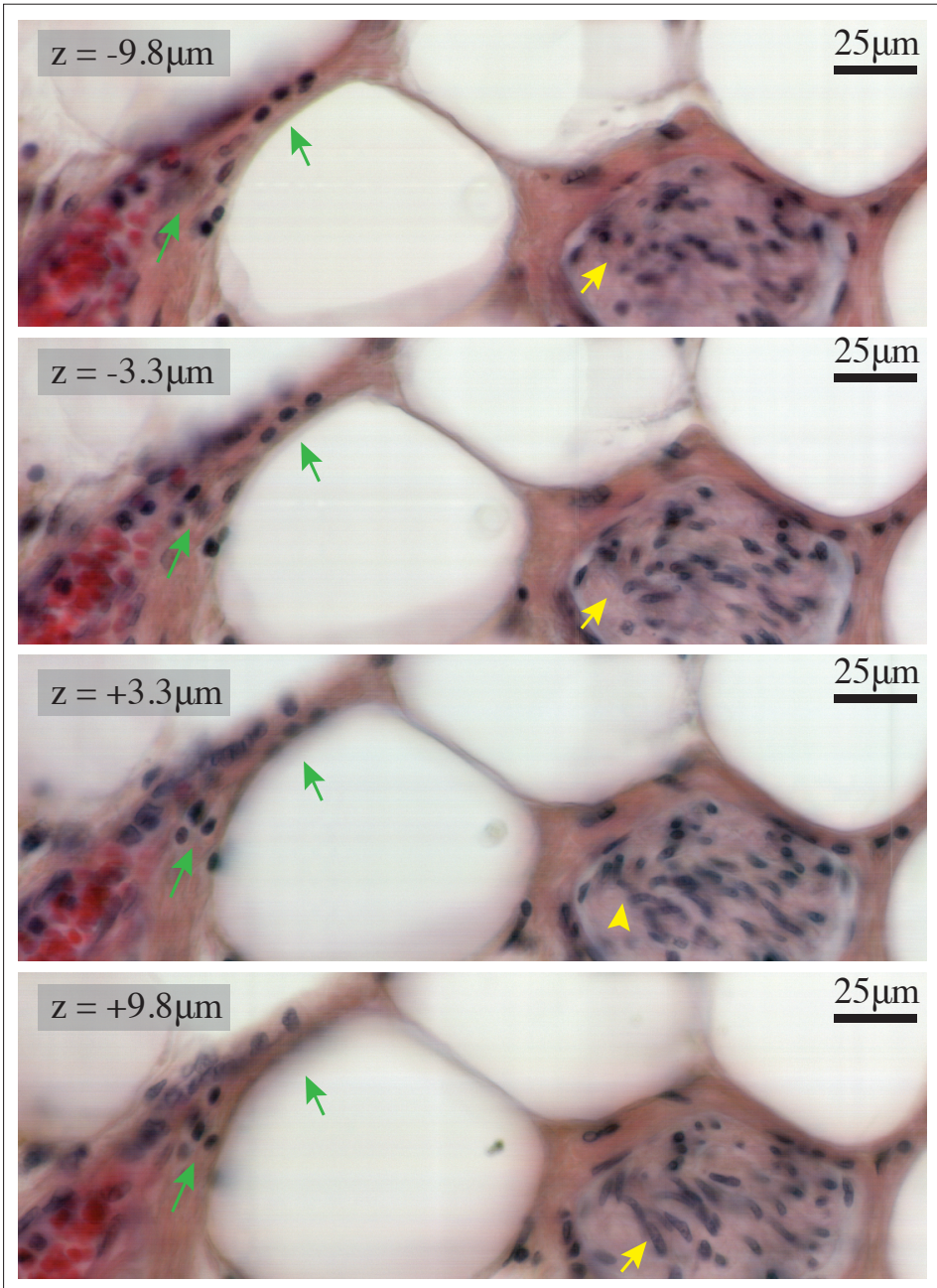


Figure 5.17: Focal slices of a 3D-image of a $20 \mu\text{m}$ thick prostate tissue slide stained with H&E at five times lower staining concentration than the standard concentration. Four slices of a single scan with 10 sensorlets are shown, with a focus difference of $6.5 \mu\text{m}$. The indicated z -position is the distance from the axial position of the middle sensorlet in object space. The green and yellow arrows indicate nuclei that are in focus at different scan planes.

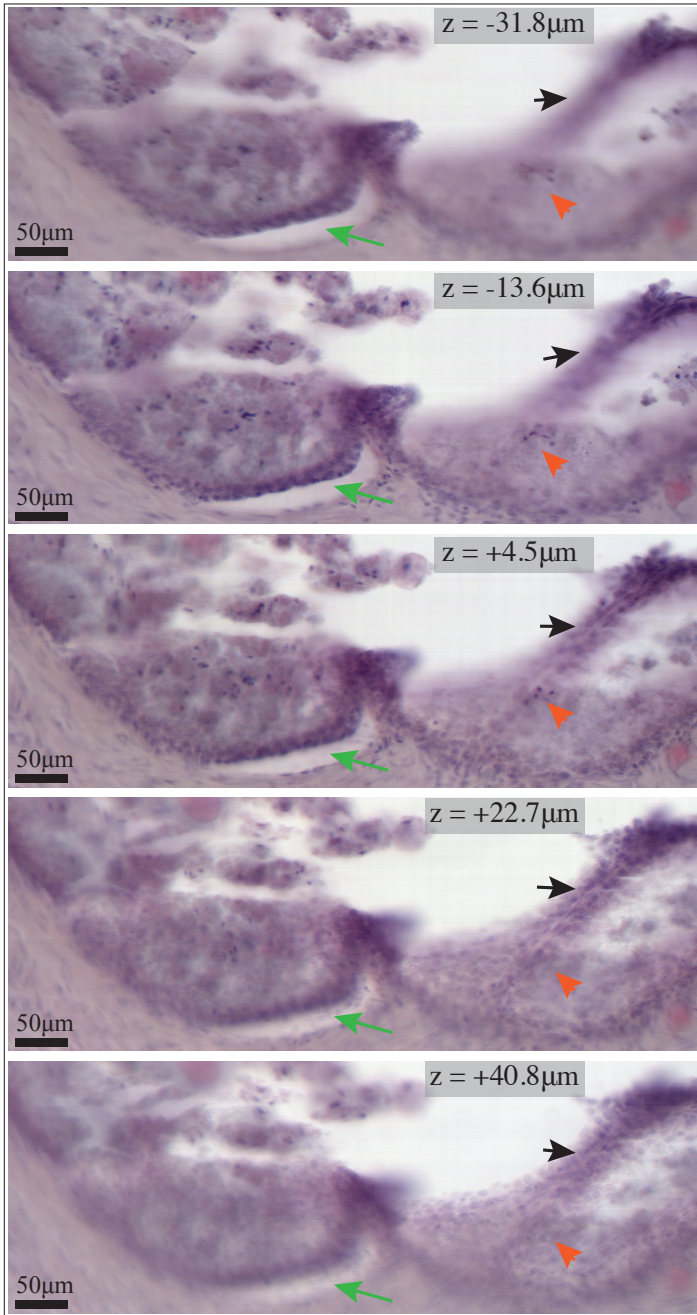


Figure 5.18: Focal slices of a 3D-image of a $60\mu\text{m}$ thick prostate tissue slide stained with H&E at ten times lower staining concentration than the standard concentration. Four slices of a single scan with 10 sensorlets are shown, with a focus difference of $18.1\mu\text{m}$. The indicated z -position is the distance from the axial position of the middle sensorlet in object space. The green, black and orange arrows indicate nuclei that are in focus at different scan planes.

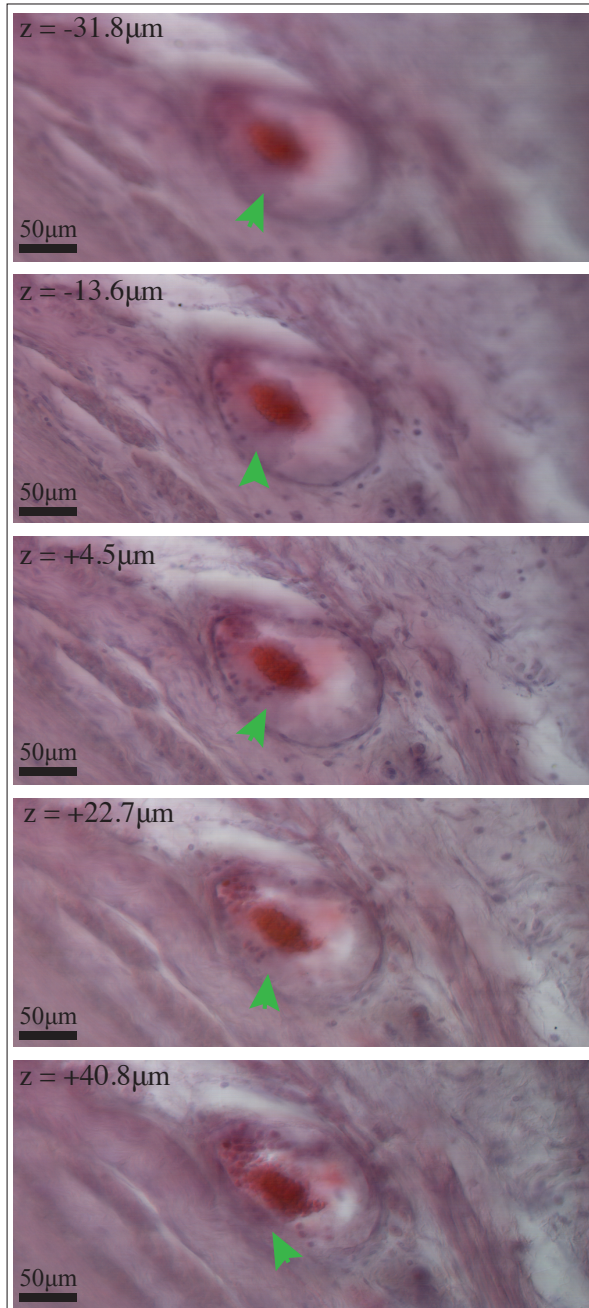


Figure 5.19: Focal slices of a 3D-image of a $100\mu\text{m}$ thick prostate tissue slide stained with H&E at ten times lower staining concentration than the standard concentration. Four slices of a single scan with 10 sensorlets are shown, with a focus difference of $18.1\mu\text{m}$. The indicated z-position is the distance from the axial position of the middle sensorlet in object space. The green arrows indicate nuclei that are in focus at different scan planes.

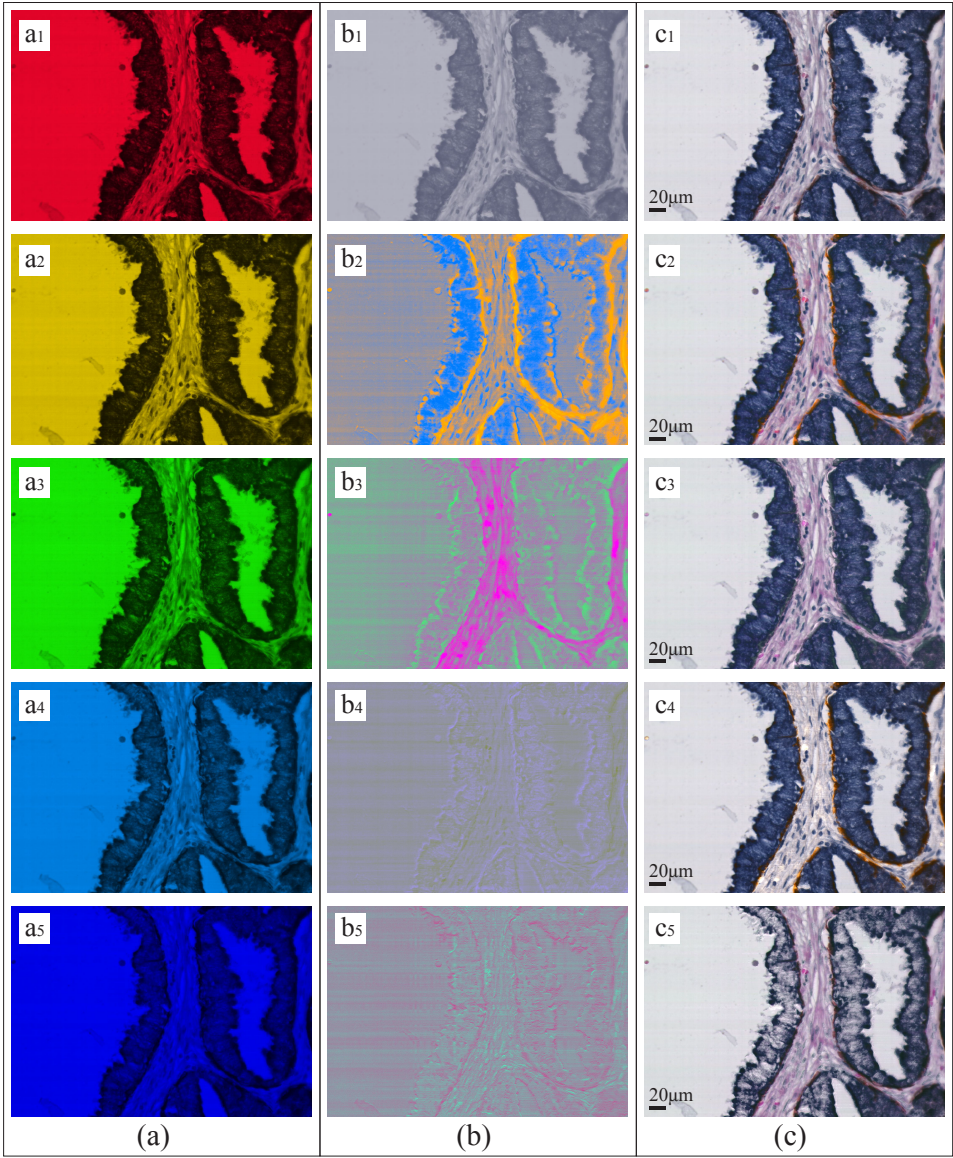


Figure 5.20: Multispectral analysis of a prostate tissue specimen stained with H&E, a brown stain (basal cells, K5), and a blue stain (cells above basal membrane, K8/K18). (a) Original five measured color channels (red, amber, green, cyan and blue). (b) Projected images I_{PCi} along the five principal components. (c) Computationally reconstructed RGB images obtained with the PCA-based multispectral analysis: (c₁) Original. (c₂) Brown stain is enhanced. (c₃) Brown stain is removed. (c₄) Eosin is removed and brown stain is enhanced. (c₅) Blue stain is removed.

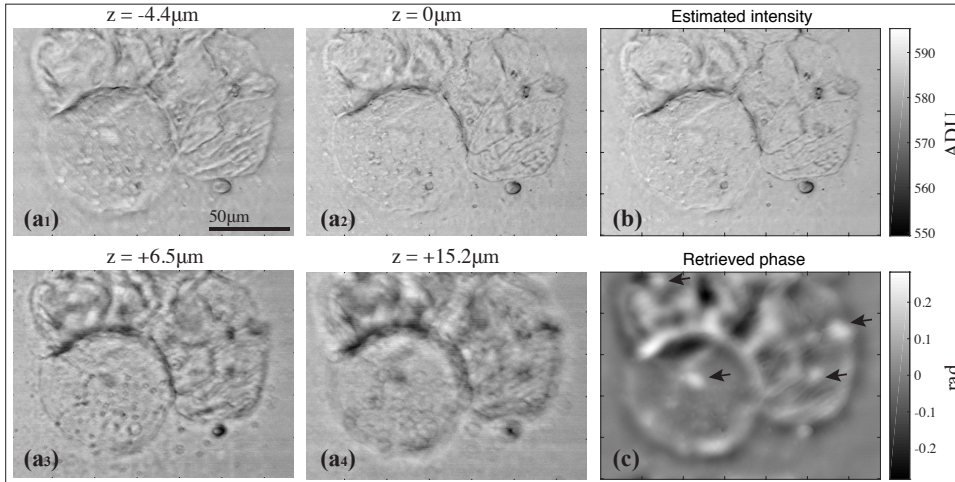


Figure 5.21: Unstained cheek cells in a single scan. (a₁ to a₄) Image of cheek cells at four focus levels for the green color layer. (b) and (c) Average of estimated intensity and phase of five color channels by applying the sparse ACEKF algorithm to a stack of through-focus images with 10 focus levels. Arrows show the positions of nuclei in the retrieved phase image.

5.4. DISCUSSION

To summarize, we have presented proof-of-principle experiments and a characterization of a novel 3D multispectral WSI platform for application in digital pathology based on a new custom-designed image sensor placed tilted in the scan direction at the image plane. This configuration enables simultaneous scanning of different focus levels. We have built an experimental setup to scan simultaneously 10 different focus levels using 10 sensorlets of the image sensor. We also built a LED-based color sequential illumination unit with five colors. We have achieved a scanning speed of 5 k lines/s for one color scanning using a first prototype of the sensor. The design goal is to reach a maximum 200 k lines/s for a single sensorlet.

We have estimated the gain and readout noise for a single sensorlet. The resulting numbers are unrealistically high and probably due to the fact that the ADC must be operated at high gain and offset in order to get reasonable contrast. The measured primary aberrations for a single sensorlet shows the overall diffraction-limited performance with two exceptions: astigmatism close to the edge of the FOV and coma for the blue color channel. These findings can be used in further optimization of the design of the tube lens. The measured lateral magnification errors for the different colors are below 0.5 pixel, which demonstrates intrinsic color registration of the WSI system. The NAT based analysis of the full-field aberration maps across the FOV shows a misalignment of the middle sensorlet with respect to the optical axis. It also provides evidence for the effect of conjugate change on the measured aberrations across the FOV. Since we used an image-based aberration measurement method, the outcome can be affected by the quality of the scanned images. The first prototype of the sensor shows significant line-to-line noise and a low dynamic range, which can contribute to the statistical and systematic

uncertainties for the aberrations and NAT coefficients. A possible next step would be to measure the sensitivity of the NAT coefficients for each full-field aberration map (astigmatism, coma) with respect to intentional misalignments (tilt or decenter of components), which then would lead to a calibration tool for the different misalignments. Such a non-invasive calibration tool can be used for testing and optimizing the alignment of WSI systems during assembly and maintenance.

We imaged H&E stained prostate tissue slides with different specimen thicknesses and staining concentrations. We found that a tissue section with 20 μm specimen thickness and prepared with a five times lower staining concentration can be imaged through-focus with reasonable axial contrast. The results for 60 μm and 100 μm specimen thicknesses prepared with a ten times lower staining concentration show substantial contribution of axial crosstalk between layers of the scanned 3D stack. The increased haziness of the images may be reduced by a further decrease of staining concentration along with novel tissue clearing techniques [55, 56] to reduce scattering. Further investigation could eventually lead to a better/different approach in the study of tissue morphology, which in essence is defined as a 3D structure. Pathologists can reap benefits of imaging deep in a thick tissue sections. This enables viewing multiple tissue layers and can possibly result in more accurate diagnosis.

The 3D-WSI scanner platform enables novel contrast modalities based on computational imaging approaches. Multispectral imaging with spectral demixing enables the disentanglement of different stains applied to the same tissue section thereby avoiding registration of multiple slides scanned sequentially with these different stains. To this end we used a PCA-based analysis to remove or highlight targeted information in the scanned images. We found that the method is highly sensitive to the stain color. The method breaks down when the spectral overlap among the stains are too high. Staining combinations that make better use of the entire color gamut, i.e. stains on top of H&E that have a significant red and/or green appearance, can improve the outcome of the multispectral analysis. This would open up the possibility to use more complicated staining protocols. A different computational imaging approach enabled by the platform is defocus-based phase-contrast imaging of thin unstained tissue slides. We retrieved the phase for unstained human cheek epithelial cells. The measured optical path length difference inside the cells between nuclei and cytoplasm is about 20 nm. Considering the approximate thickness of 1 μm for the sample results in refractive index change of about 0.02, which is relatively small. Further steps are required to fully realize this approach for our platform. These steps include measuring calibration phase samples, evaluating various phase retrieval algorithms, and scanning unstained tissue sections.

ACKNOWLEDGMENT

We would like to thank Laura Waller and Jingshan Zhao for providing us with the code of the sparse ACEKF algorithm.

REFERENCES

- [1] B. Hulsken, D. Vossen, and S. Stallinga, *High NA diffractive array illuminators and application in a multi-spot scanning microscope*, Journal of the European Optical

- Society: Rapid Publications **7**, 120261–7 (2012).
- [2] G. Zheng, R. Horstmeyer, and C. Yang, *Wide-field, high-resolution Fourier ptychographic microscopy*, *Nature Photonics* **7**, 739–745 (2013).
- [3] K. Guo, S. Dong, and G. Zheng, *Fourier ptychography for brightfield, phase, dark-field, reflective, multi-slice, and fluorescence imaging*, *IEEE J. Select. Topics Quantum Electron.* **22**, 1–12 (2015).
- [4] L. Tian, et al., *Computational illumination for high-speed in vitro Fourier ptychographic microscopy*, *Optica* **2**, 904–911 (2015).
- [5] J. Wu, et al., *Wide field-of-view microscope based on holographic focus grid illumination*, *Opt. Lett.* **35**, 2188–2190 (2010).
- [6] S. Pang, C. Han, M. Kato, P. W. Sternberg, and C. Yang, *Wide and scalable field-of-view Talbot-grid-based fluorescence microscopy*, *Opt. Lett.* **37**, 5018–5020 (2012).
- [7] F. Ghaznavi, A. Evans, A. Madabhushi, and M. Feldman, *Digital imaging in pathology: whole-slide imaging and beyond*, *Annual Review of Pathology: Mechanisms of Disease* **8**, 331–359 (2013).
- [8] J. R. Gilbertson, et al., *Primary histologic diagnosis using automated whole slide imaging: a validation study*, *BMC Clinical Pathology* **6** (2006).
- [9] M. G. Rojo, G. B. Garcia, C. P. Mateos, J. G. Garcia, and M. C. Vicente, *Critical comparison of 31 commercially available digital slide systems in pathology*, *International Journal of Surgical Pathology* **14**, 285–305 (2006).
- [10] R. Randell, R. Ruddle, and D. Treanor, *Barriers and facilitators to the introduction of digital pathology for diagnostic work*, *Studies in Health Technology and Informatics* **216**, 443–447 (2015).
- [11] L. Pantanowitz, et al., *Validating whole slide imaging for diagnostic purposes in pathology: guideline from the college of American pathologists pathology and laboratory quality center*, *Archives of Pathology and Laboratory Medicine* **137**, 1710–1722 (2013).
- [12] D. R. Snead, et al., *Validation of digital pathology imaging for primary histopathological diagnosis*, *Histopathology* (2015).
- [13] P. W. Hamilton, Y. Wang, and S. J. McCullough, *Virtual microscopy and digital pathology in training and education*, *Acta Pathologica, Microbiologica, et Immunologica Scandinavica* **120**, 305–315 (2012).
- [14] K. Foster et al., *Medical education in the digital age: Digital whole slide imaging as an e-learning tool*, *Journal of Pathology Informatics* **1**, 14 (2010).
- [15] L. Pantanowitz and A. V. Parwani, *Education*, in *Digital Pathology* (Springer, 2016).

- [16] E. A. Krupinski, A. K. Bhattacharyya, and R. S. Weinstein, *Telepathology and digital pathology research*, in *Digital Pathology* (Springer, 2016).
- [17] P. W. Hamilton, et al., *Digital pathology and image analysis in tissue biomarker research*, *Methods* **70**, 59–73 (2014).
- [18] M. C. Montalto, R. R. McKay, R. J. Filkins, et al., *Autofocus methods of whole slide imaging systems and the introduction of a second-generation independent dual sensor scanning method*, *Journal of Pathology Informatics* **2**, 44 (2011).
- [19] B. Hulsken, *Autofocus based on differential measurements*, US Patent App. 13/805,555 (2011).
- [20] M. E. Bravo-Zanoguera, C. A. Laris, L. K. Nguyen, M. Oliva, and J. H. Price, *Dynamic autofocus for continuous-scanning time-delay-and-integration image acquisition in automated microscopy*, *Journal of Biomedical Optics* **12**, 034011–034011 (2007).
- [21] R.-T. Dong, U. Rashid, and J. Zeineh, *System and method for generating digital images of a microscope slide*, US Patent App. 10/897,941 (2004).
- [22] T. C. Cornish, R. E. Swapp, and K. J. Kaplan, *Whole-slide imaging: routine pathologic diagnosis*, *Advances in Anatomic Pathology* **19**, 152–9 (2012).
- [23] N. Roberts, et al., *Toward routine use of 3D histopathology as a research tool*, *The American Journal of Pathology* **180**, 1835–1842 (2012).
- [24] E. A. El-Gabry, A. V. Parwani, and L. Pantanowitz, *Whole-slide imaging: widening the scope of cytopathology*, *Diagnostic Histopathology* **20**, 456–461 (2014).
- [25] W. E. Khalbuss, L. Pantanowitz, and A. V. Parwani, *Digital imaging in cytopathology*, *Pathology Research International* **2011** (2011).
- [26] T. Kalinski, et al., *Virtual 3D microscopy using multiplane whole slide images in diagnostic pathology*, *American Journal of Clinical Pathology* **130**, 259–264 (2008).
- [27] R. M. Levenson, *Spectral imaging and pathology: seeing more*, *Laboratory Medicine* **35**, 244–251 (2004).
- [28] R. M. Levenson, A. Fornari, and M. Loda, *Multispectral imaging and pathology: seeing and doing more*, *Expert Opinion on Medical Diagnostics* **2**, 1067–1081 (2008).
- [29] W.-L. Liu, et al., *Application of multispectral imaging in quantitative immunohistochemistry study of breast cancer: a comparative study*, *Tumor Biology* , 1–12 (2015).
- [30] K. Lee, et al., *Quantitative phase imaging techniques for the study of cell pathophysiology: from principles to applications*, *Sensors* **13**, 4170–4191 (2013).
- [31] G. Popescu, *Quantitative phase imaging of cells and tissues* (McGraw Hill Professional, 2011).

- [32] S. Sridharan, V. Macias, K. Tangella, A. Kajdacsy-Balla, and G. Popescu, *Prediction of prostate cancer recurrence using quantitative phase imaging*, Scientific Reports **5** (2015).
- [33] C. J. Sheppard, S. S. Kou, and S. Mehta, *Quantitative phase imaging in microscopy*, in *Fringe 2009* (Springer, 2009).
- [34] Z. Jingshan, J. Dauwels, M. A. Vazquez, and L. Waller, *Sparse ACEKF for phase reconstruction*, Opt. Express **21**, 18125–37 (2013).
- [35] L. Waller, *Phase imaging with partially coherent light*, SPIE BiOS , 85890K–6 (2015).
- [36] L. Waller, L. Tian, and G. Barbastathis, *Transport of intensity phase-amplitude imaging with higher order intensity derivatives*, Opt. Express **18**, 12552–61 (2010).
- [37] L. Waller, M. Tsang, S. Ponda, S. Y. Yang, and G. Barbastathis, *Phase and amplitude imaging from noisy images by Kalman filtering*, Opt. Express **19**, 2805–14 (2011).
- [38] B. Hulsken, *Method for simultaneous capture of image data at multiple depths of a sample*, Patent WO2016102200A1 (2016).
- [39] B. Hulsken, *Scanning imaging system with a novel imaging sensor with gaps for electronic circuitry*, Patent WO2015091300A1 (2015).
- [40] B. Hulsken and S. Stallinga, *Sensor for microscopy*, US Patent App. 13/519,360 (2010).
- [41] H. Netten, L. J. Van Vliet, F. R. Boddeke, P. De Jong, and I. T. Young, *A fast scanner for fluorescence microscopy using a 2D CCD and time delayed integration*, BioImaging **2** (1994).
- [42] S. Stallinga, *Finite conjugate spherical aberration compensation in high numerical-aperture optical disc read-out*, Appl. Opt. **44**, 7307–7312 (2005).
- [43] S. M. Shakeri, B. Hulsken, L. J. van Vliet, and S. Stallinga, *Optical quality assessment of whole slide imaging systems for digital pathology*, Opt. Express **23**, 1319–1336 (2015).
- [44] S. M. Shakeri, B. Hulsken, L. J. van Vliet, and S. Stallinga, *Shack-Hartmann sensor based optical quality testing of whole slide imaging systems for digital pathology*, Proc. SPIE 9315, Design and Quality for Biomedical Technologies VIII , 931504 (2015).
- [45] L. J. Van Vliet, F. R. Boddeke, D. Sudar, and I. T. Young, *Image detectors for digital image microscopy*, Digital Image Analysis of Microbes: Imaging, Morphometry, Fluorometry, and Motility Techniques and Applications , 37–63 (1998).
- [46] J. C. Mullikin, et al., *Methods for CCD camera characterization*, Proc. SPIE **2173**, 73–84 (1994).

- [47] K. Thompson, *Description of the third-order optical aberrations of near-circular pupil optical systems without symmetry*, J. Opt. Soc. Am. A **22**, 1389–1401 (2005).
- [48] K. P. Thompson, T. Schmid, O. Cakmakci, and J. P. Rolland, *Real-ray-based method for locating individual surface aberration field centers in imaging optical systems without rotational symmetry*, J. Opt. Soc. Am. A **26**, 1503–1517 (2009).
- [49] K. P. Thompson, T. Schmid, and J. P. Rolland, *Recent discoveries from nodal aberration theory*, International Optical Design Conference **7652**, 76522Q (2010).
- [50] I. Jolliffe, *Principal component analysis* (Wiley Online Library, 2002).
- [51] E. Barone-Nugent, A. Barty, and K. Nugent, *Quantitative phase-amplitude microscopy I: optical microscopy*, Journal of Microscopy **206**, 194–203 (2002).
- [52] M. R. Teague, *Deterministic phase retrieval: a Green's function solution*, J. Opt. Soc. Am. **73**, 1434–1441 (1983).
- [53] M. Soto and E. Acosta, *Improved phase imaging from intensity measurements in multiple planes*, Appl. Opt. **46**, 7978–7981 (2007).
- [54] Z. Jingshan, R. A. Claus, J. Dauwels, L. Tian, and L. Waller, *Transport of intensity phase imaging by intensity spectrum fitting of exponentially spaced defocus planes*, Opt. Express **22**, 10661–74 (2014).
- [55] E. A. Genina, A. N. Bashkatov, and V. V. Tuchin, *Tissue optical immersion clearing*, Expert Review of Medical Devices **7**, 825–842 (2010).
- [56] D. S. Richardson and J. W. Lichtman, *Clarifying tissue clearing*, Cell **162**, 246–257 (2015).

6

CONCLUSIONS & RECOMMENDATIONS

6.1. CONCLUSIONS

In the course of this thesis we have built and characterized a modular Whole Slide Imaging (WSI) platform for application in the emerging field of digital pathology. This platform enables good quality brightfield microscopy and provides 2D as well as 3D images of tissue slides. The following is the summary of our achievements:

1) A systematic method for testing and monitoring the optical quality of WSI systems has been developed and validated. This non-invasive tool assesses the overall image quality of the entire system based on analysis of the through-focus Optical Transfer Function (OTF) obtained from the edge response of a custom-made resolution target. This assessment enables the measurement of a number of primary aberrations such as spherical aberration, coma, astigmatism, and field curvature. The statistical error in the determined aberrations is typically below $20\ m\lambda$. The method was used to compare different tube lens designs and to study the effect of objective lens aging. The results were in good agreement with direct measurement of aberrations based on Shack-Hartmann wavefront sensing with a typical error ranging from $10\ m\lambda$ to $40\ m\lambda$.

2) A technique to measure the full-field optical aberrations of WSI systems using a Shack-Hartmann wavefront sensor is presented and tested. We used Nodal Aberration Theory (NAT) to analyze the resulting full-field aberration maps for primary astigmatism and coma in terms of a limited set of coefficients. This theory appeared to fit well to the experimental data. We have measured and analyzed the full-field aberration maps for two different objective lens-tube lens assemblies and found that only the astigmatism coefficient related to optical design differed substantially between the two cases, in agreement with expectations. We have also studied full-field aberration maps for intentional decenter and tilt and found that these affect the misalignment NAT coefficient for constant coma (decenter) and the misalignment NAT coefficient for linear astigmatism (tilt), while keeping all other NAT coefficients constant. The non-invasive through-focus

OTF-based test in combination with NAT coefficients can be used for checking and improving the alignment of the WSI system.

3) The effect of partial coherence on the WSI system was investigated. Firstly, in order to find the optimal value of the partial coherence factor σ for WSI systems, and secondly in order to examine how our OTF-based optical quality test, developed under the assumption of having an incoherent optical imaging system, is affected by partially coherent illumination. The investigation is based on the analysis of the edge response of an optical system. We specifically focused on two practical aspects: edge ringing and Depth of Focus (DOF). Simulations showed that the practical tolerance limit for σ to avoid edge ringing is about 0.75, which kept the edge overshoot below 2.9%. For quantifying the DOF we used the FWHM of the through-focus MTF at the middle range of spatial frequencies, $[0.1 - 1] \times 2NA/\lambda$. We proposed a semi-quantitative scaling of DOF with the partial coherence factor, which agreed reasonably well with numerical simulations. This scaling law could possibly be used to find the value of the partial coherence factor σ such that the system achieves a desired DOF for the spatial frequency content of a targeted feature. To experimentally evaluate these analyses, we designed, built and implemented a compact Köhler illumination unit with variable Numerical Aperture (NA). We showed that the optimum σ value is highly dependent on the required specifications for lateral resolution, DOF, and edge ringing. The best σ value in practice can be found by knowing the smallest feature of interest and the overshoot tolerance limit. Regarding the evaluation of our optical quality test, we found that approaching the coherent limit results in a lower accuracy of estimating coma. This can also have impact on the alignment check of an optical system by analyzing Phase Transfer Function (PTF) curves across the Field Of View (FOV) (see chapter 3).

4) A novel 3D multispectral WSI platform is demonstrated for application in digital pathology based on a new custom designed image sensor containing 128 sensorlets building upon previous efforts at Philips. Each sensorlet acts as an individual line scan camera. This sensor enables simultaneous scanning of multiple focus levels when the sensor is placed tilted in the light path. We have built an experimental setup to demonstrate this concept of 3D imaging with a single scan. We achieved simultaneous scanning of 10 different focus levels, which can be chosen arbitrarily in the range of thicknesses of up to around $20\mu m$ (using a $20\times/NA0.75$ objective lens) and up to around $80\mu m$ (using a $10\times/NA0.45$ objective lens). The lower NA of the 10x objective was required in order to reduce the spherical aberration sensitivity for the thicker tissue slices. Additionally, we designed and built a 5-color LED-based sequential illumination unit to perform multispectral imaging. We have achieved a scanning speed of 5 k lines/sec per color scanning with the first prototype of the sensor. The goal is to reach a maximum 200 k lines/sec for a single sensorlet in a next version of the sensor. We characterized the WSI platform, evaluated its performance by imaging prostate tissue slides, and eventually experimented with two computational imaging approaches, namely multispectral imaging and defocus-based quantitative phase imaging. The Analog to Digital Converter (ADC) of the prototype sensor had to be operated at high gain and offset, preventing a realistic determination of these numbers with a standard mean intensity vs. variance of the intensity measurement. We also measured the primary aberrations for a single sensorlet, which showed overall a diffraction-limited performance with two exceptions:

astigmatism close to the edge of the FOV and coma for the blue color channel, which reached levels close to $80 \text{ m}\lambda$. The lateral color error was measured to be below 0.5 pixel across the entire field of view for all sensorlets, thus providing intrinsic color registration of all the color channels. By imaging Haematoxylin and Eosin (H&E) stained prostate tissue slides with different thicknesses and staining concentrations, we found that tissue sections up to $20 \mu\text{m}$ thickness and with relatively low staining concentration can be imaged through focus with reasonable axial contrast. The results for $60 \mu\text{m}$ and $100 \mu\text{m}$ thick tissue slides with further diluted staining concentration show substantial axial crosstalk between layers of the scanned 3D stack. We employed our 5-color illumination unit to perform multispectral imaging. We used a PCA-based analysis technique to selectively emphasize or remove individual stains in the scanned images. The results were promising for the case in which the spectral overlap between the stains is low. Since the new platform scanned multiple focus level simultaneously, we also touched upon the topic of defocus-based phase contrast imaging of thin unstained tissues with a proof-of-principle scan of unstained human cheek epithelial cells.

6.2. RECOMMENDATIONS

Here I present a list of recommendations could possibly be used to improve and extend our achievements in this thesis.

6.2.1. OPTICAL QUALITY TEST

The first aspect that could improve our optical quality test is a redesign of the custom resolution target. Currently we measured aberrations by analyzing the through-focus OTF derived from vertical and horizontal edges which only provided information about zero degree astigmatism. By incorporating 45 degree edges it will be possible to also measure diagonal astigmatism, which provides more complete information on the low order astigmatism in the system. A possible way is to use a checkerboard pattern instead of vertical and horizontal bars. This pattern can contain both up-right and 45 degrees rotated checkerboard areas over the field of view.

A second aspect open for improvement derives from the observation that there was mild aliasing in the currently realized WSI setup. The slanted edge technique can be used to reduce the impact of aliasing on our optical quality test measurement.

The last aspect concerns the partial coherence effect. In chapter 4, we showed that approaching the coherent limit can reduce the accuracy of our proposed optical quality test particularly concerning coma, for which the OTF-based measurement is most sensitive to partial coherence effects. This effect should be taken into account in follow up versions of the optical quality testing tool, especially if the tool is used for the alignment of the system.

6.2.2. NAT AND DISTORTION

We have shown in this thesis that Nodal Aberration Theory (NAT) can be efficient in aligning digital microscope as it was for big astronomical telescopes since both have small field angles. NAT has the potential to be used as a non-invasive alignment tool in digital microscopes. The information that we acquired about lower-order astigmatism,

coma, and distortion can be employed to pinpoint specific misalignments in the optical system. An analysis of distortion with NAT has not been tried so far, but could potentially provide more accurate information regarding misalignment. A key advantage would be that an analysis and interpretation of the through-focus OTF would not be necessary. A follow up investigation on NAT and distortion is therefore recommended.

We also propose to set up a dedicated calibration procedure to determine the sensitivity of the NAT coefficients for each full-field aberration map (astigmatism and coma) with respect to various intentional misalignments (tilt and decenter of components) in the optical system. This approach can be used effectively in the 3D WSI platform since it has sensorlets at different positions in the FOV and therefore can provide aberration information across the entire FOV.

6.2.3. 3D WSI PLATFORM

WSI systems put digital pathology in a path to eventually supplant conventional diagnosis with analog microscopes. It aims to deliver a platform packed with various hardware and software features in order to provide a pathologist with relevant information for improving diagnosis. Most of the current WSI systems scan 2D images of tissue slides. This deprives pathologist of having a through-focus view of a thin tissue slice under inspection. The modular WSI platform described in this thesis can perform 2D/3D imaging in a single scan and has the potential to accommodate other microscopy modalities along with brightfield microscopy. In addition it can open up attractive novel applications for digital pathology such as:

3D content: The scope of 3D imaging can be broadened from viewing thin tissue slices through-focus to a comprehensive study of 3D tumor morphology. For example, real 3D structures of healthy and malignant tissues can be investigated in order to pinpoint the differences from a view based on a limited set of 2D cross-sections. This can possibly even be tried in clinical studies of tumor progression and the effect of drugs on tumor morphology. Important technical developments in this respect are tissue clearing technology (for minimizing scattering in thick tissue slices) and adaptive optics (for controlling spherical aberration inherent to focusing through relatively thick layers of a specimen).

Molecular imaging: Specific stains are available to target specific proteins (immunostaining methods) or genes/DNA (via the family of In-Situ Hybridization (ISH) techniques). Using these stains and digitizing the imaging process make it possible to correlate the proteomic and/or genetic information to the tissue morphology on the ~1 mm scale of the scanned tissue sections. For example, scanning one section with Hematoxylin and Eosin (H&E) staining and the adjacent one with ISH would make it possible to overlay the genetic information retrieved from the ISH slide onto the digitized H&E slide. The multi-spectral approach has the potential to have a number of such information-rich stains in a single section.

Large scale Fluorescence In Situ Hybridization (FISH): In this thesis, we have restricted the analysis to brightfield microscopy as that is the default method in pathology for examination of tissue sections. Fluorescence microscopy, however, provides more quantifiable information and becomes the method of choice when the required sensitivity cannot be met using absorption stains. Techniques such as FISH use fluorescent

probes to label specific genes in order to find the gene copy number within the cells of the tissue. It is currently used in breast cancer diagnosis for testing for so-called HER2-positive cases, as these patients receive a drug that specifically targets HER2-positive tumor cells. Being able to perform fluorescence microscopy, in particular FISH, and bright-field microscopy both in one platform can substantially facilitate the digital pathology work flow. It is, however, challenging to achieve a high throughput on par with bright-field microscopy because the fluorescence signal levels are typically much weaker than brightfield signal levels. In the current hardware, the implementation can be realized by adding a LED-based epi-illumination branch similar to the already realized color-sequential illumination unit described in this thesis. In addition it is necessary to develop a fast and tunable optical filter or a multi pass-band dichroic mirror for coupling the LED emission into the light path.

Microscopy on unstained tissues and cells: In some cases cell and tissue preparation and the staining process may change the morphology of the sample. Techniques such as phase-contrast imaging can be used to look at a specimen in its native unstained state. This may in particular be considered for cytology applications where the sample is typically sparse. Defocus-based phase-contrast is anticipated to work best on sparse samples. We showed a proof-of-principle scan for defocus-based phase-contrast imaging with the 3D WSI platform. This particular technique can be adopted readily since multiple layers in one scan are imaged. Further steps are suggested to fully realize this approach, such as measuring calibration phase samples, evaluating various phase retrieval algorithms, and benchmarking unstained tissue scans with a corresponding reference H&E scan.

Automated image analysis: The resulting large image data files generated by the platform can be a valuable source of extra/new information for pathologists. Relevant information on biomarkers can potentially be extracted from these datasets by machine learning algorithms, in particular novel so-called deep learning approaches. Deep learning algorithms have recently found applications in fields such as computer vision and automatic speech recognition, and may also fit well with analysis of tissue morphology. In particular one can envision new ways of locally correlating the parameters found with image analysis to the tissue structure (e.g. make an overlay or heat map). This could for example result in a new method for studying the heterogeneity of tumors.

SUMMARY

Digital pathology is based on the use of digital images of tissues for diagnosis of diseases. In the emerging clinical practice of digital pathology, images of tissue slides are acquired with a high-resolution and high-throughput automated microscope, a so called Whole Slide Imaging (WSI) system. We designed, built and characterized a modular WSI platform for conducting two- and three-dimensional brightfield microscopy, the most common modality in this field.

We developed a non-invasive systematic approach to test and quantify the optical quality without the need for an external aberration measurement instrument. This is an important feature since the optical quality of WSI systems needs to be self-monitored continuously for assuring that the pathologist is offered the best possible digital image quality. Our proposed method uses a measurement of the through-focus Optical Transfer Function (OTF) obtained from the edge response of a custom-made resolution target. This enabled quantitative analysis of a number of primary aberrations such as spherical aberration, coma, astigmatism and field curvature. The statistical error in the determined aberrations is typically below $20\ m\lambda$. To verify this approach we used a Shack-Hartmann wavefront sensor, a well-established aberration sensor, as benchmark. The comparison resulted in a typical error ranging from $10\ m\lambda$ to $40\ m\lambda$. We also showed that full-field aberration maps can be used to find the root cause of the aberrations in WSI systems, e.g. tilt or decenter of the optical components. Our approach was inspired by Nodal Aberration Theory (NAT), which is developed for analyzing and quantifying misalignment in optical telescopes. NAT has a great potential to be an alignment tool in the manufacturing process of microscopy tools such as WSI systems.

We subsequently focused on investigating the effect of the partial coherence factor σ on the optical imaging system. This was motivated by two reasons: 1) Determining the practical optimum value for σ in the trade-off involving lateral resolution, edge contrast, edge ringing, and Depth of Focus (DOF). Simulations showed that the practical tolerance limit for σ to avoid edge ringing is about 0.75, which kept the edge overshoot below 2.9%. Then, a compact Köhler illumination unit with variable Numerical Aperture (NA) was designed and used to evaluate the analysis experimentally. It is shown that the optimum σ value is highly dependent on the required specifications for lateral resolution, DOF, and edge ringing. 2) Studying the impact on our OTF-based optical quality test, which was based on the assumption of an incoherent optical imaging system. We found that approaching the coherent limit results in a lower accuracy of estimating coma, which was based on the assumption of a third-order polynomial shape for the Phase Transfer Function (PTF) curve. To experimentally evaluate all these analyses we designed, built and used a compact Köhler illumination unit with adjustable σ .

Finally we realized an experimental WSI platform for studying 2D and 3D multi-color brightfield microscopy of tissues slides with different stains and thickness, building upon previous efforts at Philips on 3D multispectral scanning with a new custom-

designed image sensor placed tilted in the scan direction at the image plane. This new sensor consists of 128 imaging sensorlets that can be independently read and configured. This configuration enables simultaneous scanning of different focus levels. We performed a thorough sensor and optical characterization on this platform. With the first prototype of the sensor, we achieved a simultaneous scan of 10 different focus levels using 10 sensorlets with a speed of 5 k lines/s per color. We also showed the ability of this WSI platform to perform other microscopy modalities based on computational imaging such as: multispectral imaging and defocus-based quantitative phase imaging. Regarding the application in digital pathology, we imaged H&E stained prostate tissue slides with different specimen thicknesses and staining concentrations using two different objective lens-tube lens assemblies. A tissue section with 20 μm specimen thickness and prepared with staining concentration five times lower than a standard protocol for 4 μm thick slices can be imaged through-focus with reasonable axial contrast. The results for 60 μm and 100 μm specimen thicknesses prepared with a twofold further diluted staining concentration show substantial contribution of axial crosstalk between layers of the scanned 3D stack.

An experimental WSI platform is now available to study 2D and 3D brightfield imaging for different applications in digital pathology. It has the potential to be used in comprehensive studies of 3D tumor morphology, in molecular imaging of thick tissues by using specific stains to target specific proteins or genes. The resulting 3D-stack of images can be used by machine learning algorithms such as deep learning to provide automated analyses of heterogeneous tissue structures that may lead to useful information in e.g. tumor grading. It can also be extended further to perform large scale fluorescence scanning by adding an epi-illumination branch to the WSI platform.

SAMENVATTING

Digitale pathologie is gebaseerd op het gebruik van digitale beelden van weefsel voor de diagnose van ziekten. In deze in de klinische praktijk opkomende techniek, worden afbeeldingen van weefselcoupes op objectglasjes verkregen met een hoge resolutie en zeer snelle geautomatiseerde microscoop, een zogenaamd "Whole Slide Imaging" (WSI) systeem. We hebben een modulair WSI-platform gebouwd en gekarakteriseerd voor het uitvoeren van twee- en driedimensionale witlicht microscopie, de meest voorkomende modaliteit op dit gebied.

We hebben een niet-invasieve systematische methode ontwikkeld om de optische kwaliteit te testen en kwantificeren zonder de noodzaak van een extra meetinstrument voor aberraties. Dit is een belangrijk kenmerk, omdat de optische kwaliteit van WSI systemen continu en automatisch moet worden gevolgd om te verzekeren dat de patholoog wordt voorzien van digitale beelden van optimale kwaliteit. De door ons ontwikkelde methode maakt gebruik van een meting van de door-focus Optische Overdrachtsfunctie verkregen uit de stapresponsfunctie gemeten aan een speciaal gemaakt resolutie-testobject. Dit maakt een kwantitatieve analyse mogelijk van een aantal primaire aberraties, zoals sferische aberratie, coma, astigmatisme en veldkromming. De statistische fout in de bepaalde afwijkingen is meestal lager dan $20 \text{ m}\lambda$. Om deze aanpak te verifiëren hebben we gebruik gemaakt van een Shack-Hartmann sensor, een veel gebruikte aberratiesensor. De vergelijking resulteerde in een typische fout variërend van $10 \text{ m}\lambda$ tot $40 \text{ m}\lambda$. We toonden ook aan dat dat aberratiekaarten van het volledige afgebeelde optische veld kunnen worden gebruikt om de oorzaak van afwijkingen in WSI systemen te vinden, bijvoorbeeld een kanteling of verschuiving van de optische componenten. Onze aanpak is geïnspireerd door de Nodale Aberratie Theorie (NAT), die oorspronkelijk is ontwikkeld voor het analyseren en kwantificeren van de uitlijning van optische telescopen. NAT kan in potentie een hulpmiddel te zijn bij de uitlijning tijdens het productieproces van microscopie-systemen zoals WSI systemen.

Vervolgens hebben we ons gericht op het onderzoeken van het effect van de partiële coherentie factor σ op het optisch afbeeldingssysteem. Dit werd ingegeven door twee redenen: 1) Het bepalen van de optimale waarde voor σ in de praktijk waarbij een compromis gesloten moet worden met betrekking tot laterale resolutie, contrast van randen, rand-oscillaties, en scherptediepte (DOF). Uit simulaties bleek dat de praktische tolerantiegrens voor σ om rand-oscillaties te voorkomen ongeveer 0,75 is, waarbij de rand minder dan 2,9 % wordt overschoten. 2) het bestuderen van de impact op onze optische overdrachtsfunctie gebaseerde optische kwaliteitstest, die gebaseerd is op de aanname van een incoherent optische beeldvormend systeem. We vonden dat het naderen van de coherente limiet resulteert in een lagere nauwkeurigheid van de schatting van coma, welke gebaseerd was op de aanname dat de Fase Overdrachtsfunctie de vorm van een derde orde polynoom had. Om al deze analyses experimenteel te evalueren hebben we een compacte Köhler belichtingseenheid ontworpen, gebouwd en gebruikt met va-

riabele numerieke apertuur (NA). Daarmee hebben we aangetoond dat de optimale σ waarde sterk afhankelijk is van de vereiste specificaties voor laterale resolutie, DOF, en de rand-oscillaties.

Tot slot hebben we een experimenteel WSI platform gerealiseerd voor het bestuderen van 2D- en 3D-meerkleuren microscopie van weefselscoupes met verschillende kleuringen en diktes, voortbouwend op eerdere inspanningen van Philips op 3D-scannen met een nieuwe beeldsensor die gekanteld in de scanrichting in het beeldvlak wordt geplaatst. Deze nieuwe sensor bestaat uit 128 lijnsensoreenheden die onafhankelijk kunnen worden gelezen en ingesteld. Deze configuratie maakt het gelijktijdig scannen van verschillende focusniveaus mogelijk. We voerden een grondige karakterisatie uit van de sensor en de optica van dit nieuwe platform. Met het eerste prototype van de sensor behaalden we een gelijktijdige scan van 10 verschillende focusniveaus met behulp van 10 sensoreenheden met een snelheid van 5 k lijnen/s per kleur. We toonden ook de mogelijkheden van dit WSI-platform om andere microscopiemodaliteiten gebaseerd op de techniek van “computational imaging” uit te voeren, zoals: multispectrale en defocus gebaseerde kwantitatieve fase-beeldvorming. Met betrekking tot de toepassing in de digitale pathologie hebben we standaard aangekleurde prostaatweefselcoupes afgebeeld met verschillende diktes van de coupe, verschillende kleuring-concentraties, en gemeten met twee verschillende objectief en tubus-lens combinaties. Een weefselcoupe met 20 μm dikte, en geprepareerd met een kleuring-concentratie vijf keer lager dan een standaard protocol voor 4 μm dikke coupes, kan door-focus worden afgebeeld met een redelijk axiaal contrast. De resultaten voor 60 μm en 100 μm diktes, bereid met een twee keer verder verdunde kleuring concentratie tonen een substantiële axiale overspraak tussen de lagen van de gescande 3D-set aan.

Het experimentele WSI-platform is nu beschikbaar voor 2D- en 3D-witlicht microscopie studies voor verschillende toepassingen in de digitale pathologie. Het heeft de potentie om gebruikt te worden in uitgebreide studies van 3D tumor-morfologie en in moleculaire beeldvorming van dikke weefselcoupes door gebruik te maken van labels om specifieke eiwitten of genen in beeld te brengen. De resulterende 3D afbeeldingen kunnen door zogenaamde “machine learning” algoritmen zoals “deep learning” worden gebruikt voor geautomatiseerde analyse van heterogene weefselstructuren, wat kan leiden tot nuttige informatie ten behoeve van tumordiagnostiek. Het kan ook verder worden uitgebreid om grootschalige fluorescentie afbeeldingen op te nemen door toevoeging van een epi-belichtingstak aan het WSI-platform.

CURRICULUM VITÆ

Mojtaba Shakeri was born in Mashhad, Iran on 18 September 1982. He obtained his B.Sc. degree in Electrical Engineering (Control) from Iran University of Science and Technology in 2005. Afterwards, he worked as a technical engineer at Middle East Petro Gas Engineering Co. for one year to design and construct a data acquisition and recording system for pipeline inspection tools. Then he continued his study in Electrical Engineering (Control) and obtained his M.Sc. from Iran University of Science and Technology with distinction in 2009. He designed and implemented a magnetic attitude control system for a spinning satellite. During his M.Sc. education, he was a member of the student satellite research center. He designed and built magnetic actuators, a 3-axis magnetometer and programmed a software tool for designing spinning satellites at the system level.

From January 2012, he started his PhD in the Department of Imaging Physics at Delft University of Technology. His project was on automated slide scanning for digital pathology. He collaborated closely with Philips digital pathology within the framework of the Cyttron II consortium on bioimaging technologies.

Since March 2016, he has been working as a design engineer at ASML, a company which provides lithography systems for the semiconductor industry.

LIST OF PUBLICATIONS

4. S.M. Shakeri, L. van der Graaf, G.J.L.H. van Leenders, L.J. van Vliet, B. Hulsken, and S. Stallinga, *Novel 3D multispectral WSI platform for digital pathology*, manuscript in preparation.
3. S.M. Shakeri, L.J. van Vliet, and S. Stallinga, *The impact of partial coherence on the apparent optical transfer function derived from the response to amplitude edge*, submitted to Applied Optics.
2. S.M. Shakeri, B. Hulsken, L.J. van Vliet, and S. Stallinga, *Shack-hartmann sensor based optical quality testing of whole slide imaging systems for digital pathology*, in Proc. SPIE 9315, Design and Quality for Biomedical Technologies VIII (2015).
1. S.M. Shakeri, B. Hulsken, L.J. van Vliet, and S. Stallinga, *Optical quality assessment of whole slide imaging systems for digital pathology*, Optics Express, Optics Express 23, 1319 (2015).

ACKNOWLEDGEMENTS

This thesis is an outcome of my enjoyable and unforgettable experience at Delft University of Technology. Surely, this would have not been possible without the help and support of many people. I would like to gratefully thank them.

Sjoerd, thank you for giving me the freedom to explore my way, for continuously helping me, for reviewing and editing in short notice, and for checking on me in the lab when I was busy with constructing the setup.

Lucas, thank you for all the practical and constructive advice and suggestions in the progress meetings, and for making "dagjes uit" even more fun.

Bas, Jeroen, Prarthana, and Rik at Philips Digital Pathology, thank you for your valuable support and fruitful collaboration.

Wim and Ron, thank you for helping me with the building of the setup and for showing me the right way to build things.

Nitish, Luca, and Tim, thank you for providing me with some optical components and the Shack-Hartmann sensor.

Ronald, thank you for your help in IT related issues and for understanding my Apple addiction.

My officemates Robert, Nadya, Tom, and Richard, thank you for your support, help and fruitful discussions, and also for understanding the importance of playing darts after lunch.

Zhang, thank you for all the fun we have had together, for teaching me how to play badminton professionally, and how to beat a Chinese ping-pong player.

Robiel, thank you for your great speech in our sport day victory.

Kedir, thank you for the endless fun discussion on what is less useless: android or iOS.

Jelle, thank you for being an amazing lab buddy, for adding a tinge of extra fun to every working day. I believe you still need one more year of foosball practice.

Leon, thank you for all of your remote helps when I started my new job. Thanks for being so kind to log off the lab PC, every afternoon for a while.

My colleagues at QI group, thank you all for creating the great working environment that allowed me to finish this thesis with fun and good memories.

Finally I would like to express my gratitude to my family and friends for their continuous support, especially Maryam who stood by me with unwavering encouragement all the way.

